CO outflows from young stars in Cygnus-X: Exploring the connection of protostellar and extragalactic outflows

MASTER's THESIS

Iason - Michail Skretas

Supervisor: Lars E. Kristensen

Niels Bohr Institute
University of Copenhagen
Denmark
20/05/2021

Abstract

Molecular outflows are commonly detected originating from both protostellar and extragalactic sources. Separate studies of low-mass, high-mass and extragalactic sources have revealed similar scaling relations connecting the force carried by an outflow and the properties of the source that drives it.

The aim of this work is twofold, initially, to examine the effects of clustered star formation on the protostellar outflows and their scaling relations, and secondly, to explore the possibility that outflows varying in scale and energetics by many orders of magnitude are consistent with being launched by the same physical processes.

To that end, using high-angular resolution CO [$J = 3\text{-}2$] observations of 10 high-mass protostars in the Cygnus-X molecular cloud, obtained at the SubMilliMeter Array as part of the PILS Cygnus survey, the outflow force, i.e., the momentum ejection rate, is measured. In addition, an extended sample of protostellar and extragalactic outflow force measurements is assembled from existing literature, to allow for a direct comparison of their scaling relations.

A close agreement was found between the Cygnus-X sources and sources from the literature, strongly suggesting that, clustered star formation does not have a significant impact on the outflow energetics of protostars. In addition, the comparison of the protostellar and extragalactic sources revealed, with 95% confidence, that Class 0 protostars and extragalactic sources follow the same outflow force - bolometric luminosity correlation, thus offering strong indication that protostellar and extragalactic outflows have the same launch mechanism. The existence of such a mechanism would enable the development of a single universal outflow launch model, more observations are though required in order to verify this connection.

Contents

1   Introduction

The process of forming stars takes place deep inside molecular clouds (MCs), the coldest and densest areas of the interstellar medium (ISM). Star formation is a complex process, whose details are still being extensively studied, but, one of the commonly agreed upon elements of star formation is that it gives rise to strong bipolar outflows and jets. These outflows often extend far into the surrounding ISM sweeping up gas from the surrounding envelope and carving out large cavities in the parent MCs. As the surrounding gas is swept up and accelerated by the outflow, the radiation it emits gets Doppler shifted enabling the observation of the outflows through CO emission lines. Such observations open the path to the measurement of various parameters describing the outflows, like their size, velocities and force, important in furthering our understanding of the outflows and their impact on the surrounding space. Among these parameters, we focus on the outflow force, which has been found to have an strong correlation with the mass of the envelope in which the proto-star, driving the outflow, is located, as well as, with the total bolometric luminosity of the proto-star. The existence of such uniform relations points towards a, long suspected, strong connection between the collapse of clouds and the ejection of material in the form of bipolar outflows. In addition, similar relations have been observed for extragalactic outflows. The question that naturally arises is are the physical mechanisms behind these two outflow types the same? Can outflows that vary in scale and energetics by many orders of magnitude be launched by the same physical processes? And how can we use statistical methods to compare and thereby infer similarities and differences between these types of outflows?

1.1   Molecular clouds

As the scene where the action takes place, molecular clouds have significant part to play in star formation. In brief, MCs constitute the coldest and densest areas of the ISM and according to their size, density and temperature, are split into separate categories. These are:

- The diffuse molecular clouds, which have the lowest optical extinction (lowest density) among all molecular clouds.

- The giant molecular clouds (GMCs), which are the next type of MC, in order of increasing density, but are also the largest in size.

- The dark clouds, which are in general denser, colder and significantly smaller than the GMCs.

- The dense cores/Bok globules, which are the densest, coldest and smallest of all MCs.

Overall, molecular clouds have densities ranging from 100 to 10^4 cm^{-3}, temperatures between 10 and 15 K and sizes from 0.1 pc, for dense cores, all the way up to 50 pc in the case of GMCs. The low temperatures and high densities that we encounter at the MCs create and environment that allows the existence of molecules, hence earning their name.

One of the most interesting properties of molecular clouds is that, with the exception of diffuse MCs, they are bound by their own gravitational force. This means that MCs exist in a precarious equilibrium between their own gravitational pull, dragging material towards their center, and a combination of bulk motions, thermal pressure and magnetic forces trying to disperse them. This equilibrium is best described by the Virial theorem:

$$\frac{1}{2}\frac{\partial^2 I}{\partial t^2} = 2T + 2U + W + M \tag{1}$$

In this equation, I is the generalised moment of inertia, depending on the cloud radius, T is the kinetic energy due to bulk motions of the gas, U is the energy of thermal motions, W is the gravitational energy of the clouds own self-gravity and B is the energy of the magnetic field. If, for any reason, this equilibrium is disturbed (e.g. internal turbulence, external radiation or ram pressure), it can lead to either the dispersion of the cloud, if the gravitational term becomes smaller than the rest, or, more interestingly, to collapse if the gravitational term becomes dominant.

1.2 Protostars

1.2.1 Formation process

When a molecular cloud becomes unstable and begins to collapse, it initially forms a small "lump" of material at its center. This over-dense object then attracts progressively more and more material from the surrounding cloud, until eventually it becomes opaque to its own infrared cooling radiation. This means that the central "lump" can no longer cool down effectively by radiating away the excess energy generated through the gravitational collapse, and, as it keeps accreting mass, its temperature begins to rise. The increase in temperature leads to an increase of internal pressure and thus the central object reaches hydrostatic equilibrium. The now stable object is called the first hydrostatic core and has a typical size of 5 AU (Astronomical Units), a typical mass of 0.05 M⊙ and a typical temperature of 850 K. The first hydrostatic core may be stable but it is not yet considered a protostar. As the first hydrostatic core continues to accrete material, its temperature continues to rise in order to maintain the hydrostatic equilibrium. This continues until the temperature reaches 2000 K at which point the collisional dissociation of H_2 takes place, absorbing the released gravitational energy and stopping the temperature increase, thus ending the hydrostatic equilibrium and the core starts collapsing again.

This second phase of the collapse ends when the core reaches approximately the size of the Sun, with a mass of ≈ 0.1 M⊙ and a temperature of 10^5 K. At this temperature the H gas is completely ionized, therefore all released gravitational energy is once more available to heat the core material and re-instate hydrostatic equilibrium. This new stable object is called the second hydrostatic core, and is in all regards what we refer to as a protostar.

1.2.2 Protostellar structure

The most promising scenario describing the collapse of a dense core into a protostar is probably that of the rotating collapsing core (Terebey et al. 1984). In this scenario, the inward motion of infalling material perpendicular to the cores rotation axis, is inhibited due to conservation of angular momentum. As a result, infalling material settles on the mid-plane forming a disk surrounding the central protostar. This formation scenario is strongly supported by multiple observations of such disks around protostars (Strom et al. 1989).

In this scenario, the evolving protostar accretes matter through the surrounding disk, which is, precisely for that reason, called an accretion disk. Although the exact mechanism remains uncertain, accretion through a disk is believed to give rise to strong bipolar winds and jets, which in turn entrain the surrounding envelope material forming extended outflows. For a full review of protostellar outflows, and their launching mechanisms see Bally (2016) (and references therein), but in brief, the currently prominent types of models, describing the launching of protostellar outflows, are the magnetohydrodynamic (MHD) disk winds model, the stellar wind models and the X-winds models. All three different types of models are based on the same assumptions, that the outflows are powered from the rotational energy of the protostar - circumstellar disk system and that this energy is transferred to the outflow through a magnetic field. For the MHD disk winds, the magnetic field responsible for powering the outflow is this of the disk. Assuming an initial magnetic field with lines perpendicular to the disk, the inward motion of the gas would drag them along, creating an angle between the disk and the magnetic field. At the same time, the rotation of the disk would wind up the magnetic field, leading to an hourglass-like stricture with the magnetic lines bending away from the protostar (see Fig. 1). Charged particles from the disk are then accelerated along these open magnetic lines by centripetal forces, forming the outflow. This mechanism describes well the broad outflow component as well as the varying velocities observed in protostellar outflows but fails to do so for the highly collimated jets that are also observed.

In the stellar wind type models, the magnetic field of the protostar is responsible for the outflow. More precisely, material is ejected from the surface of a protostar rotating at nearly break-up velocities. The ejected material is then travelling along the open magnetic lines of the protostar forming the outflow. In this scenario the surrounding disk is needed to explain the very fast rotation of the protostar. A significant drawback of this model is that, even though protostars have sufficiently strong magnetic fields, the rotation velocities required have not been observed in protostars.

Finally, the X-wind type models also assume that the stellar magnetic field is used to power the outflow. In this scenario though, the magnetic field is believed to be strong enough to truncate the disk at a certain
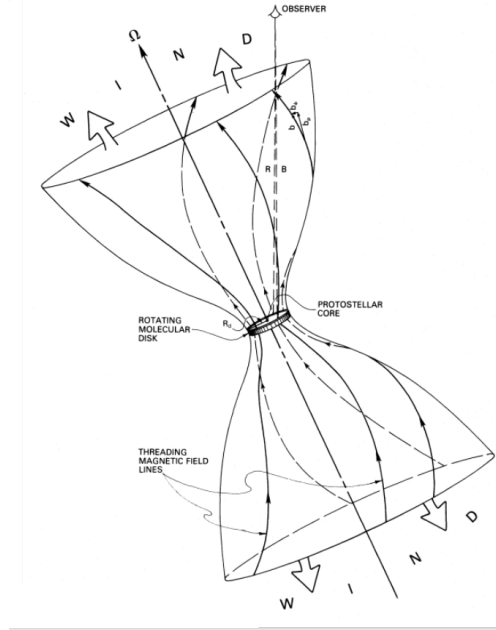
Figure 1: Illustration of the outflow structure for the disk-wind model (Pudritz & Norman 1986).

distance from the stellar surface. This interaction of the stellar magnetic disk also leads to a deceleration of the central protostar, in direct opposition with the assumption of the stellar winds models. At the area where the stellar magnetic field interacts with the disk there are both closed and open magnetic lines, therefore, the infalling disk material is either accreted to the central object through the closed magnetic lines or is swept up and accelerated into the outflow through the open magnetic lines (see Fig. 2). Interestingly, all proposed scenarios predict rotating outflows, with rotation speeds depending on the launching point, offering a means of determining the prevalent scenario. Such rotating outflows have been detected in a few cases (e.g. Lee et al. (2017); Tabone et al. (2017)) and point towards a wide angle MHD wind scenario, but are yet unable to rule out other solutions.

Regardless of the launching mechanism, a sketch of the expected structure of a protostar is shown if Fig. 3, where the protostar can be seen in the center, surrounded by its accretion disk and driving a bipolar outflow into the surrounding envelope.

1.2.3 Classification of protostars

Protostars are split into four categories, called Class 0, Class I, Class II and Class III. This classification is based on the observed spectral energy distributions of the protostars. The initial classification system from Lada (1987) only included the Class I, II and III sources, and was based on the spectral index α. The spectral index is defined as:

$$\alpha = \frac{\mathrm{d} \log(\lambda F_\lambda)}{\mathrm{d} \log(\lambda)} \tag{2}$$

with F_λ the emitted flux and λ the corresponding wavelength, for wavelengths from 1 μm to 20 μm. Sources with $0 < \alpha \leqslant 3$ where classified as Class I, while sources with $-2 \leqslant \alpha < 0$ as Class II and sources with $-3 < \alpha \leqslant -2$ as Class III. Class 0 sources are not visible in this wavelength range, and where therefore omitted from the initial classification. They where though later defined by Andre et al. (1993), using submillimeter observations, as the protostellar sources that have $\frac{L_{\mathrm{SMM}}}{L_{\mathrm{bol}}} > 0.5\%$. In Fig. 4 we give an example of the different protostellar classes and their corresponding spectra. The apparent excess of infra-red (IR) radiation, seen in Class 0 sources, is believed to be emitted by the envelope surrounding the protostar, which absorbs short wavelength radiation emitted from the central protostar and re-emits it at longer wavelengths. This excess radiation decreases progressively in Class I, II and III sources, which has
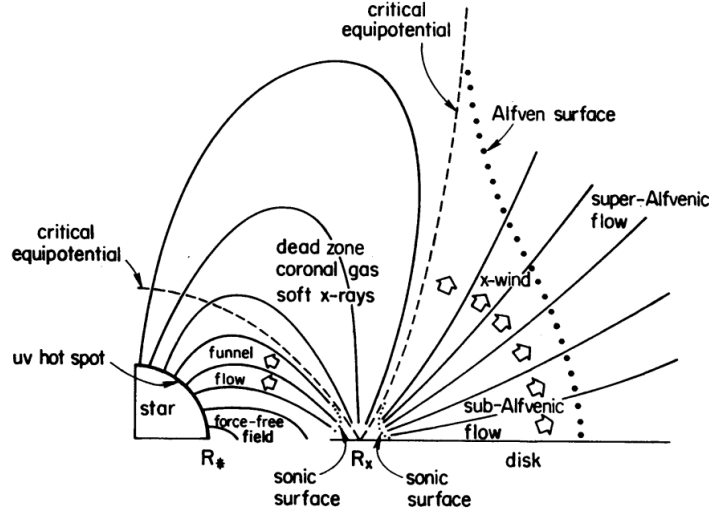
Figure 2: Illustration of the outflow structure for the X-wind model (Shu et al. 1994).

been interpreted as a result of protostellar sources being progressively less embedded going from Class 0 sources to Class III. With this interpretation the classification system is also connected to the evolutionary stage of the sources, with Class 0 sources being considered the less evolved sources and Class III the most evolved. This is a result of the protostellar outflows and radiation dispersing the surrounding material over time, thus leading to the progressive decrease in IR excess seen between Class 0 and Class III sources . This also means that over time Class 0 sources will evolve into Class I, then Class II and, in the end, Class III sources.

Interestingly, only Class 0 and I sources commonly appear to drive outflows and in addition, Class 0 protostars tend to drive outflows $\approx$ 10 times stronger when compared to Class I sources of similar and luminosity (Bontemps et al. 1996). This is believed to be the result of a decrease in the accretion rate of the protostar as it evolves, in combination with the fact that, as the surrounding envelope disperses, there is less material available to be entrained into the outflow (Mottram et al. 2017).

1.3 Observations of protostellar outflows

Protostellar outflows can be observed in many different ways, at various wavelengths and depending on the tracer used, a different part of the outflow becomes visible. Some examples are the visual and near-infrared (IR) emission lines of atomic H or forbidden transitions of atomic and ionized oxygen ([O$_\mathrm{I}$], [O$_\mathrm{II}$], [O$_\mathrm{III}$]) that can trace the atomic and ionized components of the outflows (see review from Bally (2016) for more details). For the cold molecular outflow that we focus on in this work, low-J rotational transitions of CO are most commonly used (e.g. Fukui et al. (1993); Wu et al. (2004)). The reason CO is primarily used for observing molecular outflows is that it is the second most abundant molecule, after only H$_2$, but also, contrary to H$_2$, it has very low rotational energy levels that are easily populated even in the cold and dense environment of the MCs. In addition to low-J CO emission lines that trace the bulk of the molecular outflows, emission from species like SiO and H$_2$O, whose abundance increases greatly in shocked areas, can provide information on the working surfaces of outflows and aid in constraining their borders.

CO observations of molecular outflows allow for a direct measurement of their morphological characteristics, like their extent and their collimation factor (the ration between the length and the width of the outflow). In addition, by measuring the doppler-shift of the CO emission, the velocity of the outflowing gas can be estimated. Finally, the integrated CO emission allows for the calculation of the molecular mass carried by the outflow (See Sec. 4.1 for a detailed explanation of the mass calculation method).
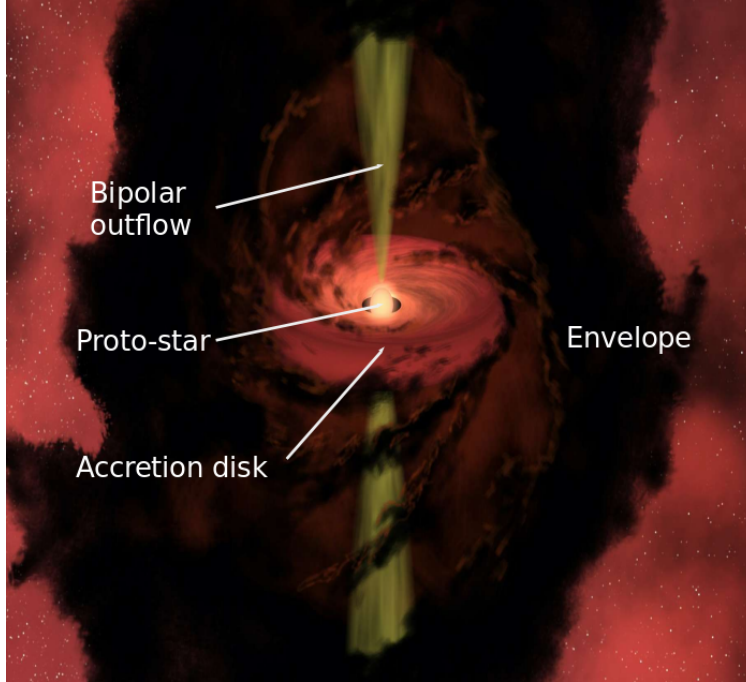
Figure 3: Illustration of a protostar and its surroundings.(By NASA/JPL-Caltech/R. Hurt (SSC) - Image of the day gallery, Public Domain, https://commons.wikimedia.org/w/index.php?curid=1280919)

1.3.1 The outflow force

One of the most interesting properties of an outflow, that can be inferred from observed quantities, is the outflow force (F_{CO}). More precisely the outflow force is the ratio between the total momentum carried by the outflow and the dynamical age of the outflow. It offers a measure of the rate at which the outflow injects momentum into the surrounding envelope and, overall, describes the strength of an outflow. There are several different methods used to calculate the outflow force (see van der Marel et al. (2013) for an in depth comparison of the various methods), but in principle the outflow force is given as:

$$F_{\mathrm{CO}} = \frac{P_{\mathrm{out}}}{t_{\mathrm{dyn}}},\tag{3}$$

where t_{dyn} is the dynamical time of the outflow and P_{out} its total momentum. The exact calculation of both parameters varies depending on the exact calculation method used, but as a general guideline the dynamical time offers an estimate of the lifetime of the outflow, and is calculated as:

$$t_{\mathrm{dyn}} = \frac{R_{\mathrm{lobe}}}{v_{\mathrm{out}}}\tag{4}$$

where R_{lobe} is the projected extent of the outflow, and can be directly measured from mapping the outflows and v_{out} is the velocity of the outflowing material. The total momentum is estimated as:

$$P_{\mathrm{out}} = M_{\mathrm{H_2}} v_{\mathrm{out}}.\tag{5}$$

Where $M_{\mathrm{H_2}}$ is the molecular mass carried by the outflow and v_{out} is again the velocity of the outflowing material. It is though important to note that different values of v_{out} are used in the different methods described in van der Marel et al. (2013) and in some cases a different v_{out} is used for calculating P_{out} and t_{dyn}. This is actually the parameter that most differentiates the various methods of outflow force calculation. Unfortunately all calculation methods suffer from significant uncertainties that mainly arise from uncertainties in the true inclination of the outflows, optical depth effects and uncertainties in the mass
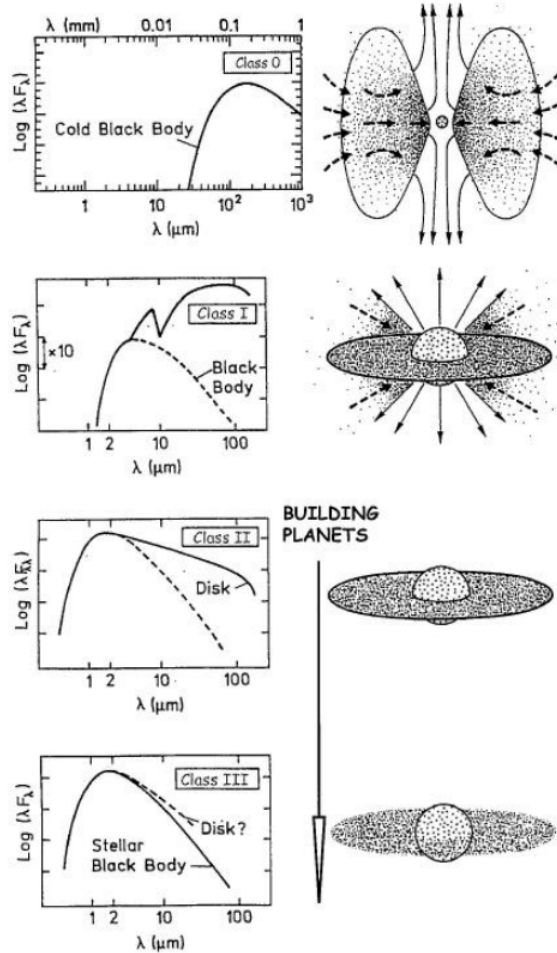
Figure 4: Illustration of the different evolutionary stages of protostars and their respective emission spectra (André 1993).

calculation. We will discuss the F_{CO} calculation method used in this work, and the uncertainties it contains, in more detail in Sec. 4.2.

What stands out regarding F_{CO} is an empirical correlation connecting the force with the mass (M_{env}) of the envelope surrounding the protostar (see Fig. 5 for an example). This correlation was first described in Bontemps et al. (1996) for a sample of, primarily, Class I low-mass protostellar sources, using CO [J=2-1] observations. At the same time Bontemps et al. (1996) also points out a decrease in outflow energetics for Class I sources in comparison to Class 0. This is interpreted as an evolutionary effect, as evolving protostars disperse their surrounding envelope over time, thus have a decreasing M_{env} which in turn, because of the aforementioned correlation, leads to a decrease in F_{CO}.

Later, using a sample of 26 massive and relatively isolated sources Beuther et al. (2002) found that this correlation extends also to in include high-mass protostellar sources. This was further strengthened with the results of Maud et al. (2015b), who examined outflows from 99 massive young stellar objects (MYSO's) and very compact H_{II} regions taken from the RMS [Red MSX source Survey (Lumsden et al. 2002, 2013)] sample. Interestingly, Beuther et al. (2002) also reports that the correlation appears tighter between Class I sources and high-mass sources, than it is for Class 0 sources, and tentatively suggests the absence of proper Class 0 equivalent phase for high mass protostars.

The low-mass sample has also been significantly expanded, since the first detection of the correlation, with more recent studies confirming its existence (e.g. Mottram et al. (2017); Yıldız et al. (2015)). In these
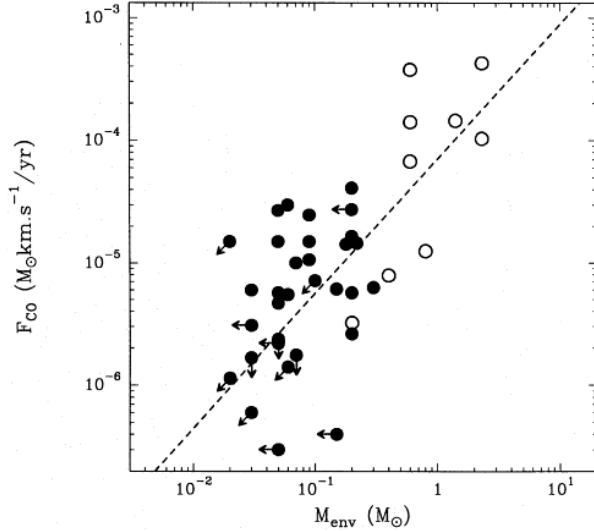
Figure 5: Outflow force (F_{CO}) over envelope mass for low-mass protostars. Open circles mark Class 0 sources while black circles mark Class I sources and the dashed line represents the best fit to the entire sample (Bontemps et al. 1996).

works Yıldız and Mottram also highlight the fact that, low-J CO observations, commonly used for the study of outflows, offer a view of the time averaged behaviour of the outflows and that, in order to probe the current outflow behaviour of a source, other tracers must be used (e.g. H_2O, O I or high-J CO transitions). The existence of this correlation is commonly believed to point to a connection between the M_{env} and the mass accretion rate ($\dot{M}_{acc}$), which is in turn connected to the outflows (Mottram et al. 2017; Duarte-Cabral et al. 2013).

Similar to the F_{CO} - M_{env} correlation, F_{CO} also has been found to correlate with the bolometric luminosity (L_{bol}) of the protostellar source (Cabrit & Bertout 1992). Interestingly, for this correlation Bontemps et al. (1996) reports a split between Class I and Class 0 sources, with Class I sources forming a much tighter correlation while Class 0 sources appear to drive consistently stronger outflow than Class I sources of similar L_{bol}. Again similar to the F_{CO} - M_{env} correlation, the F_{CO} - L_{bol} correlation was expanded to include high-mass sources (Beuther et al. 2002; Maud et al. 2015b) and the low mass sample has been significantly increased (Mottram et al. 2017; Yıldız et al. 2015) without significantly affecting the observed correlation. It is though noteworthy that, for the high-mass sources, Maud et al. (2015b) finds a shallower slope when compared to low mass sources, that when extrapolated to the low mass regime lands between Class 0 and Class I sources. The reason behind the shallower slope is currently uncertain, with Maud et al. (2015b) suggesting the possibility that the observed cores are in reality protoclusters and not single protostars driving a single outflow.

1.4 Extragalactic outflows

Apart from protostars, similar outflows, albeit on a much larger scale, are also observed originating from galaxies. These galactic-scale outflows are believed to be powered by accretion onto a central black hole or by a combination of stellar processes, like supernova explosions and star formation. This stems from the fact that extragalactic outflows are more commonly observed in galaxies hosting an active galactic nucleus (AGN) or a starburst. (See Veilleux et al. (2020) for a recent, in depth, review on galactic outflows, the energy sources behind them and their driving mechanisms). These galactic-scale outflows are typically observed either through P-Cygni profiles of OH transitions (e.g. Sturm et al. (2011); González-Alfonso et al. (2017)) or through broad line wings detected on CO line emission (e.g. Cicone et al. (2014); Fluetsch et al. (2019)). These observations also allow for the measurement of the characteristics of the detected outflows like their spatial extent, the velocities of the outflowing material as well as the total mass carried
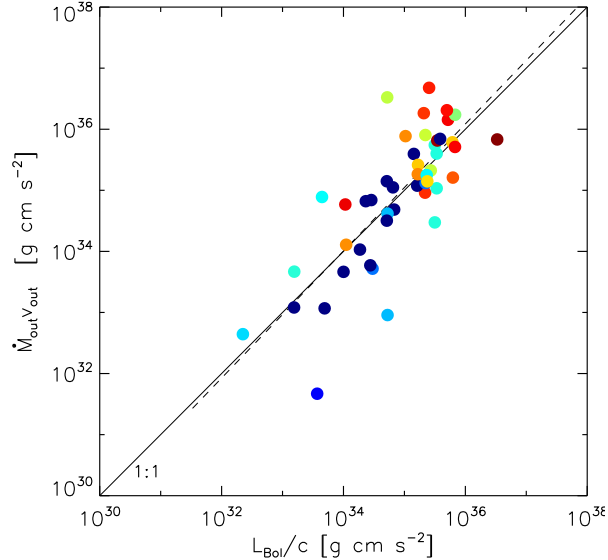
Figure 6: Outflow force (F_{CO}) over the bolometric luminosity momentum rate ($\frac{L_{bol}}{c}$ for extragalactic outflows in the local universe ($z < 0.2$). The continuous line represent the 1:1 relation. The colors mark the AGN contribution to the bolometric luminosity on a square root scale between 0 (dark blue) and 1 (dark red) (Lutz et al. 2020).

by the outflow (see Veilleux et al. (2020) for details). This in turn allows for the estimation of secondary properties of the outflows, like the mass outflow rate ($\dot{M}_{out}$) and the outflow force ($\dot{P}_{out}$)[1] in a way similar to that of the protostellar outflows. Measurements of extragalactic outflow forces have been carried out extensively for low-redshift ($z < 0.2$) sources (e.g. Cicone et al. (2014); González-Alfonso et al. (2017); Fluetsch et al. (2019); Lutz et al. (2020)) and have also recently expanded to include higher redshift sources ($z > 4$) (Spilker et al. 2020). Although the samples studied in these works had a significant overlap and were undeniably biased towards luminous star-forming systems and quasars, they allowed for the search of scaling relations between outflow properties and properties of the host galaxies. From their results, most interesting appears a correlation reported in (ref lutz 2020) between F_{CO} and L_{bol} of the host galaxy (see Fig. 6), as a similar correlation is detected in the case of protostars and their outflows (see Sec. 1.3.1). The similarities between protostellar and galactic outflows are further emphasized in Aalto et al. (2020), as the suggested magnetohydrodynamic launch mechanism that is proposed for the AGN driven narrow wind and molecular jet of NGC 1377 is expected to be similar to the suggested launch mechanism of protostellar winds!

1.5   The Cygnus-X molecular cloud

In this work we will examine ten intermediate- to high-mass sources located in the Cygnus-X molecular cloud. The Cygnus-X region was first detected as a strong, extended source of radio emission at a galactic longitude of $\approx 80\,\text{deg}$ from Piddington & Minnett (1952). Since then, extensive studies of the region have revealed a significant number of protoclusters and high-mass protostellar objects deeply embedded within massive, dense, dusty cores (Motte et al. 2007), a large number of ultra compact H$_{II}$ regions (Cyganowski et al. 2003) as well as a significant population of OB stars (Wright et al. 2010), including Cyg OB2 (Knodlseder 2000), one of the largest OB associations in our galaxy. Overall, Cygnus-X is considered to be one of the most intense star-forming regions nearby. In total, it is estimated that Cygnus-X has a mass of $\approx 4 \times 10^6 \text{M}_\odot$ and it extends over 100 pc in diameter (Leung & Thaddeus 1992) while the distance to its various substructures is found to range between 1.3 kpc for the nearest, W75, up to ≈ 3.3 kpc for AFGL 2591 (also called CygX-S26) (Rygl et al. 2012). Although it can be argued that AFGL 2591 is not actually located within the Cygnus-X complex, and that it simply lies along the same line of sight, this does not affect our results significantly, therefore AFGL 2591 is treated as part of the Cygnus-X complex for this work.

---

[1]Outflow forces are often noted differently in protostellar (F_{CO}) and extragalactic ($\dot{P}_{out}$) outflow studies, but in this work we will use the protostellar notation for both cases henceforth
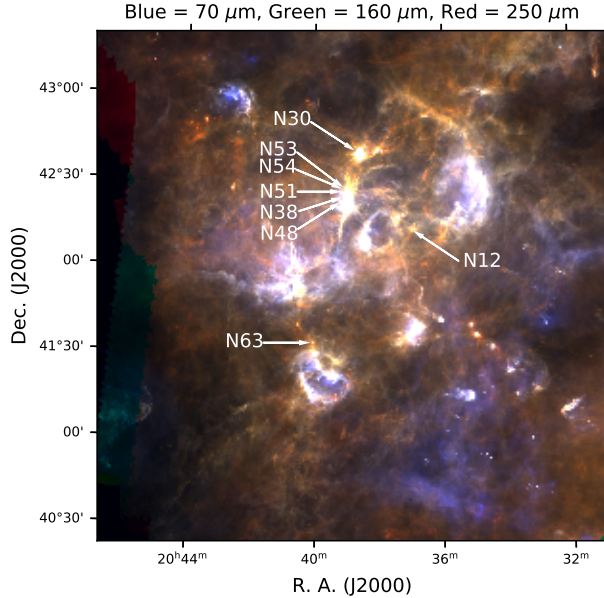
Figure 7: Part of the Cygnus-X molecular cloud containing the majority of the sources targeted in the PILS Cygnus survey (van der Walt et al. subm.). The image is comprised of observations at three different wavelengths, with 70 μm emission shown in blue, 160 μm in green and 250 μm in red. All observations were taken with Herschel.

1.5.1 The PILS Cygnus survey / The sources

The ten sources examined in this work, (CygX N12, N30, N38, N48, N51, N53, N54, N63, S8, S26) were the targets of the PILS Cygnus survey (Protostellar Interferometric Line Survey) (van der Walt et al. subm.), which is a large frequency-range line survey, covering 32 GHz of continuous frequency observations in the 345 GHz atmospheric window. All the observations for the survey where carried out with the SubMillimeter Array (SMA). The observations are described in more detail in section 2.

The majority of the targets in this survey, as can be seen in Fig. (7), are packed tightly in the same molecular cloud structure, while at the same time are located near the Cyg-OB2 association. These properties make them an ideal candidate for studies on the effects of clustered star formation on the evolution and properties of protostars.

1.6 The Sub-Millimeter Array

The Sub-Millimeter Array (SMA) is a radio interferometer operated by the Smithsonian Astrophysical Observatory (SAO) and the Academia Sinica Institute of Astronomy and Astrophysics (ASIAA), located at Mauna Kea in Hawai, a prime location for astronomical observations due to its high altitude (4.2 km above sea level) and dry climate. The array is operational since 2003, and currently consist of eight antennas with a diameter of 6 m each, that can cover baselines from 7 m up to 509 m. SMA covers a frequency range from 194 to 408 GHz, thus covering a large number of rotational transition of molecular species as well as continuum emission from interstellar dust grains. As such, the SMA is commonly used for observations of molecular clouds, high red-shift galaxies and the Galactic center. Finally, SMA also forms part of the Event Horizon Telescope, a global network of radio telescopes used to perform very long baseline interferometry and that produced the first ever image of a black holes event horizon.

1.7 Aims

In this thesis, we will look at CO [J = 3-2] and SiO [J = 8-7] line emission from the ten sources of the PILS Cygnus survey. Our aim is to search for outflow activity in these sources, and, in the cases where outflows are indeed detected, map them and calculate their outflow forces.

11

Figure 8: The Sub-Millimeter Array in Mauna Kea, Hawai. (Picture from Jonathan Weintroub `https://lweb.cfa.harvard.edu/sma/Photos/`.)

We then will compare our results with similar results from previous works, both for low-mass protostars (Yıldız et al. 2015; Mottram et al. 2017) and high-mass sources (Maud et al. 2015b), with regards to the $F_{\rm CO}$ - $M_{\rm env}$ correlation, in order to examine if and how clustered star formation affects the outflow forces of protostars. The nature of our sources, regarding their mass, will also enable us to attempt to connect the two relatively distinct data sets, of high- and low-mass sources.

Finally, through an extended literature search, we have gathered a significant sample of $F_{\rm CO}$ measurements from galactic outflows (Lutz et al. 2020; Fluetsch et al. 2019) and their corresponding luminosities. We aim to combine this sample with our protostellar sample in order to examine if the $F_{\rm CO}$ - $L_{\rm bol}$ correlation detected separately in both cases extends over the entire bolometric luminosity range or it is two entirely distinct correlations. The presence of a shared correlation between protostellar and galactic outflows is very interesting as it will strongly point towards the existence of a common driving mechanism behind the two types of outflows. The existence of such a mechanism would greatly aid in the research of understanding the actual launching mechanisms of outflow as it would add a significant constraint in the modeling of launch mechanisms, as they should now be able to explain both types of outflows and stay consistent over several orders of magnitude. At the same time, this would significantly expand the available sample for observations of outflows, both in number and in scales, by allowing the combined study of protostellar and extragalactic sources.

2 Observations

The PILS Cygnus survey, from which the CO [$J = 3$-2] and SiO [$J = 8$-7] data used in this work are taken, was carried out entirely with the Sub-Millimeter array (SMA), with use of the SWARM (SMA Wideband Astronomical ROACH2 [second generation Reconfigurable Open Architecture Computing Hardware] Machine) correlator.

For the observations, a combination of the compact and the extended configurations, available to the SMA, were used, with baselines ranging from 7 to 211 meters. Also, all ten sources of the survey were observed for approximately the same time over ten tracks, five of which in the compact configuration and the other five in the extended one. The compact configuration observations were carried out between the 27th of June and the 7th of August 2017, while the extended configuration observations were taken between the 20th of October and the 10th of November 2017. During this time, between 6 and 8 antennas where available in the array.

For all the observations, MWC349A was used as a complex gain calibrator, the quasars 3c273, 3c454.3 and 3c84 were used for bandpass calibration (depending on the exact time of the observation) and Neptune, Titan, Callisto and Uranus were used for the flux calibration. A more detailed breakdown of the observations is shown in the observations log in table 1.

The initial observations had a uniform spectral channel of $\approx$ 140 kHz, as provided by the SWARM correlator. These were then re-binned into a spectral resolution of $\approx$ 560 kHz, which corresponds to $\approx$ 0.48 km s^{-1}, in order to improve the noise level. The calibration of the data was performed with the Common Astronomy Software Applications (CASA) v4.7 (McMullin et al. 2007) as a part of van der Walt et al. (subm.). The data we received for this work consisted of the already calibrated measurement sets of the CO [$J = 3$-2] and SiO [$J = 8$-7] emission.

2.1 Data cleaning

Due to the nature of interferometric observations, the calibrated data represents the complex visibility ($V(u, v)$), which is the Fourier transform of the actual sky brightness $T(l, m)$. The $V(u, v)$ is defined on the spatial frequency plane, with u and v measured in wavelengths and $T(l, m)$ is defined on the sky dome, with l and m in radians. Unfortunately, in reality our observations only contain a sample $S(u, v)$ of the complex visibilities, as each pair of antennas (equivalent to a single baseline) returns the value of $V(u, v)$ at two points on the (u, v) plane. The sampled complex visibility can then be transformed into a modified image of the sky brightness ($T^{D}(l, m)$):

$$V(u, v)S(u, v) \xrightarrow{F} T^{D}(l, m) \tag{6}$$

$T^{D}(l, m)$ is a significantly distorted image of the sky brightness often called the "dirty" image. Applying the convolution theorem:

$$T(l, m)s(l, m) = T^{D}(l, m) \tag{7}$$

Table 1: Observing log of the PILS Cygnus survey.

Observing date	No of antennas	Configuration	Bandpass	Flux	Gain	$\tau(225 \text{ GHz})$
21/06/2017	7	COM	3c454.3	Titan, Neptune	mwc349a	0.05-0.07
22/06/2017	7	COM	3c273, 3c454.3	Titan, Neptune	mwc349a	0.10
27/06/2017	7	COM	3c454.3	Callisto	mwc349a	0.08
10/07/2017	7	COM	3c454.3	Callisto	mwc349a	0.05-0.06
07/08/2017	6	COM	3c84	Titan, Uranus	mwc349a	0.05
20/10/2017	8	EXT	3c84	Uranus	mwc349a	0.02-0.03
22/10/2017	7	EXT	3c84	Uranus	mwc349a	0.08-0.10
08/11/2017	8	EXT	3c84	Uranus	mwc349a	0.07
09/11/2017	7	EXT	3c84	Uranus	mwc349a	0.07
10/11/2017	8	EXT	3c84	Uranus	mwc349a	0.07

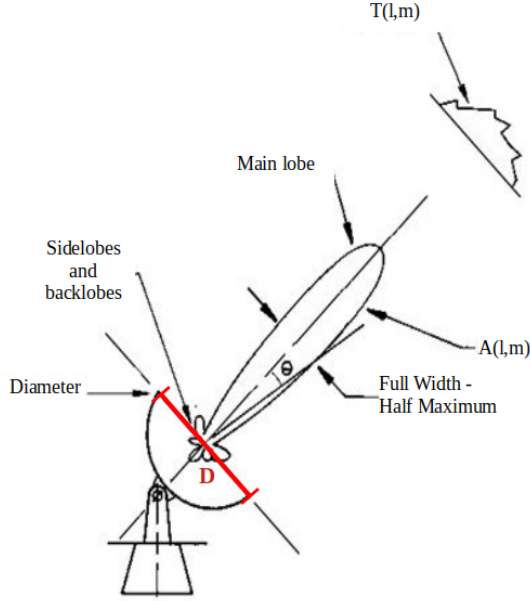**Notes.** Table from van der Walt et al. (subm.).

Figure 9: Illustration of an antennas response function, demonstrating the main and side lobes.

we see that the "dirty" image is the true sky brightness convolved with a point spread function (PSF) $s(l, m)$. This PSF is the Fourier transform of the sampling $S(u, v)$ and is often called the "dirty" beam and contains a lot of substructure due to the incomplete sampling of the (u, v) plane.

$T(l, m)$ is also distorted due to the antenna response $(A(l, m))$, which is not uniform. $A(l, m)$ drops quickly as we move away from the axis of the antenna, forming a main lobe with a "full width at half maximum" (FWHM) of $\approx \frac{\lambda}{D}$ (see Fig. 9). The antenna response modifies the sky brightness distribution, but its effects can be mostly corrected by dividing the image with $A(l, m)$. Unfortunately the antenna response apart of the main lobe also shows significant response some other specific angles, called sidelobes and can add significant artifacts to the image if they happen to fall on a bright source.

In order to remove these artifacts and reconstruct, as closely as possible, the true sky brightness, a process known as "cleaning" is necessary. Usually this is performed with the help of specialized software, like the `clean` command of CASA that is used in this work.

The process of cleaning the interferometric data is based on the assumption that the sky brightness can be described accurately as a collection of point sources. Under this assumption, the cleaning works by marking the highest peak in the area selected for cleaning, and then subtracting from the initial image the a "dirty" beam corresponding to a point source at the marked point and scaled by a gain parameter. The result of this subtraction is kept as the "residual" image and the location of the point source is kept in the "clean components" list. Then this process is repeated using the previous residual image as the initial image every time, until either the residual image peak falls under some threshold (usually it is a multiple of the rms noise or a fraction of the dirty image peak) or a maximum number of clean components is reached (this limit is arbitrary and carries no physical meaning).

At this point, the leftover residual image contains only noise and the clean components list contains all the point sources that represent the true sky brightness. In order to create a more realistic image of the sky, called the "clean" image, we convolve all the point sources with the "clean" beam, which is an elliptical gaussian fit to the main lobe of the "dirty" beam, and finally we add the residual image. The resulting clean image represent the best estimate of the true sky brightness.

It is important to mention that there is no unique, optimal way of cleaning interferometric data, but in this work, in order to achieve the best possible results we performed our cleaning in CASA v4.7 using the `clean` command with the following parameters:

14

- `field = ''`, which corresponds to the selection of all available fields.

- `spw = ''`, which corresponds to the selection of all available spectral windows.

- `selectdata = True`, which means that all available data is selected.

- `mode = 'frequency'`, sets the spectral grids in units of frequency.

- `niter = 2000`, sets the maximum number of iterations performed by the clean command.

- `outframe = 'LSRK'`, sets the output images spectral frame as the conventional local standard of rest.

- `gain = 0.1`, is the gain parameter applied for each cycle of the clean command.

- `threshold = '0.1Jy'`, sets the flux level at which cleaning stops.

- `psfmode = 'clark'`, sets the method of PSF calculation during the minor cycles.

- `usescratch = False`, as to not save model visibilities

- `interactive = True`, in order to open the casa display panel and allow for manual selection of the areas to clean.

- `imsize = [256,256]`, sets the size of the output image in pixels.

- `cell = '0.2arcsec'`, sets the output pixel size.

- `weighting = 'briggs'`, sets the weighting method to be used on $S(u, v)$.

- `robust = 2.0`, sets the free parameter of the Briggs weighting function.

Using the interactive mode of the clean command opens up the display panel of CASA, in which a specific area of the $T^D(l, m)$ can be manually marked to be cleaned. We selected this approach as it allowed us to better handle the extended and wildly varying CO emission. Selecting the 'clark' algorithm, as the method of PSF calculation, means that the cleaning is split into minor and major cycles. During the minor cycles the brightest points are detected, and an approximation of the true PSF is used for the subtractions. Then, in the major cycle, the points found during the minor cycles are subtracted correctly by applying the full PSF. The Briggs weighting function that is used is:

$$w_{ik} = \frac{1}{S^2 + \sigma_{ik}^2} \tag{8}$$

where σ_{ik} is the rms noise of the (i,k) cell of the (u, v) plane and S is a parameter defined as:

$$S^2 = \frac{(5 \times 10^{-R})^2}{\overline{w}} \tag{9}$$

where R is the robust parameter and $\overline{w}$ is the average variance weighting factor. Setting the robust parameter to 2 mean that the Briggs weighting function approximates the natural weighting:

$$w_{ik} = \frac{1}{\sigma_{ik}^2} \tag{10}$$

Applying a natural weight throughout the cleaning process, yields the lowest σ_{rms} possible in the final image.

In order to achieve the best possible result with our cleaning, we strove, in our manual selection of areas to clean, to prioritize the areas with the brightest emission among all channels. Next we selected areas displaying emission over an extended number of channels and finally we selected areas with a clearly dominant emission over a single channel. We selected these areas as they are most likely corresponding to real emission, and are not artifacts introduced due to the nature of interferometric observations. At the same time, we avoided areas near the edges of the data cubes as, due to the reduced sensitivity of the antennas as we move away from the center of their field of view (FOV), they are not considered trustworthy. In Fig.
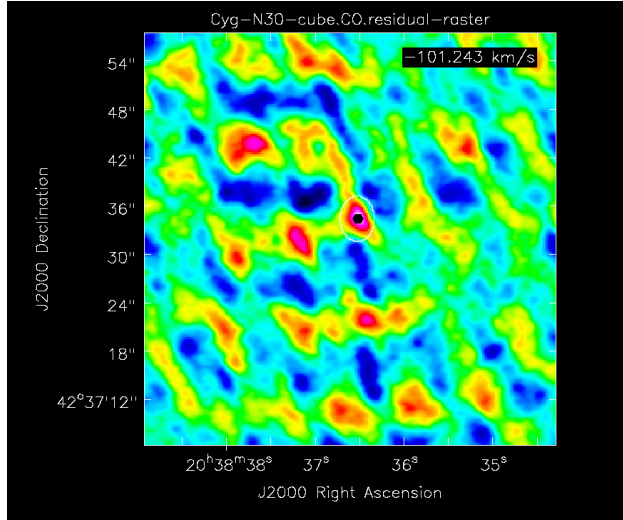
Figure 10: Residuals map of N30, taken from the CASA display panel during the cleaning process. The area selected to be cleaned is marked with a white contour. The black hexagon is added later to better highlight the selected area.

10 we show an example of an area marked for cleaning in the display panel of CASA. The area is marked with a white contour, and the black spot is added afterwards for clarity.

The final clean data cubes have, as set in the `clean` parameters, a size of 256×256 pixels, with a pixel size of 0.2 arcseconds. For the CO data, the initial spectral resolution of 0.48 km s^{-1} is maintained, but for the SiO data it was changed to $\approx$1.93 km s^{-1}, in order to improve its signal-to-noise (S/N) ratio. This was achieved by setting the `width` parameter, in the `clean` command, to '2234144Hz'. We show in Fig. 11 an example of the integrated emission of N30 over velocities -60 $< v <$ 60 km s^{-1} with and without cleaning, to highlight the importance of the cleaning process.

The resulting beam sizes, as well as single channel σ_{rms} for all sources are shown in table 2. We note here that, the beam sizes vary slightly over the frequency channels, but that change is $< 1\%$, with the exception of a few starting channels that have larger beam sizes. This difference, in the edge channels, arises from the selective cut-out of small parts at the edge of the spectra, where the receivers efficiency drops. The removed part of the spectra is not the same for all antennas, and as a result, the edge channels of our data correspond to observations from less antennas, which leads to them having larger beam sizes. These channels though display no actual emission, and are therefore not taken into account. Finally the σ_{rms} was estimated as $\sigma_{rms} = \sqrt{\langle I \rangle^2}$ with $\langle I \rangle >$ the mean value of the intensity for all pixels in the selected channel, for two separate channels, one near the start of the data and one near the end, both showing no line emission. The final σ_{rms} presented in table 2 is calculated as the mean of these two values.
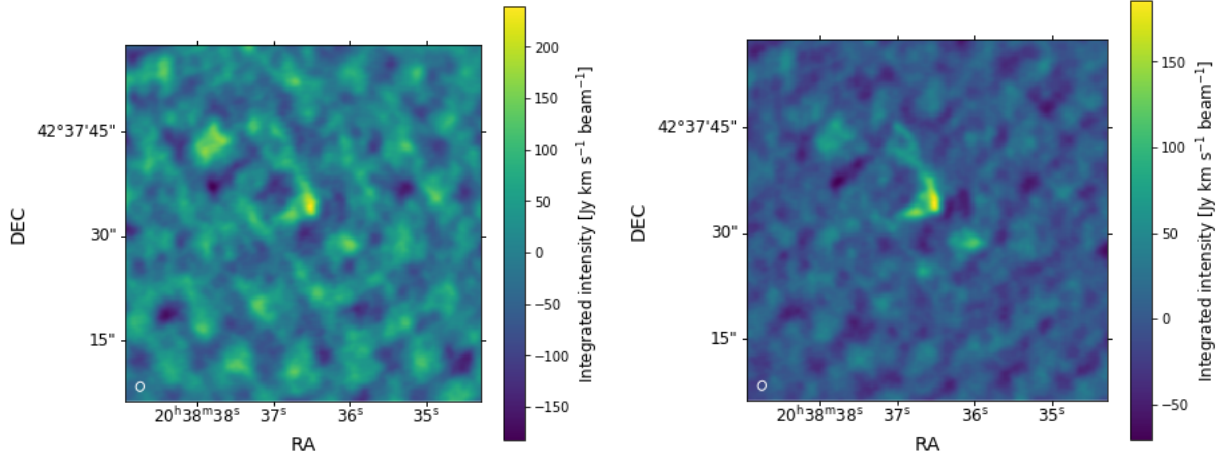
Figure 11: CO $[J = 3\text{-}2]$ integrated intensity map of N30 over velocities $-60 < v < 60$ km s^{-1} relative to source velocity. The image on the left is constructed using the CO data without cleaning, while the image on the right is constructed using the same data after performing the cleaning.

Table 2: Final beam sizes and σ_{rms} for the cleaned CO and SiO data.

Source	CO σ_{rms} [Jy beam^{-1}]	BMAJ [arcsec]	BMIN [arcsec]	BPA [deg]	SiO σ_{rms} [Jy beam^{-1}]	BMAJ [arcsec]	BMIN [arcsec]	BPA [deg]
N12	0.15	1.24	1.08	85.7	0.09	1.19	1.04	70.7
N30	0.28	1.35	1.19	75.0	0.10	1.29	1.14	56.1
N38	0.19	1.38	1.19	71.0	0.08	1.34	1.18	91.0
N48	0.16	1.37	1.13	76.6	0.09	1.30	1.11	77.4
N51	0.18	1.25	1.05	83.0	0.10	1.21	1.03	-85.0
N53	0.15	1.19	1.01	82.1	0.08	1.14	0.99	86.8
N54	0.15	1.21	1.04	-80.9	0.08	1.23	1.07	88.5
N63	0.17	1.24	1.11	88.7	0.09	1.26	1.12	82.2
S8	0.21	1.22	1.12	87.3	0.08	1.21	1.11	87.2
S26	0.21	1.40	1.25	77.0	0.11	1.39	1.24	76.9

Notes. The σ_{rms} presented here is calculated for a single channel, with channel width of 0.48 km s^{-1} for CO and 1.93 km s^{-1} for SiO.

3 Outflow maps

The integrated CO emission revealed bipolar outflows originating from all ten sources of the PILS Cygnus survey. We present these outflows in Fig. 16 as contour plots over the continuum emission of the corresponding source. The red contours correspond to the red-shifted CO emission and similarly the blue contours denote the blue-shifted emission. SiO integrated emission, although not always significantly detected, is shown in white contours. All contour levels are plotted starting at a 3 σ level and increase in increments of 3 σ, with σ being, in each case, the rms noise of the corresponding integrated emission. These were calculated from a 100×100 pixel area near the edge of each image, carefully selected as to not contain any outflow emission. From now on we will refer to them as σ_{red}, σ_{blue} and σ_{SiO} for the red-shifted, blue-shifted and SiO integrated emission image respectively.

The velocity ranges used to integrate the blue and red-shifted CO emission, as well as the SiO emission are given in table 3. For the CO observations, we refer to the velocities closest to the source velocity as "inner" velocities, noted as $v_{\mathrm{r,in}}$ and $v_{\mathrm{b,in}}$ for the red and blue-shifted range, while the furthest velocities are called "outer" and are similarly noted as $v_{\mathrm{r,out}}$ and $v_{\mathrm{b,out}}$. For SiO a single range is used in the integration and thus only the outer limits are given, with v_{r} being the maximum red-shifted velocity and v_{b} the maximum blue-shifted velocity. In order to determine the proper velocity range for each source, and ensure, to the best degree possible, that no part of the outflow is missed, we used several spectra. Initially we took the spectrum from the location of peak continuum emission. We show in Fig. 12 the location and the corresponding spectrum in the case of N12 as an example. We then made an initial estimate for the velocity range covered by the outflow, which is shown with the blue and red marked areas plotted over the spectrum. The selection of the velocity ranges was done as to best cover the entirety of the broad line wings, starting from the peak of their emission and extending at least until they reach the continuum level. In several cases though (e.g. N12, N48, N53), the spectrum taken in the continuum peak location, shows only one clear line wing. In these cases, the velocity range of the missing line wing was taken to be closely symmetrical to the velocity range determined by the line wing that was present.
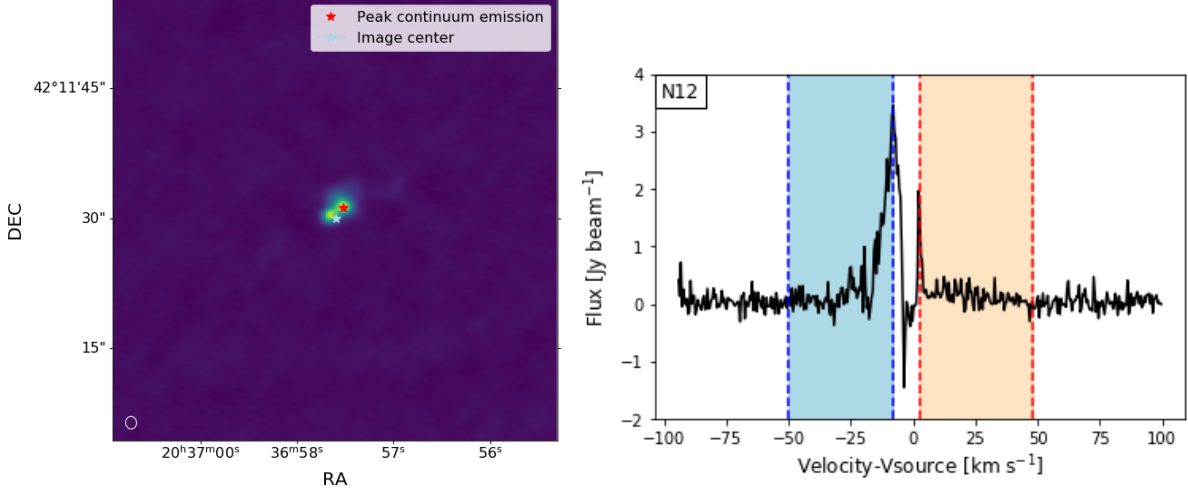

Figure 12: [Left]: Continuum emission of N12, with the location of the peak marked with a red star and the center of the image with a light blue star.[Right]: Spectrum of N12 from the location of peak continuum emission. The blue and red marked areas correspond to the initial guesses for the velocity range of the blue and red-shifted emission respectively.

To further strengthen our velocity range estimates, and to obtain proper velocity ranges in the cases a line wing was missing, we used the initial velocity estimates to determine the locations where the red- and blue-shifted emission peaks. We then extracted the spectra from these locations, and used them to adjust the velocity ranges. Using again N12 as an example, we show in the top of Fig. 13 the location of the red- and blue-shifted peaks with a red and blue star, respectively and in bottom left and right the corresponding spectra. More precisely, on the left we have the spectrum from the peak of the red-shifted emission, with

the matching velocity range marked in red, and similarly on the right is the spectrum of from the peak of the blue-shifted emission again with the corresponding velocity range marked in blue.
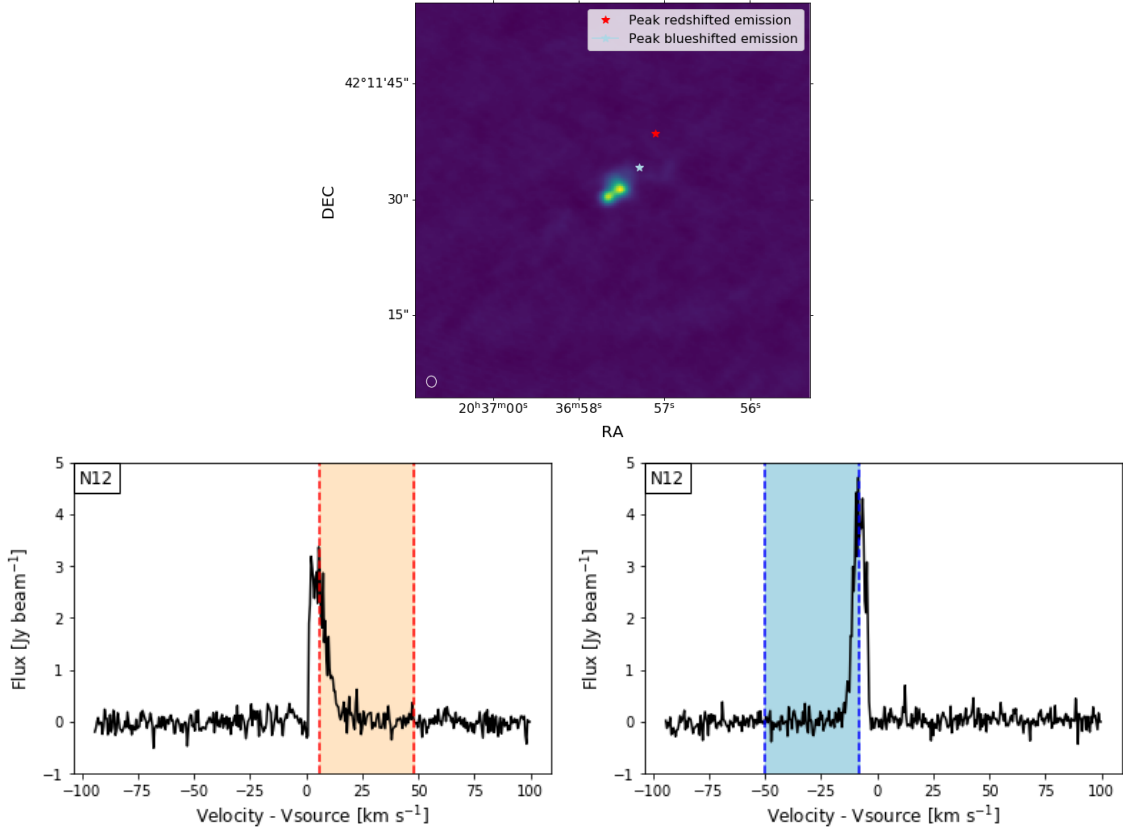

Figure 13: [Top]: Continuum emission of N12, with the location of the peak marked with a red star and the center of the image with a light blue star. [Left]: Spectrum of N12 from the location of peak red-shifted emission. Marked in red is the velocity range adopted for the red-shifted part of the outflow. [Right]: Spectrum of N12 from the location of peak blue-shifted emission. Marked in blue is the velocity range adopted for the blue-shifted part of the outflow.

As a final test for the velocity ranges, we created an initial set of integrated emission images using the velocity ranges estimated so far and extracted the spectra from the locations of peak integrated red- and blue-shifted emission. We show in Fig. 14 and 15 these locations and the corresponding spectra for N12 as an example. If the selected velocity range matched well the line wings present in these spectra, it was adopted, otherwise it was adjusted in order to properly match. These final velocity ranges are the ones presented in Table 3, and used for the remainder of this work. The spectra used for determining the velocity ranges for all the sources can be found in Appendix A.

In almost all of the spectra used for deducing the velocity ranges for the integration of the CO emission, strong absorption is seen around the source velocity v_{source}. This is a result of the optical thickness of the CO at these velocities and spatial filtering effects. Spatial filtering is a result of interferometric observations, and the fact that there is a minimum possible distance between two antennas which leads to a minimum observed baseline. This lower limit in baselines means that the interferometer cannot detect large scale structures. In the case of outflows, this means that emission in the lower velocities, where the outflow is more extended is often missing. The combination of these two effects has implications in our following results that will be discussed later.

For the SiO emission a single velocity range was used, covering continuously the entire range, from red to blue-shifted emission. This velocity range was determined as to maximize the S/N ratio in each case and to give the best possible detection at a 3 σ level. As the SiO emission detected was overall weak, and not very extended, it was only used as an additional tool assisting in determining the origin of the CO outflows,
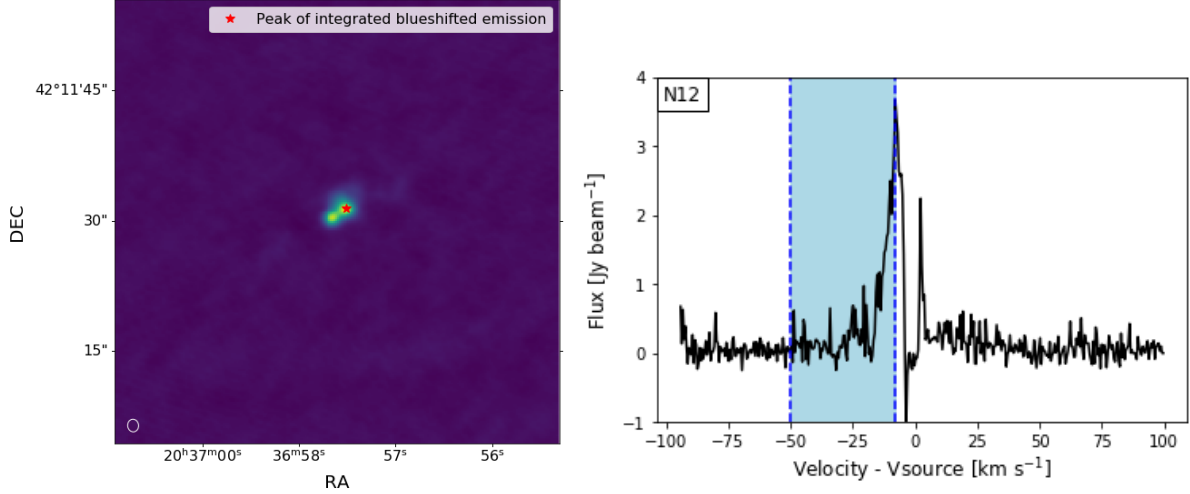
Figure 14: [Left]: Continuum emission of N12, with the location of the peak of the integrated blue-shifted CO emission marked with a red star.[Right]: Spectrum of N12 from the location of the peak of the integrated blue-shifted emission. The blue marked area corresponds to the velocity range used in the integration of the blue-shifted emission.
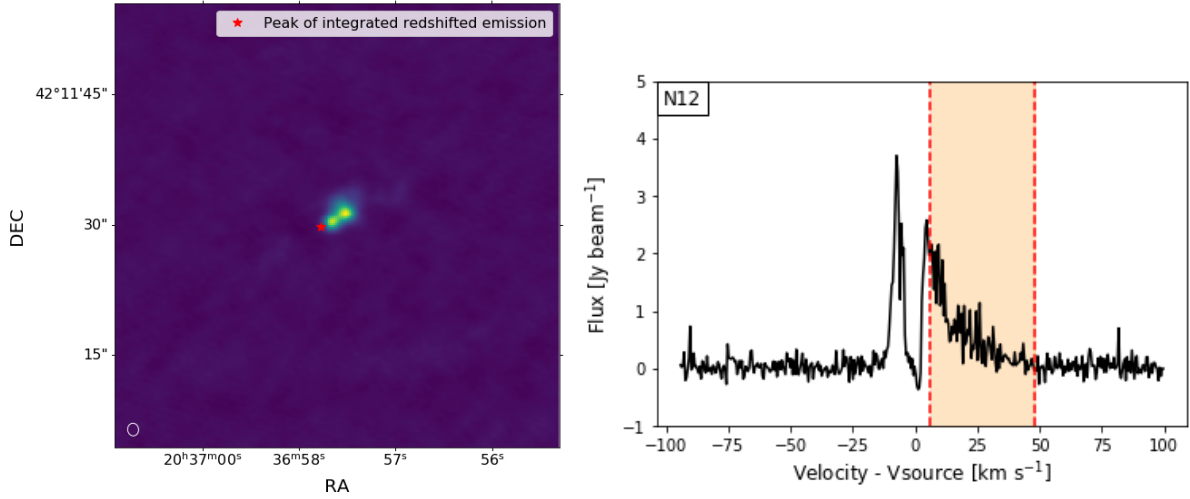

Figure 15: [Left]: Continuum emission of N12, with the location of the peak of the integrated red-shifted CO emission marked with a red star.[Right]: Spectrum of N12 from the location of the peak of the integrated red-shifted emission. The red marked area corresponds to the velocity range used in the integration of the red-shifted emission.

we therefore refrained from examining it in more detail.

Regarding the outflows, in the majority of the sources, a clear bipolar outflow structure is clearly visible, and in most cases appears to be originating from the continuum sources but there are several noteworthy cases. Firstly in N38 only a compact outflow is detected, that appears to originate from a weak, secondary, continuum peak, located slightly above the primary peak. The presence of, relatively strong, SiO emission from the same location strengthens the argument that this is indeed the actual source of the outflow. We note as well at this point that the outflow of N38 is significantly weaker than that of the other sources of our sample, and the image presented in Fig. 16 is scaled up significantly compared to the rest. N30 also appears irregular, showing a significant dissimilarity between its two lobes, with the red-shifted part of the outflow appearing significantly stronger and close to the continuum peak, that we identify as the source of the outflow, while the blue-shifted part of the outflow is small and further away from the continuum peak.

Table 3: Velocity limits for the integration of CO and SiO emission.

Source	CO				SiO	
	$v_{\text{r,in}}$ [km s^{-1}]	$v_{\text{r,out}}$ [km s^{-1}]	$v_{\text{b,in}}$ [km s^{-1}]	$v_{\text{b,out}}$ [km s^{-1}]	v_{b} [km s^{-1}]	v_{r} [km s^{-1}]
N12	6	48	−8	−50	−30	30
N30	6	51	−24	−69	−30	30
N38	2	33	−7	−20	−20	20
N48	6	55	−2	−55	−10	10
N51	4	40	−12	−40	−15	15
N53	8	55	−13	−60	−15	15
N54	3	53	−8	−58	−10	10
N63	15	55	−14	−55	−20	20
S8	3	25	−13	−35	−25	25
S26	9	35	−24	−50	−10	10

This we believe to be a result of strong blue-shifted absorption, seen on the spectra used to determine the velocity integration limits, that pushed the inner blue-shifted velocity significantly further away from the source velocity comparatively with the red-shifted one (For N30 $v_{\text{b,in}} = -24$ km s^{-1} while $v_{\text{r,in}} = 6$ km s^{-1}). In the case of N48, an elongated blue-shifted structure is detected slightly to the North-East of the continuum source. This structure is, as mentioned in Duarte-Cabral et al. (2013), the outflow of IS-1 and therefore not taken into account for this study. Looking next into N53, it is clear that, even though there are two distinct continuum peaks, the CO outflow is only originating from the western peak, which might suggest that the second core is yet to enter a protostellar phase. In addition, due to the close proximity of N53 to N54, the second is also visible in the continuum emission of N53 as a secondary peak towards the South-East corner of the field of view (FOV). Similarly, when looking into N54, N53 can clearly be seen towards the North-West corner of the image. Also, because the outflow of N53 is significantly stronger than that of N54 it can also be seen in the contour maps of N54, but is of course not taken into account in this case. In both cases another outflow shaped structure can be seen, straight to the South of N53 and to the West of N54. There appears to be no continuum emission connected to this structure, and it is not taken into account in this work. Finally, in the case of S8, we consider the outflow to originate from the area of extended continuum emission under the primary peak, and traveling along the plane of the sky. In this case, one of the outflow lobes is seen in both red and blue-shifted emission near the image center, while the second lobe is only visible in the red-shifted CO emission extending towards the East. In addition, a fairly strong red-shifted structure appears above the main continuum peak, but lacks a matching blue-shifted lobe and is therefore not considered an outflow and is not used for the subsequent outflow force calculation.
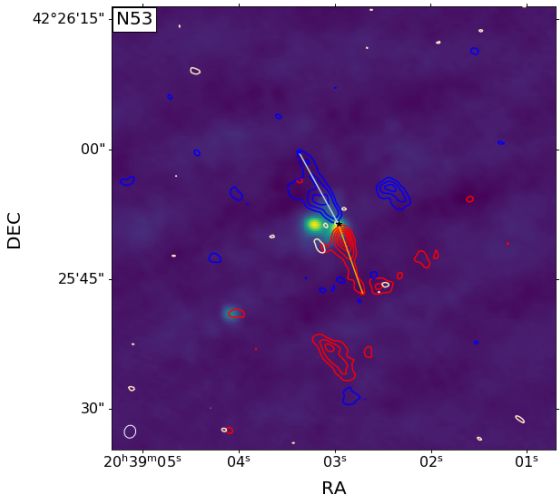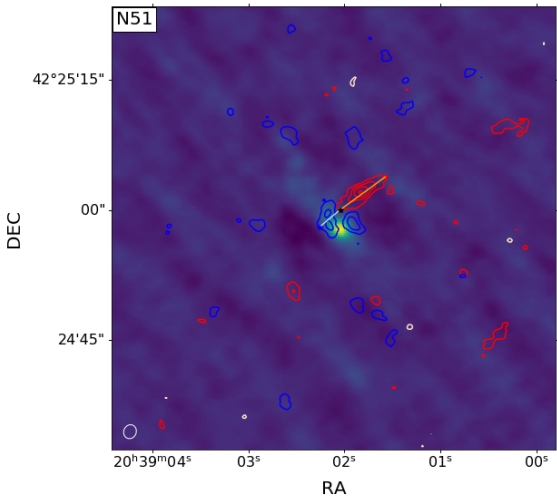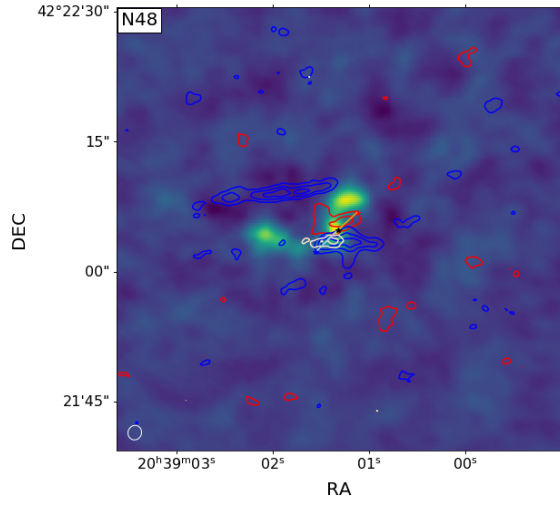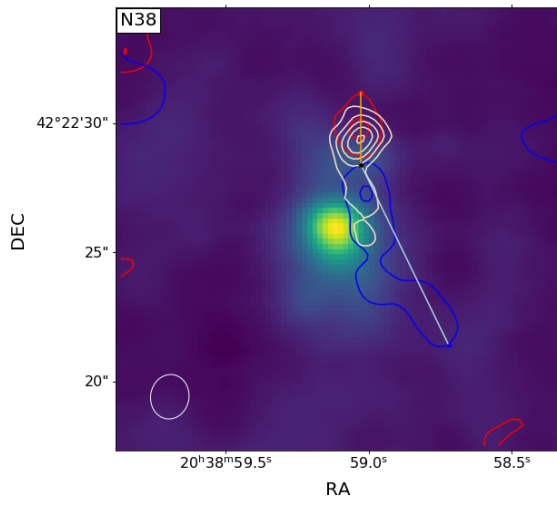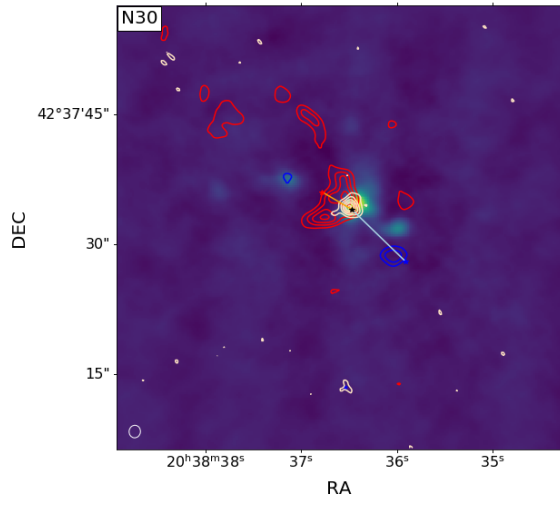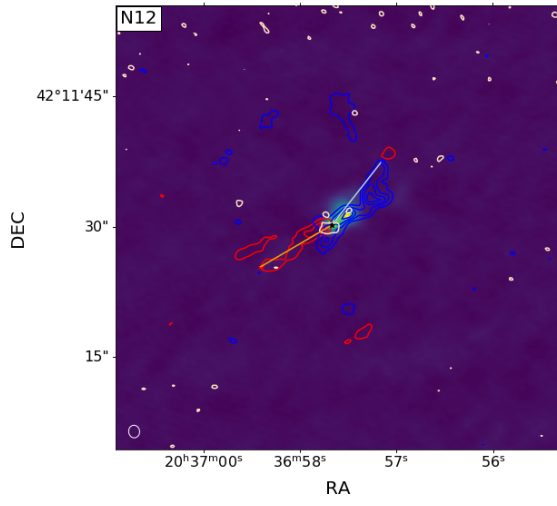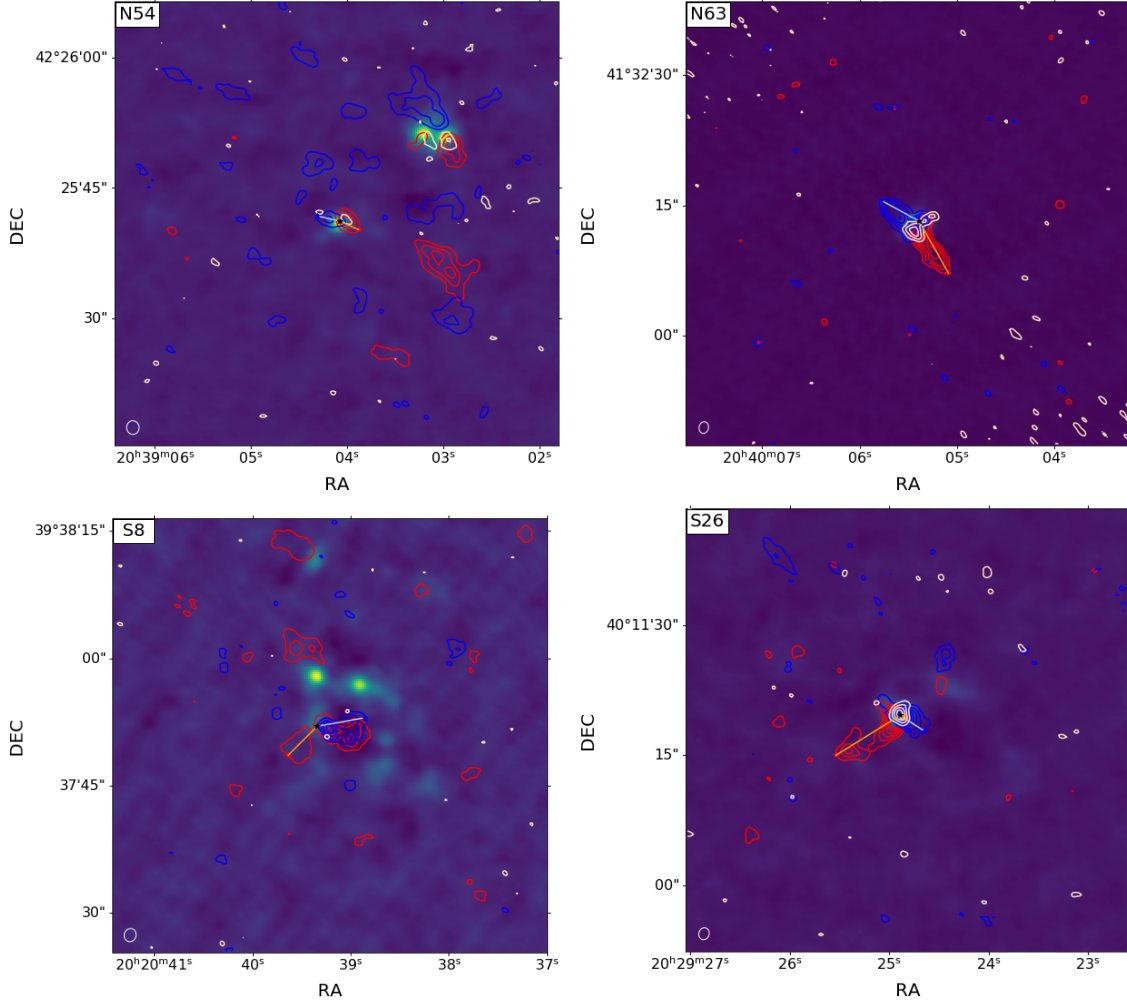
Figure 16: Continuum emission of the sources of the PILS Cygnus survey. Displayed in red contours is the red-shifted CO emission, in blue contours is the blue-shifted CO emission and in white contours is the integrated SiO emission. All contour levels are set at 3,6,9,12,15 of the σ_{rms} noise of the corresponding integrated emission.

4 Outflow forces

As mentioned in Sec. 1.3.1, over the years of outflow studies many different methods of calculating the outflow forces have been developed. A detailed comparison of these methods was presented in van der Marel et al. (2013) which showed that, use of different calculation methods can result in uncertainties of up to a factor of 6. In the same work, the separation method is found to be the least affected by observational uncertainties, and is therefore suggested as the preferred method to calculate F_{CO}.

4.1 Mass derivation

Before discussing the details of the separation method, it is important to discuss the method used to estimate the mass of the outflows, since it is crucial for the final F_{CO} calculation, and is also shared among all methods presented in van der Marel et al. (2013). To be precise, the outflow mass can be calculated, from observations of CO emission lines, with only a few, reasonable, assumptions. First, the emission needs to be optically thin, which we assume to be the case for the outflows, and then we must assume that the gas is in local thermodynamic equilibrium and therefore has a single excitation temperature. Dunham et al. (2014) found

that the correction for optically thickness mostly arises from the velocities nearest to the source velocity, and even then has a small effect to the final results. More over van der Marel et al. (2013) reports that when using outflow velocities > 3 km s^{-1} (similar to the ones used in this work) the effects of assuming optically thick emission are smaller than a factor of 2. This uncertainty is significantly smaller than those introduced to the final results by other factors, for example the inclination angle, therefore it is safe to assume optically thin emission for the entire outflow. We can also safely assume LTE as the typical density for the cores $\approx 7 \times 10^4$cm^{-3} is higher than the critical density for the CO [$J = $ 3-2] line $\approx 3.2 \times 10^4$cm^{-3} (see Appendix A from Maud et al. (2015a)) Therefore we can now measure the column density of the upper state of the observed transition:

$$N_{\mathrm{u}} = \frac{8\pi k_{\mathrm{B}}}{hc^3} \frac{\nu^2 \int T_{\mathrm{B}} \mathrm{d}v}{A_{\mathrm{ul}}} \tag{11}$$

Where k_{B} is Boltzmann's constant, h is Planck's constant, c the speed of light, ν the frequency of the emission line and T_{B} the brightness temperature, which is connected to the observed intensity as $I_\nu = \frac{2kT_{\mathrm{B}}}{c^2} \nu^2$. Finally the integral is over the velocity range covered by the outflow as to give the integrated intensity. From here, the total column density of CO can be calculated using the Boltzmann distribution as:

$$N_{\mathrm{CO}} = \frac{Q_{(T_{\mathrm{ex}})}}{g_{\mathrm{u}}} \mathrm{e}^{(E_{\mathrm{u}}/k_{\mathrm{B}} T_{\mathrm{ex}})} N_{\mathrm{u}} \tag{12}$$

where $Q(T_{\mathrm{ex}})$ is the partition function, g_{u} the degeneracy of the upper level, E_{u} the energy of the upper level and T_{ex} the excitation temperature of the observed gas. If we now multiply the CO column density with a conversion factor $\left[\frac{\mathrm{H}_2}{\mathrm{CO}}\right]$ connecting the CO and H$_2$ abundances, we get the total column density of H$_2$. Then, the total mass of the outflow can be calculated as:

$$M = \mu m_{\mathrm{H}} N_{\mathrm{H}_2} A \tag{13}$$

where μ is the mean molecular weight, m_{H} the hydrogen mass and A is the area we integrate over.

4.2 Separation method

As the separation method, was suggested by van der Marel et al. (2013) as the preferred F_{CO} calculation method, it is the method we elected to mainly use for this study. In this method, the outflow momentum (P_{out}) and the dynamical time (t_{d}) are treated as separate parameters. The dynamical time is calculated by using the maximum outflow velocity (v_{max}) as v_{out} in Eq. 4, at the same time, for the momentum, the velocity-weighted integrated intensity is used instead of the separate mass and velocity calculation of Eq. 5. This approach is chosen as it offers a better estimate of the actual outflow momentum, since it takes into account the kinematic structure of the outflow (Downes & Cabrit 2007; Curtis et al. 2010). So, the outflow force for the separation method is calculated as:

$$F_{\mathrm{CO}} = c_3 \times \frac{K \left(\sum_{\mathrm{j}} \left[\int_{v_{\mathrm{in}}}^{v_{\mathrm{out,j}}} T(v')v'\mathrm{d}v' \right]_{\mathrm{j}} \right) v_{\mathrm{max}}}{R_{\mathrm{lobe}}} \tag{14}$$

with the calculation being performed for each outflow lobe individually and then summed up for the total F_{CO}.

In Eq. 14, c_3 is a correction factor for the inclination of the outflow, and can take the values shown in table 4 according to the inclination angle of the outflow. The values were interpolated by van der Marel et al. (2013) from the ratios in the third column of Table 6 of Downes & Cabrit (2007), where $\alpha = 90 - i$, which are based on a long-duration numerical simulation of a protostellar jet model in a molecular cloud. Determining the inclination angle of an outflow is still a fairly uncertain process, since there is no way to properly measure it and the estimations are usually based on morphological comparisons between observed and model created outflow maps (Cabrit & Bertout 1990). Due to these uncertainties, c_3 takes four different values that represent broad inclination angle ranges. We assume that $i = 10°$ corresponds to inclination

angles of $0°$ to $30°$, $i = 30°$ to angles from $30°$ to $50°$, $i = 50°$ to angles from $30°$ - $70°$ and $i = 70°$ to angles from $50°$ to $70°$ similar to van der Marel et al. (2013).

K is the conversion factor used to calculate mass from integrated intensity. By combining Eq. 11, 12, 13 we get that the mass is given by:

$$M = \mu m_{\mathrm{H}} A \left[\frac{\mathrm{H}_2}{\mathrm{CO}} \right] \frac{Q(T_{\mathrm{ex}})}{g_{\mathrm{u}}} \mathrm{e}^{(E_{\mathrm{u}}/k_{\mathrm{B}} T_{\mathrm{ex}})} \frac{8\pi k_{\mathrm{B}} \nu^2}{hc^3 A_{\mathrm{ul}}} \int T_{\mathrm{B}} \mathrm{d}v \tag{15}$$

Therefore,

$$K = \mu m_{\mathrm{H}} A \left[\frac{\mathrm{H}_2}{\mathrm{CO}} \right] \frac{Q(T_{\mathrm{ex}})}{g_{\mathrm{u}}} \mathrm{e}^{(E_{\mathrm{u}}/k_{\mathrm{B}} T_{\mathrm{ex}})} \frac{8\pi k_{\mathrm{B}} \nu^2}{hc^3 A_{\mathrm{ul}}} \tag{16}$$

where as A we now use now the physical area covered by one pixel.

Next, the sum $\sum_{\mathrm{j}}$ of the integrated intensities is performed over all pixels contributing to the outflow, in order to give the total velocity-weighted, integrated intensity of the outflow. The integration itself is performed for each pixel separately, with velocity limits v_{in} and $v_{\mathrm{out,j}}$. The lower velocity limit, v_{in} is the same for all pixels, but $v_{\mathrm{out,j}}$ is calculated individually for each pixel as the highest velocity at which the intensity remains above the $1\,\sigma_{\mathrm{rms}}$ level. Then the maximum outflow velocity, v_{max}, used for the calculation of t_{dyn}, is taken as the maximum (in absolute value for the blue-shifted lobes) of $v_{\mathrm{out,j}}$ for each outflow lobe. Finally, for R_{lobe} the projected extent of the outflow lobe is used.

In this work, we calculated the outflow forces using all four values of c_3 as to both, make up for the uncertainty inherent into determining the inclination angle of an outflow, but also, examine the effect these uncertainties actually have on the final result.

For the calculation of the conversion parameter K, we used a mean molecular weight $\mu = 2.8$, in order to also take into account He (Kauffmann et al. 2008), a CO to H_2 conversion factor $\left[\frac{\mathrm{H}_2}{\mathrm{CO}} \right] = 1.2 \times 10^4$ (Frerking et al. 1982) and an excitation temperature $T_{\mathrm{ex}} = 100$ K, as used in van der Marel et al. (2013). We adopt this T_{ex} as similar temperatures have been previously measured for CO $[J = 3\text{-}2]$ (van Kempen et al. 2009; Yıldız et al. 2012, 2013) and changes of $\pm\,30$ K only infer changes of $\approx$ 10 - 20% (Yıldız et al. 2015) thus the 100 K assumption is accurate enough and also allows for a direct comparison with results from van der Marel et al. (2013). The values used for the partition function $Q = 36.5$, the upper level degeneracy $g_{\mathrm{u}} = 7$, the upper level energy $E_{\mathrm{u}} = 33.2$ K and Einstein A coefficient $A_{\mathrm{ul}} = 10^{-5.6}$ s^{-1} are taken from splatalogue (https://splatalogue.online/advanced1.php). In addition, the frequency of the CO $[J = 3\text{-}2]$ is used in units of Hz, the hydrogen mass m_{H} in kg, Boltzmann's constant in J K^{-1}, Planck's constant in J s and the speed of light c in km s^{-1}. Lastly, the pixel area A is calculated as:

$$A = (\text{pixel size} \cdot \frac{3600}{206265} d)^2 \tag{17}$$

with the pixel size in degrees taken from the image header and d the distance to the source. Here we have assumed a distance of 1.3 kpc for all sources except S26 which has a distance of 3.3 kpc. The initial calculation of K yields a result in units of $\frac{\mathrm{s}^3 \mathrm{Hz}^2 \mathrm{kpc}^2 \mathrm{kg}}{\mathrm{Kkm}^3}$ which we multiply with a conversion factor of $1.478 \times 10^{16} \frac{\mathrm{km}^3 \mathrm{M}_\odot}{\mathrm{kg\ pcHz}^2 \mathrm{kpc}^2 \mathrm{s}^2}$ in order to convert K to more appropriate units of $\mathrm{M}_\odot$ s K^{-1} pc^{-1}.

Then, in order to properly determine the pixels contributing to the outflow, we initially take a cutout surrounding the outflow, in order to avoid including unrelated structures in our measurements, and then sum up all the pixels that have an integrated intensity higher than the $3\sigma_{\mathrm{rms}}$ (σ_{red} and σ_{blue} for the red and blue-shifted lobe respectively) level used in the contour maps of the outflows (Fig. 16). For the integration of the velocity-weighted intensity of the outflows, the first step is converting our data from units of Jy beam^{-1} to K, in order to match the units used in van der Marel et al. (2013), by multiplying with $\frac{1.22 \times 10^6}{\nu^2 \cdot \mathrm{BMAJ} \cdot \mathrm{BMIN}}$ with ν the observed emission line in GHz and BMAJ, BMIN the beam major and minor axis in arcseconds (see [https://science.nrao.edu/facilities/vla/proposing/TBconv] for

details regarding the conversion from Jy beam^{-1} to K). Then we create the velocity-weighted data cube by multiplying each channel with the corresponding velocity. Finally for the limits of the integration we use, for the lower limit v_{in} the inner velocities $v_{b,in}$ and $v_{r,in}$ shown in table 3 and for the upper limit we use $v_{out,j}$, calculated as described previously, using as σ_{rms} limit the single channel rms noise of each source, presented in table 2.

What remains now is to estimate the dynamical time of the outflows, for which v_{max} and R_{lobe} are needed. v_{max} is easily calculated as the maximum (in absolute value for the blue-shifted outflow lobes) of the $v_{out,j}$ previously measured while R_{lobe} is measured directly from the outflow maps. The values of v_{max} and R_{lobe} measured for our sample are given in table 5.

The resulting outflow forces, for all sources and the four representative inclination angles are given in table 6.

Table 4: Inclination correction factors.

$i(°)$	10	30	50	70	Ref
c_1	0.28	0.45	0.45	1.1	1,2
c_2	1.6	3.6	6.3	14	1
c_3	1.2	2.8	4.4	7.1	3

References. (1) Cabrit & Bertout (1990), (2) Cabrit & Bertout (1992), (3) Downes & Cabrit (2007).

4.3   Other calculation methods

Apart from the separation method, we decided to use two additional methods, from the ones described in (ref vdm 2013) to calculate F_{CO} for all sources in our sample. The additional methods used were, the v_{max} method (Method 1 in van der Marel et al. (2013)) and the $\langle v \rangle$ method (Method 3 in van der Marel et al. (2013)). The v_{max} method was selected because, according to van der Marel et al. (2013), it is the most commonly used method in the literature, therefore presenting F_{CO} measurements of our sample with the v_{max} method might prove useful for further comparisons with similar works. The $\langle v \rangle$ method, on the other hand, was selected because it is used by Maud et al. (2015b) for the calculation of the outflow forces of his high-mass protostellar sample. As we aim to compare the results of our work with this sample, having the measurements in both methods will allow us to estimate if any observed difference in F_{CO} is true, or is inferred by the calculation method used.

The calculation of the outflow force for both methods is very similar to the separation method so we will not go into detail here. In short, for the v_{max} method:

$$F_{CO} = c_1 \times \frac{K \left(\sum_j \left[\int_{v_{in}}^{v_{out,j}} T(v') dv' \right]_j \right) v_{max}^2}{R_{lobe}} \tag{18}$$

with c_1 the corresponding inclination angle correction given in table 4 and the rest of the parameters calculated as in the separation method (see section 4.2). For the $\langle v \rangle$ method:

$$F_{CO} = c_2 \times \frac{K \left(\sum_j \left[\int_{v_{in}}^{v_{out,j}} T(v') v' dv' \right]_j \right)^2}{R_{lobe} \sum_j \left[\int_{v_{in}}^{v_{out,j}} T(v') dv' \right]_j} \tag{19}$$

with c_2 again being the corresponding inclination correction factor, given in table 4. The rest of the calculation is performed as for the separation method, with only difference that v_{max} is not needed in this case.

The outflow forces, as measured with the v_{max} and $\langle v \rangle$ methods are presented in tables 7 and 8 respectively.

Table 5: Maximum outflow velocities and extents of outflow lobes used in the calculation of outflow forces.

	Red-shifted		Blue-shifted	
Source	v_{max} [km s^{-1}]	R_{lobe} [pc]	v_{max} [km s^{-1}]	R_{lobe} [pc]
N12	28.4	0.060	−21.5	0.059
N30	53.3	0.025	−51.3	0.054
N38	10.1	0.018	−24.3	0.049
N48	15.1	0.019	−27.1	0.023
N51	13.0	0.041	−22.9	0.020
N53	14.9	0.053	−39.3	0.060
N54	30.4	0.015	−16.6	0.017
N63	52.4	0.043	−45.4	0.032
S8	17.6	0.030	−34.2	0.036
S26	37.0	0.139	−40.5	0.053

4.4   A quick comparison of methods

For a quick comparison of the outflow forces of the PILS Cygnus survey sources, as calculated using the separation, the v_{max} and the $\langle v \rangle$ methods, we plot in Fig. 17 the F_{CO} as measured with the v_{max} method, and in Fig. 18 those of the $\langle v \rangle$, over those measured using the separation method. This comparison reveals small differences, with the results varying by less than an order of magnitude. A result that agrees well with the differences of up to a factor of 6 that van der Marel et al. (2013) reports among all calculation methods discussed therein. We note as well, again in agreement with van der Marel et al. (2013), that the separation method appears to give the highest results, with the exception of few sources measured with the $\langle v \rangle$ method and for an assumed inclination angle of 70°.

Focusing on the comparison between the separation method and the $\langle v \rangle$ method (Fig. 18 reveal a difference between the methods that is, in almost all cases, less than a factor of 2. The very small difference found between the two methods is important as it means that a direct comparison between results from (ref maud 2015) and other works that used the separation method, is possible, and not significantly affected from the selection of outflow force calculation method.

Regarding the different inclination angles, for all three methods, we see that the difference, even between the most extreme cases of going from a "face on" outflow to an outflow close to the plane of the sky, the change in the resulting outflow force is smaller than an order of magnitude. Therefore, even though constraining the precise inclination angle of an outflow is difficult, this uncertainty does not affect the measured outflow force significantly.

Table 6: F_{CO} calculated with the separation method for the red-shifted lobe, the blue-shifted lobe and the whole outflow.

$i(°)$	10			30			50			70		
Source	F_{red}	F_{blue}	F_{total}	F_{red}	F_{blue}	F_{total}	F_{red}	F_{blue}	F_{total}	F_{red}	F_{blue}	F_{total}
N12	3.0	5.8	8.8	6.9	13.4	20.3	10.9	21.2	32.1	17.6	34.2	51.8
N30	193.8	35.5	229.4	452.3	82.9	535.2	710.8	130.2	841.0	1146.9	210.2	1357.1
N38	0.7	2.4	3.1	1.6	5.7	7.3	2.5	9.0	11.5	4.0	14.5	18.5
N48	3.6	7.1	10.7	8.5	16.6	25.1	13.3	26.1	39.5	21.5	42.2	63.7
N51	1.2	7.4	8.6	2.9	17.3	20.2	4.5	27.3	31.8	7.3	44.0	51.3
N53	0.8	19.6	20.4	2.0	45.6	47.6	3.1	71.7	74.8	5.0	115.7	120.7
N54	4.6	2.3	6.9	10.7	5.5	16.2	16.8	8.6	25.4	27.1	13.8	40.9
N63	21.7	30.8	52.5	50.6	71.8	122.4	79.5	112.8	192.4	128.4	182.1	310.4
S8	5.9	12.7	18.6	13.8	29.6	43.4	21.6	46.5	68.1	34.9	75.1	110.0
S26	42.5	76.9	119.4	99.1	179.5	278.6	155.8	282.0	437.8	251.3	455.1	706.4

Notes. All results are shown in units of 10^{-5} M$_{\odot}$ km year^{-1} s^{-1} .
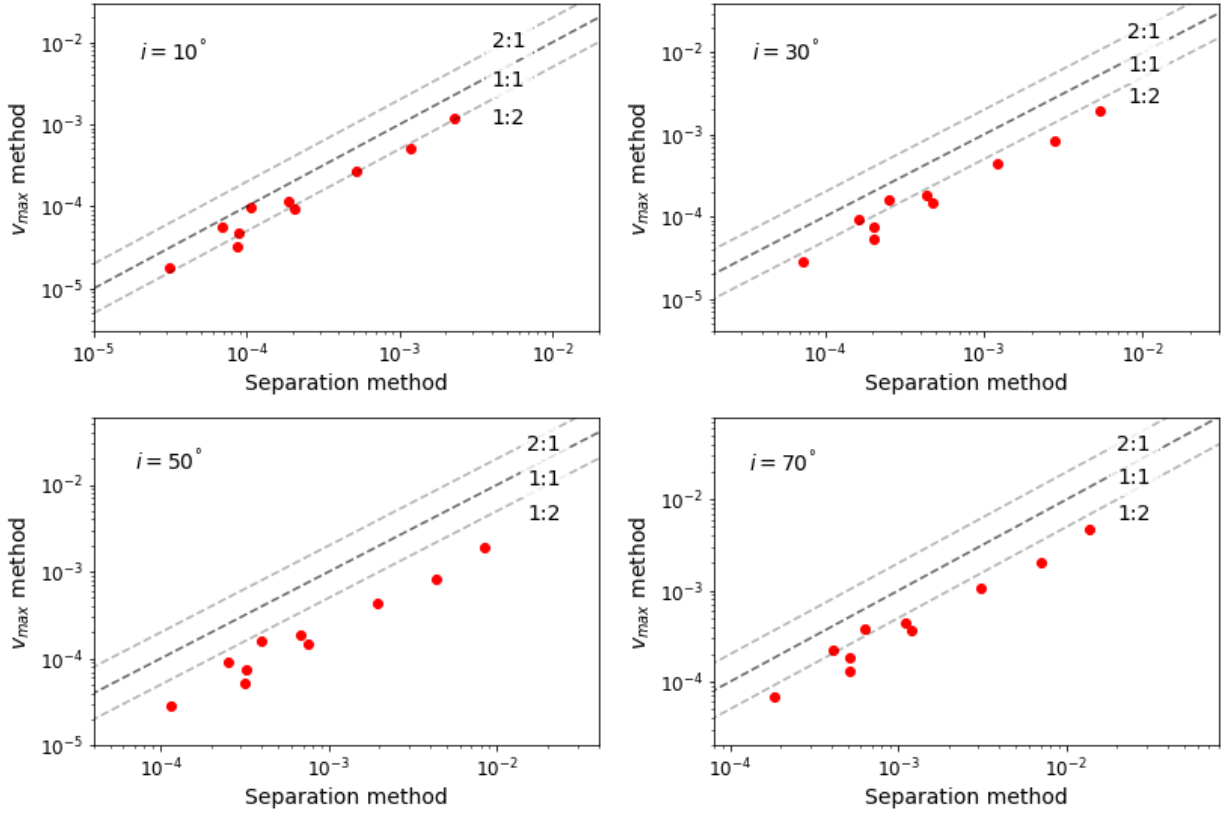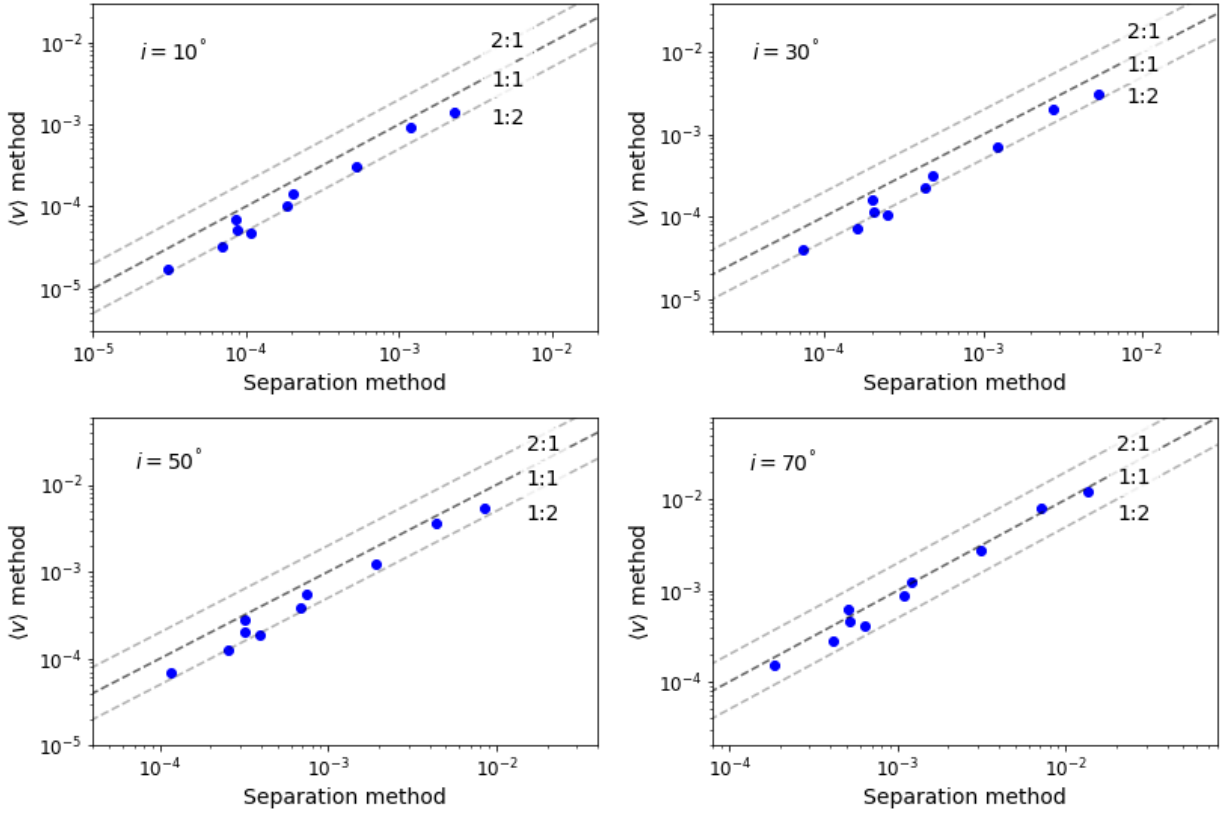
Figure 17: Comparison of outflow forces for the 10 sources of the PILS Cygnus survey, measured using the $v_{\max}$ (y-axis) and the separation method (x-axis), for inclination angles of $10°$ (top left), $30°$ (top right), $50°$ (bottom left) and $70°$ (bottom right). We plot also in dashed grey lines the 2:1, 1:1 and 1:2 ratios.

Table 7: F_{CO} calculated with the $v_{\max}$ method for the red-shifted lobe, the blue-shifted lobe and the whole outflow.

$i(°)$		10			30			50			70	
Source	F_{red}	F_{blue}	F_{total}	F_{red}	F_{blue}	F_{total}	F_{red}	F_{blue}	F_{total}	F_{red}	F_{blue}	F_{total}
N12	2.0	2.7	4.7	3.2	4.4	7.6	3.2	4.4	7.6	7.7	10.8	18.5
N30	107.4	12.8	120.2	172.6	20.6	193.1	172.6	20.6	193.1	421.8	50.3	472.1
N38	0.3	1.5	1.8	0.5	2.3	2.8	0.5	2.3	2.8	1.2	5.7	6.9
N48	1.5	8.3	9.8	2.4	13.4	15.8	2.4	13.4	15.8	5.8	32.8	38.6
N51	0.6	2.7	3.3	0.9	4.4	5.3	0.9	4.4	5.3	2.3	10.7	12.9
N53	0.3	8.9	9.2	0.4	14.3	14.7	0.4	14.3	14.7	1.1	35.0	36.1
N54	4.7	0.9	5.6	7.6	1.5	9.1	7.6	1.5	9.1	18.6	3.6	22.2
N63	11.4	16.1	27.5	18.3	25.9	44.2	18.3	25.9	44.2	44.6	63.4	108.0
S8	5.0	6.4	11.4	8.0	10.4	18.4	8.0	10.4	18.4	19.4	25.3	44.8
S26	25.7	26.1	51.8	41.4	41.9	83.3	41.4	41.9	83.3	101.1	102.5	203.6

Notes. All results are shown in units of 10^{-5} $M_\odot$ km year^{-1} s^{-1} .

Figure 18: Comparison of outflow forces for the 10 sources of the PILS Cygnus survey, measured using the $\langle v \rangle$ (y-axis) and the separation method (x-axis), for inclination angles of $10°$ (top left), $30°$ (top right), $50°$ (bottom left) and $70°$ (bottom right). We plot also in dashed grey lines the 2:1, 1:1 and 1:2 ratios.

Table 8: F_{CO} calculated with the $\langle v \rangle$ method for the red-shifted lobe, the blue-shifted lobe and the whole outflow.

$i(°)$		10			30			50			70	
Source	F_{red}	F_{blue}	F_{total}	F_{red}	F_{blue}	F_{total}	F_{red}	F_{blue}	F_{total}	F_{red}	F_{blue}	F_{total}
N12	1.4	3.8	5.2	3.2	8.5	11.7	5.5	14.9	20.5	12.3	33.2	45.5
N30	108.9	30.7	139.6	245.0	69.0	314.0	428.7	120.8	549.5	952.7	268.4	1221.1
N38	0.4	1.3	1.7	1.0	2.9	3.9	1.7	5.1	6.8	3.8	11.4	15.2
N48	2.8	1.9	4.7	6.3	4.3	10.6	11.0	7.5	18.5	24.5	16.6	41.1
N51	0.8	6.3	7.1	1.8	14.3	16.1	3.2	24.9	28.1	7.2	55.4	62.6
N53	0.8	13.4	14.2	1.8	30.1	31.9	3.1	52.6	55.7	7.0	116.9	123.9
N54	1.4	1.8	3.2	3.1	4.2	7.3	5.4	7.3	12.7	12.1	16.2	28.3
N63	12.9	18.2	31.1	29.0	41.0	70.0	50.8	71.9	122.6	112.8	159.7	272.5
S8	2.2	7.8	10.0	4.9	17.5	22.4	8.6	30.6	39.2	19.1	68.0	87.1
S26	21.8	70.5	92.3	49.1	158.7	207.7	85.9	277.6	363.5	190.8	617.0	807.8

Notes. All results are shown in units of 10^{-5} $M_\odot$ km year^{-1} s^{-1} .

5 The Outflow Force - Envelope Mass correlation of proto-stellar outflows

Protostellar outflows are found to follow a correlation with the mass of their surrounding envelope (Bontemps et al. 1996). This correlation hints to a connection between the mass of the envelope and the accretion proccess, which is in turn connected to the launch of the outflows (Duarte-Cabral et al. 2013; Mottram et al. 2017). As this correlation was also found to extend to the high-mass protostars (Beuther et al. 2002), it also strongly supports that high- and low-mass protostars form in a similar way (Maud et al. 2015b). The presence of the F_{CO} - M_{env} correlation allows us to properly understand our F_{CO} measurements, by plotting them against their respective envelope masses in Fig. 19 and comparing them with this established correlation. In addition, by examining the F_{CO} - M_{env} correlation for our combined sample of both low- and high-mass protostars, will hopefully enable us to connect these two otherwise distinct samples.

We plot our measurements using colored points, to differentiate between the various sources. The location of the point denotes the mean value of F_{CO} for the different inclination angles, while the errorbars mark the minimum and maximum F_{CO} that corresponds to inclination angles $i = 10°$ and $i = 70°$ respectively. To aid us in this comparison, we plot alongside our results in Fig. 19, similar measurements from previous studies. More precisely, using empty red circles and triangles, we show the Class 0 and Class I sources of the low-mass sample from Yıldız et al. (2015), using filled blue circles and triangles, we show the Class 0 and Class I sources of the low-mass sample from Mottram et al. (2017) and finally with grey squares we mark the high-mass sample from Maud et al. (2015b).

All three of these studies use, similar to this study, CO $[J = 3\text{-}2]$ observations, therefore it is safe to assume that they trace the same parts of their respective outflows. In addition we note that, while Yıldız et al. (2015) and Mottram et al. (2017) use the separation method for calculating F_{CO}, Maud et al. (2015b) uses the $\langle v \rangle$ method. As shown in Sec. 4.4, the $\langle v \rangle$ method, on average, varies from the separation method by less than a factor of 2. This uncertainty is significantly smaller than the inherent uncertainties of the F_{CO} measurements, as for example the inclination angle, therefore a direct comparison of the different measurements is reasonable.

Finally, in Fig. 19 we also show, with a blue dashed line, the best fit on the F_{CO} - M_{env} correlation as found in van der Marel et al. (2013), for a low-mass sample of protostars and using CO $[J = 3\text{-}2]$ observations.

5.1 Clustered star formation

The PILS Cygnus survey sources, examined in this work are, in their majority, tightly packed in the same molecular cloud structure and located in close proximity to the Cyg-OB2 association, one of the largest OB associations in our galaxy, they therefore are a prime example of clustered star formation. On the other hand, the sample used by Maud et al. (2015b) specifically contained isolated high mass sources. Comparing the results of the two studies, shown in Fig. 19, we find that the PILS Cygnus sources are in good agreement with results for sources of similar mass by Maud et al. (2015b), suggesting that clustered star formation does not significantly impact the outflow activity of protostars. An exception to this is N38, who appears to have a slightly weaker outflow than sources of similar mass. As discussed in Sec. 3, N38 has only a compact outflow, that originates from secondary continuum peak close to the main peak which causes great uncertainty for its final mass that will be discussed later. Even so, given the large scatter of the high-mass sample, N38 could still be considered to follow the same correlation as the rest.

Since outflow activity is closely tied to accretion into the central protostar, the conclusion we reach, that clustered star formation has no impact on protostellar outflows, would also imply that clustered star formation has no effect on the accretion processes of the protostars. This in turn would imply that, the surrounding environment, where a protostar forms, does not play a significant role in the accretion, and that, accretion processes are governed by local processes connected the protostar itself.

5.1.1 The envelope masses

The envelope masses of our sources, used to plot the F_{CO} - M_{env} correlation in Fig. 19, are mostly taken from Pitts et al. (in prep.), who used SED fitting of Herschel observations assuming a distance of 1.4 kpc. The masses are then scaled to the distance of 1.3 kpc assumed in this work, with the exception of S26 that was

initially calculated from Pitts et al. (in prep.) for the distance of 3.3 kpc that we also assume. For sources N38 and N54 no envelope masses where found in Pitts et al. (in prep.), therefore we use older measurements from Motte et al. (2007), which again we scale to the new distance of 1.3 kpc. The envelope masses assumed for all sources of the PILS Cygnus survey are given in table 9.

Pitts et al. (in prep.) used SCUBA 450 μm observations to determine the size of the envelopes in order to measure their mass. These observations have a resolution of 14 arcseconds, ideal for observing the extended envelopes, that have typical sizes of ≈ 0.1 pc (or 17 arcseconds at the distance of 1.3 kpc of the Cygnus-X MC), but also, significantly larger than the < 2 arcseconds of the SMA observations, used to map the CO outflows. The SMA obsrevations often reveal multiple substructures, that are all included in the same envelope, but are not all driving outflows. In such cases, the entire envelope mass is attributed to the single observed outflow source, even though it is likely, in the future, to break down into multiple sources, each driving a separate outflow.

A clear example of this is N53, where in the continuum emission of Fig. 16, two separate cores are clearly detected, but as the CO contours reveal, only one of them actually drives an outflow. Both these continuum peaks are part of the same extended envelope, and therefore the entire mass measured in Pitts et al. (in prep.) is attributed to the single outflow even though, the second core could potentially also give rise to a protostar, and therefore, an outflow. Similarly, for S8 and N48, where the SMA continuum emission reveals multiple substructures, far more extended than the source of the outflow, but included in the same envelope. Finally, as previously mentioned, the most characteristic case for which the envelope mass is overestimated, is N38. The origin of N38s outflow is located at a secondary continuum peak, to the North of the primary continuum peak. This structure remains unresolved in the observations used by Motte et al. (2007) to estimate the envelope mass of the source. It is therefore reasonable to assume that the envelope mass found in Motte et al. (2007) is mostly representative of the primary continuum peak, and not of the actual source the outflow source. In an attempt to use a more representative estimate of the actual envelope mass of the source behind the detected outflow we scaled down the mass found by Motte et al. (2007) by a factor of 4, and used this new value (see table 9) for this work. The scaling factor of 4 was determined by the ratio of the intensity of continuum emission of the primary and secondary peak. We recognise of course that this estimate is very uncertain, and that the actual envelope mass of N38 might vary significantly.

Additional uncertainties, that affect the accuracy of the envelope mass measurements, arise from the assumptions made for the calculation of the mass using dust continuum emission. In brief, as discussed in Kristensen et al. (2010), one has to assume that, the dust emission is optically thin, which is typically true for the long wavelengths where dust emission takes place, and that dust emission happens at a single temperature for the entire envelope. This assumption is less accurate, as for example, the presence of a protostar can heat the envelope from the inside. Therefore an average temperature is often assumed to describe the entire envelope, typically between 10 - 20 K. This assumption carries its own uncertainties as changes of 10 K are found to infer differences in the final mass estimate up to a factor of 3.

Overall, it is clear that the M_{env} used for the PILS Cygnus sources in this work are most likely over-estimated. We do not though expect such an over-estimate to be greater than, at most, an order of magnitude, with the possible exception of the most extreme case N38. Therefore, even though more accurate mass measurements are definitely required to better constrain the F_{CO} - M_{env} correlation, we do not expect the to significantly change our results regarding the effects of clustered star formation on outflow forces.

5.1.2 Uncertainties of the outflow forces

It is important to highlight also that, in contrast to M_{env}, the outflow force measurements for the PILS Cygnus sources, most likely represent lower limits of the true F_{CO}. This is a result of the velocity ranges used for the integration in Eq. 14, and more precisely of the lower limits for which the inner velocities of table 3 where used. As discussed in section 3, due to the optical thickness of the CO emission in combination with spatial filtering effects arising from the nature of interferometric observations, we are forced to exclude a velocity range of ≈ 10 up to ≈ 30 km s^{-1} surrounding the v_{source}. Therefore, the low velocity outflowing gas, that holds a significant part of the outflows mass, is not taken into account in measuring F_{CO} (Dunham et al. 2014). More precisely, Offner et al. (2011) found that, integrating over velocities > 2 km s^{-1} leads to an underestimate of the outflow mass by a factor of 5 - 10, a result that was also confirmed later by Dunham et al. (2014). Interestingly, N30, S26 and N63, the sources driving the strongest outflows, are also

Table 9: Envelope masses and bolometric luminosities of the Cygnus-X sources.

Source	$M_{\rm env}$ [$M_\odot$]	$L_{\rm bol}$ [$L_\odot$]	Ref.
N12	40	940	1
N30	260	28000	1
N38	60	-	2
N48	40	2100	1
N51	150	1500	1
N53	140	460	1
N54	40	-	2
N63	50	490	1
S8	70	7400	1
S26	350	244000	1

References. (1) Pitts et al. (in prep.), (2) Motte et al. (2007).

the sources with the largest masked-out velocity range. This is most likely due to, based on the $F_{\rm CO}$ - $M_{\rm env}$ correlation, these sources having larger envelopes and therefore being susceptible to spatial filtering effects at higher velocities, which in turn forces the inner velocities limits to higher velocities (in absolute for the blue-shifted ones).

We do not expect the difference in $F_{\rm CO}$ to be significant, but even if our measurement underestimates the true $F_{\rm CO}$ by as much as an order of magnitude, the results for the PILS Cygnus sources would still fall within the scatter of the high-mass sample from Maud et al. (2015b). Therefore, although the outflow measurements presented in table 6 are lower limits of the true $F_{\rm CO}$, our results regarding clustered star formation remain unchanged.

5.2 A comparison of high- and low-mass sources

Comparing now the two samples, of low- and high-mass sources, in Fig. 19 a clear distinction can be seen between them as there is a lack of measurements for sources with $M_{\rm env}$ of ≈ 10 $M_\odot$. At a first glance it could be argued that the low-mass sample follows a different correlation than the high-mass sample. Based on the good agreement between the best fit from van der Marel et al. (2013), found using solely low-mass sources, and the high-mass sample, we argue that, a more realistic explanation is that low- and high-mass sources are following the same $F_{\rm CO}$ - $M_{\rm env}$ correlation but low-mass sources exhibit significantly higher scatter. A possible explanation for the observed scatter could be that, material is not continuously accreted onto the central object, but rather in sudden bursts of high accretion rates followed by periods of low accretion rates, following a scenario known as episodic accretion (Audard et al. 2014). These accretion bursts are found to take place in timescales far shorter than those required for the dispersion of the protostellar envelope from both observations (i.e. Audard et al. (2014)), as well as computational models (i.e. Vorobyov & Basu (2015)). As we believe that outflow energetics are connected to $\dot{M}_{\rm acc}$ (Mottram et al. 2017; Duarte-Cabral et al. 2013), then we can also expect them to vary significantly on similar time-scales. This variation though would not be reflected to the surrounding envelope mass, thus giving rise to the observed scatter in the $F_{\rm CO}$ - $M_{\rm env}$ correlation. The fact that, a higher scatter is seen for low-mass protostars, compared to their high-mass counter parts, suggests that, episodic accretion is more prominent in low-mass protostars.

It is clear though that, more measurements, especially for intermediate mass protostars, are needed in order to properly connect the low- and high-mass samples and properly address these questions.
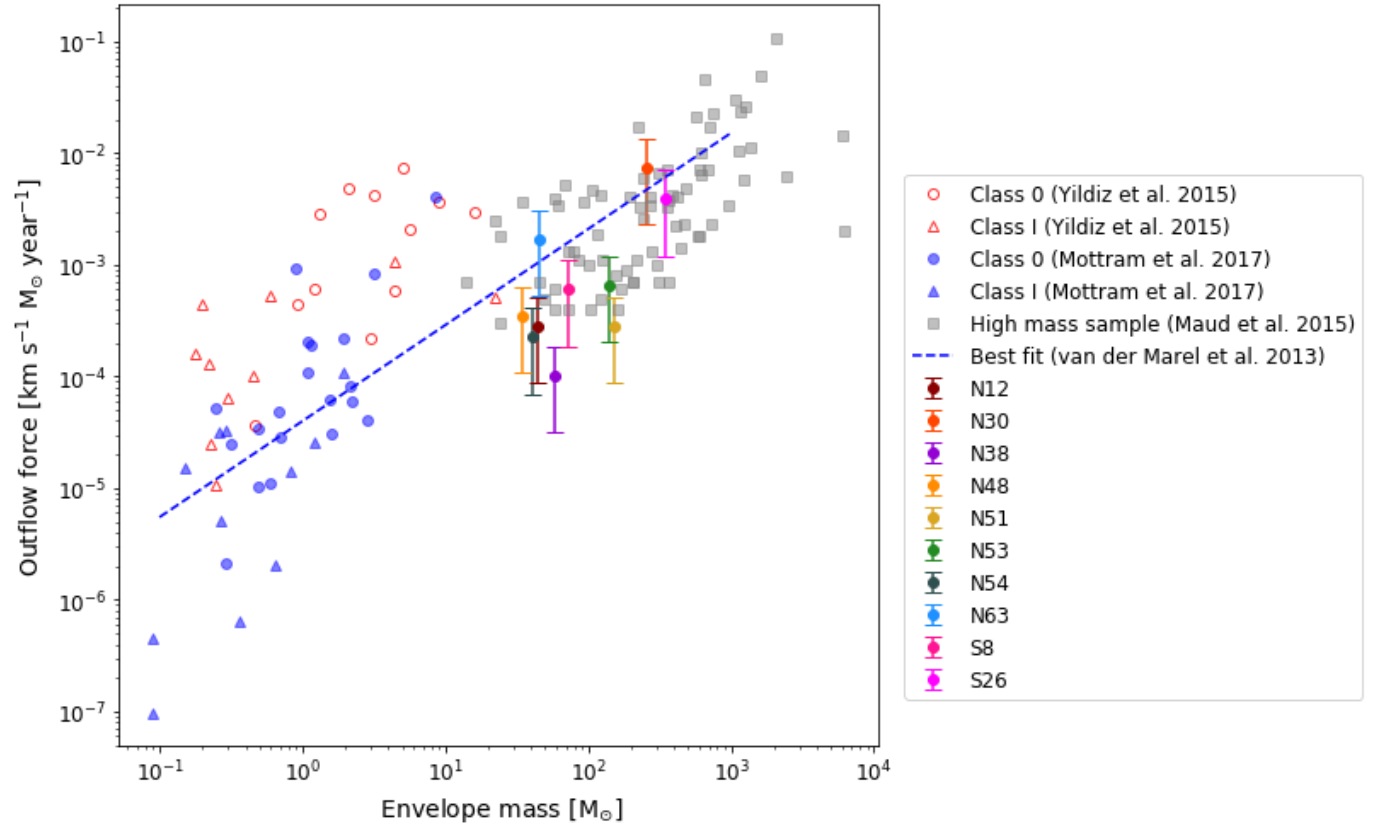
Figure 19: Outflow forces for the ten sources of the PILS Cygnus survey, over their envelope mass. Plotted in the same figure are, Class 0 sources from Yıldız et al. (2015) in empty red circles, Class I sources from Yıldız et al. (2015) in empty red triangles, Class 0 sources from Mottram et al. (2017) in filled blue circles, Class I sources from Mottram et al. (2017) in filled blue triangles and high mass sources from Maud et al. (2015b) in grey squares. The blue dashed line shows the best fit as found in van der Marel et al. (2013) for CO $[J = 3\text{-}2]$ observations of a low mass protostellar sample.

6 The Outflow Force - Bolometric Luminosity correlation

A correlation, connecting the outflow force and the bolometric luminosity of the source driving the outflow, has been separately detected for both protostellar sources (e.g. Cabrit & Bertout 1992; Bontemps et al. 1996) and extragalactic sources (e.g Lutz et al. 2020). Examining the F_{CO} - L_{bol} correlation, for both samples at the same time offers a unique opportunity, to connect the protostellar and extragalactic outflows to a common underlying launch mechanism, and thus open the way to the development of a unified model for outflow launch mechanisms.

Therefore, in order to examine the F_{CO} - L_{bol} correlation, we plot in Fig. 20 the outflow forces of the low- and high-mass protostellar sources over their bolometric luminosities. The low-mass sources from Yıldız et al. (2015) are plotted using the left-faced purple triangles, with the filled ones representing Class I sources and the empty ones Class 0. Similarly, right-faced magenta triangles are used for the low-mass sources from Mottram et al. (2017), with filled markers representing Class I sources and empty markers the Class 0 sources. The high mass sample from Maud et al. (2015b) is plotted using pink crosses and with the orange stars we mark the measurements for the Cygnus-X cloud from this work. The L_{bol} values used for the Cygnus-X sample, presented in table 9, are taken from Pitts et al. (in prep.) and were scaled for the distance of 1.3 kpc assumed in this work. As Pitts et al. (in prep.) has no measurements for N38 and N54, they are not included in Fig. 20. Similar to Fig. 19, the stars mark the mean F_{CO} measured for each source, for the available inclination angles, while the errorbars show the maximum and minimum values.

In addition, as discussed in Sec. 1.4, a similar correlation exists for the extragalactic sources (see Fig. 6). In order to examine if there is a connection between the protostellar and the extragalactic sources, we decided to also include in Fig. 20 measurements from extragalactic outflows. The extragalactic sample includes sources with both AGN and starburst (SB) powered outflows, plotted in blue and red markers respectively. The AGN sample is further divided into Seyfert I, Seyfert II and LINER sources. In brief, Seyfert galaxies are usually spirals with strong continuum and line emmission originating from their nucleus, while, in contrast, LINERs have very weak nuclear line emission. The additional classification, as Seyfert I and II, stems from the linewidth of the observed emission lines, with Seyfert I sources having broader emission lines which, in turn, translates to a higher outflow velocity. Seyfert I, Seyfert II and LINER sources in our sample are marked with squares, circles and triangles respectively. All points with filled markers are taken from Lutz et al. (2020), while empty markers represent sources from Fluetsch et al. (2019). The samples presented in Lutz et al. (2020) and Fluetsch et al. (2019) have a significant overlap, therefore in this work we used the entire sample from Lutz et al. (2020), as it is the most recent work, and added the unique measurements from Fluetsch et al. (2019). Both works made use of CO $[J = 1\text{-}0]$ observations, and use the approach of the time averaged thin shell, for calculating the outflow force. In this approach, a constant outflow rate, over the entire life-time of the outflow ($t_{\mathrm{flow}} = \dfrac{R_{\mathrm{out}}}{v_{\mathrm{out}}}$), is assumed, yielding a final density profile of $\rho \propto r^{-2}$. In this scenario the outflow rate is given as:

$$\dot{M}_{\mathrm{out}} = \frac{M_{\mathrm{out}} v_{\mathrm{out}}}{R_{\mathrm{out}}} \tag{20}$$

and then the outflow force is calculated as:

$$F_{\mathrm{CO}} = \dot{M}_{\mathrm{out}} v_{\mathrm{out}} \tag{21}$$

This approach is very similar to the v_{max} method (van der Marel et al. 2013) often used to calculate protostellar outflows, where a unique velocity is assumed for the entirety of the outflow.

A quick comparison of the outflow forces measured in the two works, for their shared sources, showed good agreement between the two (see Fig. 21). We therefore are confident that we can combine the results from the two studies into a single extragalactic sample for the purposes of this work. It is worth noting that, Fluetsch et al. (2019), apart from the molecular outflow forces measured via CO observations, contains also other type of outflow measurements for both molecular and ionized outflows. Examining those outflows fell outside the scope of this work, thus they were not included in the extragalactic sample.
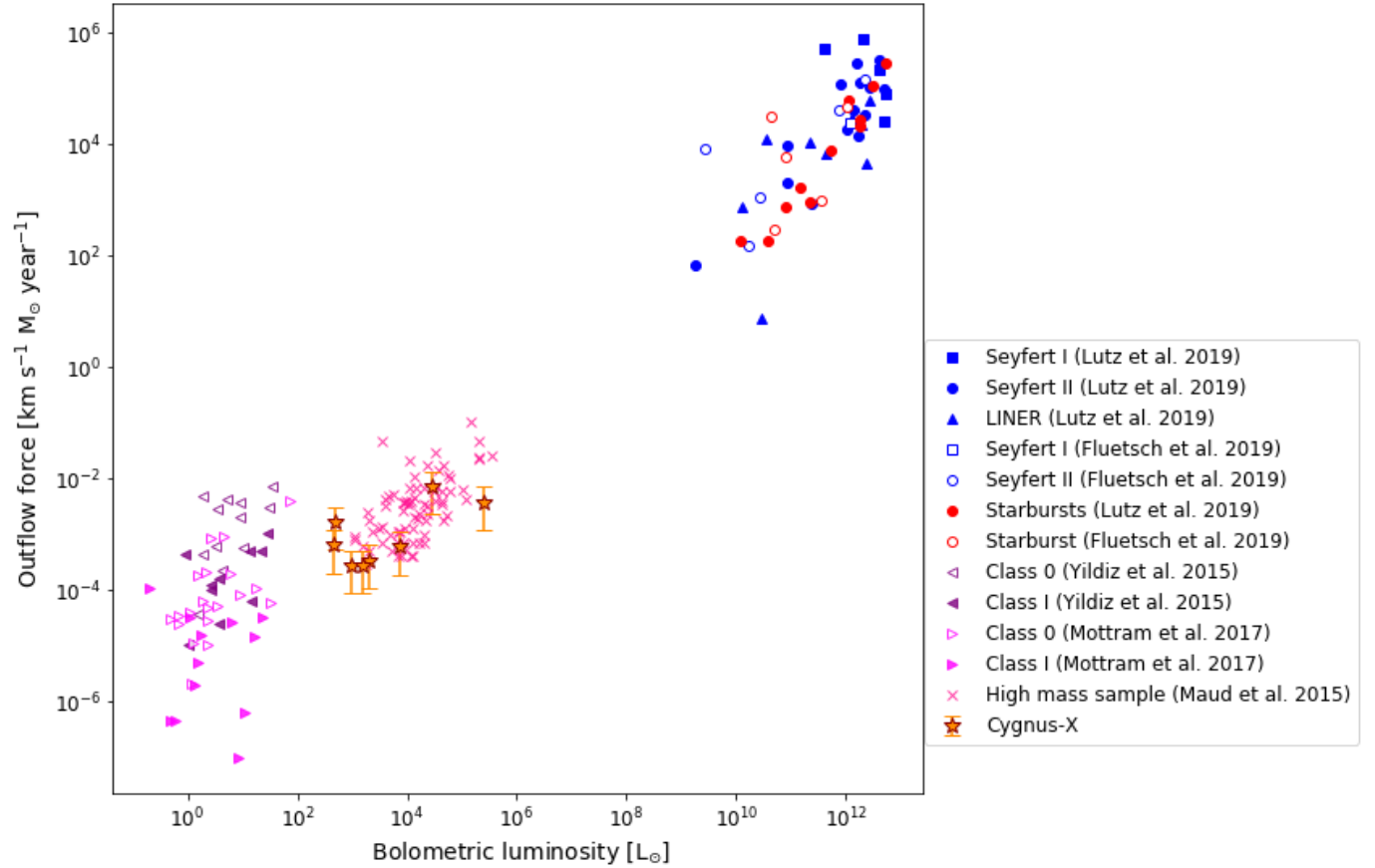
Figure 20: Outflow forces over bolometric luminosities for a sample of low-mass protostars, a sample of high-mass protostars and extragalactic sources. Left looking, purple triangles represent the sources from Yıldız et al. (2015), with the empty ones corresponding to Class 0 and filled ones to Class I. Right facing, magenta triangles represent sources from Mottram et al. (2017), again with empty triangles marking Class 0 and filled ones Class I sources. Pink crosses represent the high-mass sample from Maud et al. (2015b) and the orange stars the the mean value, calculated for the different inclination angles, for the Cygnus-X sample, with the errorbars marking the maximum and minimum measured F_{CO}. For the extragalactic sample, AGN sources are marked in blue, with squares for Seyfert I, circles for Seyfert II and triangles for LINER sources. Red circles mark the starburst sources. Finally, filled points represent measurements taken from Lutz et al. (2020) and empty ones from Fluetsch et al. (2019).
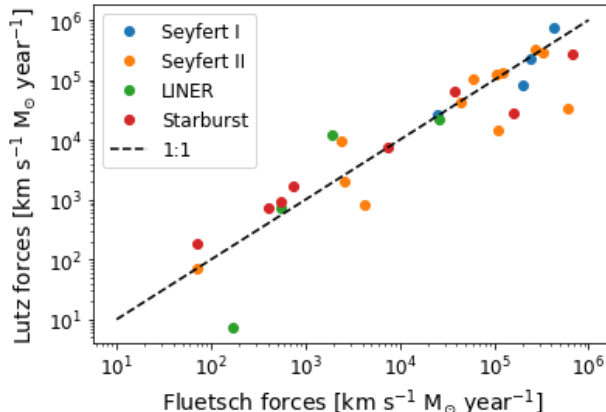
Figure 21: A comparison of outflow force measurements between Lutz et al. (2020) and Fluetsch et al. (2019) for the shared sources in their samples. Plotted in black dashed line is the 1:1 ratio.

6.1 Protostellar sources

Focusing on the protostellar part of the sample, we again see a clear separation between the low- and high-mass sample, similar to what was discussed in Sec. 5.2, albeit this time the separation appears even clearer. Again we favor the scenario that low- and high-mass protostars follow the same correlation with the low mass sources having significant larger scatter due to episodic accretion causing significant variation to their outflow behaviour. Such a scenario is also able to explain why the separation between low- and high-mass sources is more prominent in the F_{CO} - L_{bol} correlation, compared to the F_{CO} - M_{env}, as the first is believed to better trace the current outflow behaviour, which is more affected from episodic accretion events (Mottram et al. 2017). This happens as, L_{bol} is directly connected to the gravitational energy released by the accreting material, therefore each change on the accretion rate translates, in theory, directly to a change in L_{bol}. In contrast, M_{env} changes according to the evolutionary stage of the protostar, slowly dissipating as the protostar evolves. As a result, the sudden changes in accretion, expected in the case of episodic accretion, should be traced in L_{bol}, but not in M_{env}.

Similar to the F_{CO} - M_{env} correlation case, the much tighter F_{CO} - L_{bol} correlation observed for the high-mass sample suggests that episodic accretion is less pronounced in high-mass sources.

In this instance, we again see a good agreement between the Cygnus-X sources and the high-mass sample from Maud et al. (2015b) that further strengthens the previous suggestion (see Sec. 5.1) that clustered star formation has no significant impact on protostellar outflow activity.

Finally, the protostellar F_{CO} - L_{bol} correlation, once more highlights the need for additional observations, especially in the area of $L_{bol} \approx 10^2$ $L_{\odot}$, in order to properly connect the low- and high-mass samples. Properly connecting the two samples will assist significantly in determining if the two samples are indeed following the same correlation or not. Finding that low- and high-mass star formation would, in turn, strongly favor the scenario that high-mass star formation is simply a scaled up version of its low-mass counterpart. In addition, observation of intermediate-mass sources will, most likely, offer a better understanding of episodic accretion and how its effects change depending on the size of the accreting source.

6.2 Extragalactic sources

Regarding the extragalactic sample, at a first glance, we note that there appears to be no clear distinction between AGN- and starburst-powered outflows, apart from the AGN sample displaying higher dispersion. Among the different types of AGN powered outflows, Seyfert I galaxies appear to drive slightly stronger outflows, consistent with the higher velocities detected in their case, while there is no clear distinction between the outflows of the other two types. We note though that the individual sub-samples are small and thus we cannot draw any significant conclusions at this point. We therefore treat all the AGN-powered outflows as a single sample for this work.

6.3 A statistical comparison of best-fits

The most interesting question arising from the F_{CO} - L_{bol} correlation in Fig. 20, is if, and how well, do the low-mass, high-mass and extragalactic samples compare to each other and if it is at all possible to assume a common correlation for all three samples. In order to do so, we calculated the best-fit of the F_{CO} - L_{bol} correlation for each of the samples. In addition to these, we also examined the AGN and SB driven outflows separately, as well as the Class 0 and Class I sources. Using the least squares method to find the best-fits, we get:

- Extragalactic sources: $\log(F_{CO}) = (0.93 \pm 0.11)\log(L_{bol}) - (6.7 \pm 1.3)$

- AGN sources: $\log(F_{CO}) = (0.86 \pm 0.14)\log(L_{bol}) - (5.9 \pm 1.6)$

- SB sources: $\log(F_{CO}) = (1.08 \pm 0.20)\log(L_{bol}) - (8.6 \pm 2.3)$

- High-mass sources: $\log(F_{CO}) = (0.60 \pm 0.08)\log(L_{bol}) - (5.0 \pm 0.3)$

- Low-mass sources: $\log(F_{CO}) = (0.80 \pm 0.25)\log(L_{bol}) - (4.5 \pm 0.2)$

- Class I sources: $\log(F_{CO}) = (0.47 \pm 0.39)\log(L_{bol}) - (4.9 \pm 0.3)$

- Class 0 sources: $\log(F_{CO}) = (1.02 \pm 0.26)\log(L_{bol}) - (4.3 \pm 0.2)$
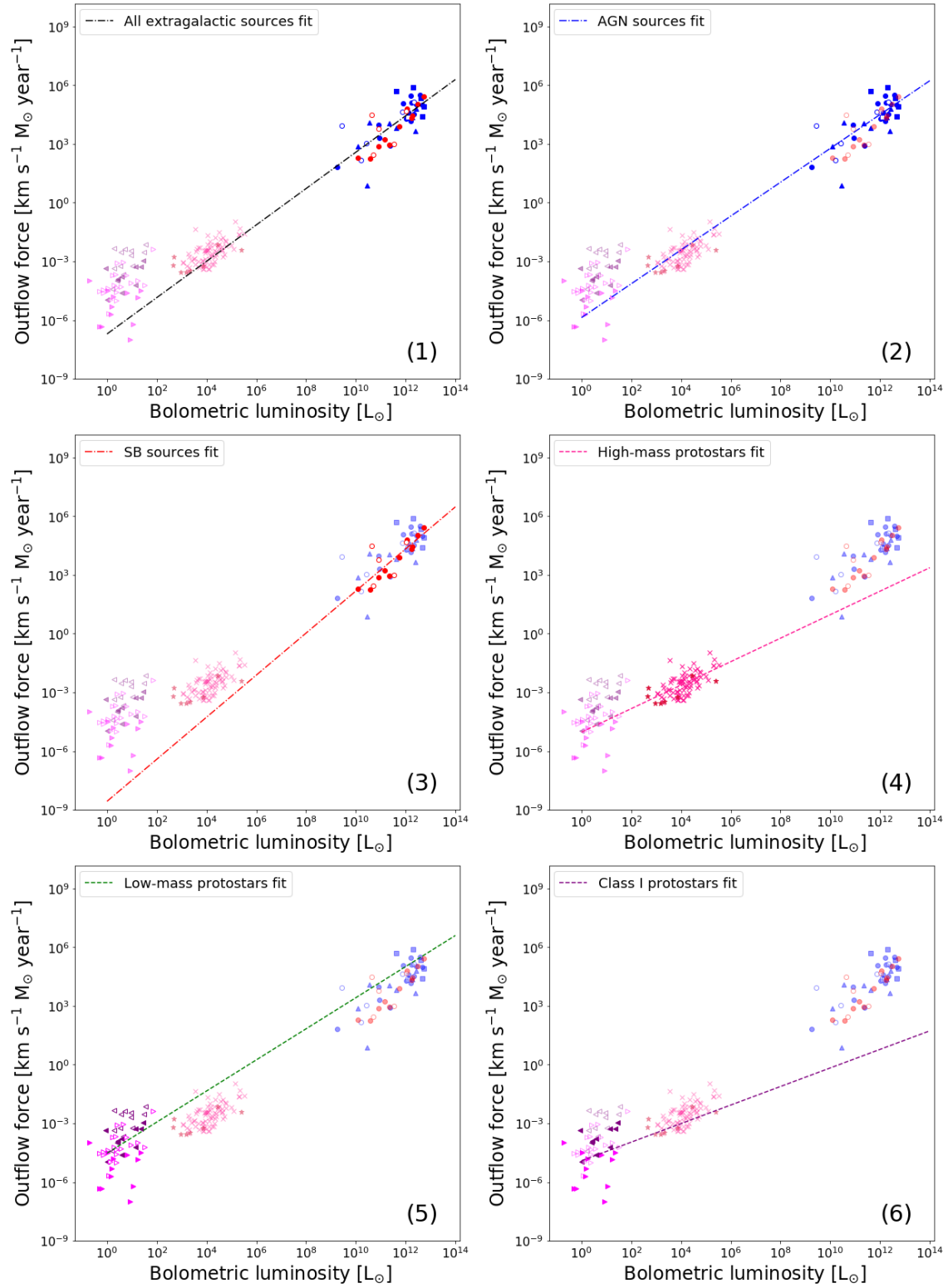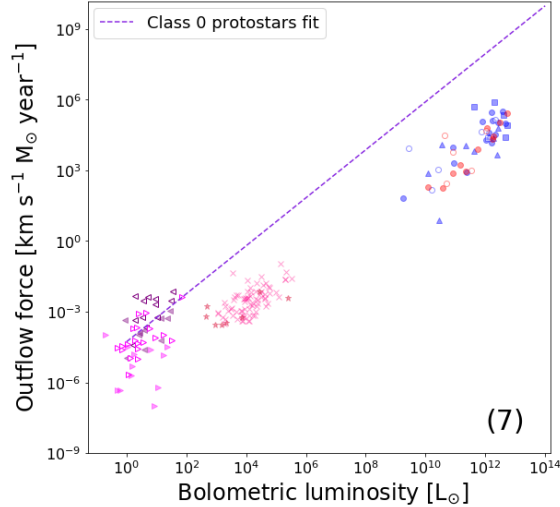
Figure 22: Outflow forces over bolometric luminosities for a sample of low-mass protostars, a sample of high-mass protostars and extragalactic sources. In each plot, the the sample, from which the plotted best-fit of the F_{CO} - L_{bol} was taken, is highlighted. (1) Best-fit to all extragalactic sources. (2) Best-fit to AGN extragalactic sources. (3) Best-fit to starburst extragalactic sources. (4) Best-fit to high-mass protostellar sources. (5) Best-fit to all low-mass protostellar sources. (6) Best-fit to Class I low-mass protostellar sources. (7) Best-fit to Class 0 low-mass protostellar sources.

For clarity, we plot the best-fit we found, extrapolated over the entire luminosity range of our samples, in Fig. 22 highlighting in each sub-figure the sample that was used for the plotted fit. Each plot is numbered for ease of reading, with (1) being the best fit for all extragalactic sources, (2) for AGN sources, (3) for SB sources, (4) for high-mass protostellar sources, (5) for all low-mass protostellar sources, (6) for Class I low-mass protostars and (7) for Class 0 low-mass protostars.

To properly compare the various fits, and determine any similarities between the correlation followed for the different sources, we opted for a statistical comparison of the fits. As a first step, we performed an F-test on the variances of the samples, comparing them in pairs. Briefly, to perform an F-test, we need to calculate the F-value, which is given as:

$$F = \frac{s_1}{s_2} \tag{22}$$

where s_1 and s_2 are the variances to be compared, with $s_1 > s_2$. The F-value is then compared with a critical value (F_{crit}), calculated from the F-table[2], and which depends on the degrees of freedom (DF) of both samples. These are calculated as $N - 1$ for each sample, with N being the number of sources in the sample. If the F-value calculated is smaller than the F_{crit}, then the two variances are similar enough and we can compare the two samples. In this work we use the F-table for $\alpha = 0.05$, which corresponds to a 95% confidence level.

For the pairs with comparable variances, we then performed two-tailed t-tests, in order to examine if the parameters of their best-fit, the slope and the intersection, could be considered equal or not. For a t-test, we make the initial assumption that the parameters are equal (H_0: $b_1 = b_2$) and we calculate the t-value as:

$$t = \frac{b_1 - b_2}{\sqrt{s_{b_1} + s_{b_2}}} \tag{23}$$

where b_1 and b_2 the compared parameter of the two fits, and s_{b_1} and s_{b_2} the corresponding variance of the parameters. The t-value is then used, alongside the degrees of freedom, which is in this case defined as $N_1 + N_2 - 4$ with N_1 and N_2 the sizes of the two samples whose fits we are comparing, in order to calculate the P value [3]. If the resulting P-value is lower than the confidence level α, then the initial hypothesis can be rejected and the compared parameters are not equal. On the other hand, if the P-value exceeds a then

---

[2]http://www.socr.ucla.edu/Applets.dir/F_Table.html
[3]For this step an online calculator was used (https://www.socscistatistics.com/pvalues/tdistribution.aspx)

the initial hypothesis cannot be rejected and we assume that the two parameters are equal. The confidence level selected for this work is $\alpha = 0.05$, resulting to a 95% level of confidence in our results.

We present in table 10 the F-values calculated for all comparisons among the seven samples, as well as the degrees of freedom corresponding to each sample. Comparing these values with the appropriate critical values from the F-table, we determined that:

- The variance for the three extragalactic samples (entire sample, AGN and SB) are comparable with one another.

- The high-mass protostellar sample variance is only comparable with the SB sample.

- The low-mass sample variance is comparable with the Class I sample, but not the Class 0.

- The Class 0 sample is comparable with all three extragalactic samples.

Table 10: F-values for the best-fit variances comparisons and the degrees of freedom for each sample.

	Class 0	Class I	Low-mass	High-mass	Starburst	AGN	DF
Extragalactic	1.11	2.18	2.01	2.52	1.51	1.09	49
AGN	1.01	1.99	1.84	2.76	1.66	-	33
Starburst	1.67	3.29	3.04	1.67	-	-	15
High-mass	2.79	5.49	5.06	-	-	-	82
Low-mass	1.82	1.08	-	-	-	-	53
Class I	1.97	-	-	-	-	-	21
Class 0	-	-	-	-	-	-	31

Notes. (1) Mirrored comparisons are equivalent and therefore not shown.
(2) DF $= N - 1$ for the F-test

Table 11: p-values and DF for comparison of the intersection and slope of samples with matching variances.

	p_{slope}	p_{inter}	DF
Extragalactic - AGN	0.72	0.69	80
Extragalactic - SB	0.53	0.49	62
AGN - Starburst	0.40	0.35	46
Extragalactic - Class 0	0.75	0.07	78
AGN - Class 0	0.61	0.33	62
Starburst - Class 0	0.87	0.07	44
Starburst - High-mass	0.03	0.14	95
Low-mass - Class I	0.49	0.31	72

Notes. DF $= N_1 + N_2 - 4$ for the two-tailed t-test

We performed t-test for the best-fits of the sample pairs found having comparable variances and present the resulting p-values along with the corresponding DF in table 11. The p_{slope} value corresponds to the comparison of the slopes of the fits, while p_{inter} to the comparison of the intersections. In the end, we find that:

- The best-fits for the three extragalactic samples (AGN, SB and the entire sample) can be considered equal.

- The slope of the high-mass sample best-fit does not match the slope of the SB sample fit. They, therefore, do not follow the same correlation.

- The best-fit to the entire low-mass protostellar sample is equivalent to the best-fit of the Class I sources.

- The best-fit to Class 0 low-mass protostars can be considered equal to the best-fits of all extragalactic samples.

The most interesting result, is that, with 95% confidence, low-mass Class 0 protostars appear to follow the same F_{CO} - L_{bol} correlation as the extragalactic sources. For Starburst powered extragalactic outflows, this result supports a scenario where these outflows are, from among the various powering sources suggested in Veilleux et al. (2020), predominantly driven by a large number of protostellar outflows. In the case of AGN powered extragalactic outflows, the presence of a common correlation with the low-mass class 0 protostellar sample strongly favors the launching mechanism suggested in Aalto et al. (2020), and that greatly resembles the launching mechanisms of the protostellar outflows. As we now found that the fit parameters of the Class 0 and extragalactic fits can be considered similar, the significant difference between them, seen in Fig. 22, is mostly attributed to the uncertainty of the extrapolation of a fit over many orders of magnitude.

The discrepancy between low-mass Class 0 and Class I sources agrees with results from Bontemps et al. (1996), who also found, albeit for a smaller sample, that Class 0 sources do not agree well with the F_{CO} - L_{bol} correlation for Class I sources. A possible explanation for this discrepancy, as well as for discrepancy between the high-mass protostellar sample and the low-mass Class 0 sample, will be discussed in more detail in Sec. 6.4.

6.3.1 Alternative force calculation method for extragalactic sources

Apart from the assumption of the time-averaged thin shell, used from Lutz et al. (2020); Fluetsch et al. (2019) another commonly used method for calculating the outflow force of extragalactic sources, is to assume that, the outflowing gas fills the entire cavity of the outflow with a constant density (e.g Cicone et al. 2014; Fiore et al. 2017). This alternate calculation method is found to differ by a factor of three compared to the thin shell approach (Lutz et al. 2020). To test if the selected method of outflow force calculation has any impact on our results, we increased the outflow forces of our extragalactic sample by a factor of three, and performed again the statistical analysis for the new best-fits. The resulting differences in F- and p-values, we found, were minimal, and did not significantly change any of our previous results. Therefore, at this point, there is no apparent preference towards either of the methods used for calculating outflow forces, and the conclusion appear to stand for both scenarios.

6.4 The ionized outflow mass

In an attempt to explain the observed discrepancies between the F_{CO} - L_{bol} correlation set by the low-mass class 0 protostellar sources, and the correlations derived from the other samples, we suggest the possibility of a significant ionized component in the outflows. Since Class 0 sources are deeply embedded, all ionizing radiation from the protostar is quickly absorbed by the surrounding envelope. Therefore, for Class 0 sources, we assume that the ionized component would be negligible, and that the energetics of the outflow are clearly dominated by the molecular component. This is not the case for the other types of sources we examine.

For example, as the envelope disperses in Class I sources, more of the protostellar radiation escapes, dissociating and ionizing the molecular outflow (Panoglou et al. 2012). As a result, a decrease in the molecular fraction of the outflow, when compared to Class 0 sources, is expected (Bally 2016).

On the other hand, high-mass protostars emit most of their radiation at short wavelengths, capable of ionizing the surrounding gas. It is expected therefore that their outflows would contain a significant fraction of ionized gas. Indeed, Gusdorf et al. (2015) and Leurini et al. (2015) found for the outflow of the massive star-forming region G5.89-0.39, a ratio between ionized and molecular column densities of $\frac{N_{C_{II}}}{N_{CO}} \approx 100$.

For the extragalactic sources, based on the comparison between the dynamics of molecular and ionized outflows, as measured from Fiore et al. (2017), we do not expect a dominant ionized component. In addition to that, our previous results show that the correlation of Class 0 low-mass protostars is equivalent to the one followed by the extragalactic sources strengthening the previous assumption.

To properly examine our assumption, and give measurable values for the expected ionized component in the outflows, we calculated the total outflow force (F_{tot}) needed for all sources to match the Class 0 correlation, where we assume that $F_{tot} = F_{ion} + F_{mol}$. We can then calculate the ratio of outflow forces for the ionized (F_{ion}) and molecular (F_{mol}) components. Adopting a simplistic outflow force calculation method $F = \frac{M_{out} v_{out}}{t_{dyn}}$, we then assume that both outflows have the same outflow velocities v_{out} and dynamical time t_{dyn}. Such an assumption is supported by CO, O_I and C_{II} observations from Leurini et al. (2015); Gusdorf

et al. (2015). Under these assumptions, the ionized to molecular gas mass ratio is equal to the outflow force ratio $\left(\dfrac{M_{\mathrm{ion}}}{M_{\mathrm{mol}}} = \dfrac{F_{\mathrm{ion}}}{F_{\mathrm{mol}}}\right)$. Finally, we assume that the fraction of $\mathrm{C_{II}}$ in the ionized gas is the same as the fraction of CO in the molecular outflow, therefore $\dfrac{M_{\mathrm{ion}}}{M_{\mathrm{mol}}} = \dfrac{M_{\mathrm{C_{II}}}}{M_{\mathrm{CO}}}$.

We present the resulting mass ratios, for low-mass Class I, high-mass and extragalactic sources plotted over the corresponding L_{bol} in Fig. 23 (top, middle and bottom respectively). The corresponding best-fits, also plotted in dashed lines, are :

- $\log(\dfrac{M_{\mathrm{C_{II}}}}{M_{\mathrm{CO}}}) = (0.04 \pm 0.50)\log(L_{\mathrm{bol}}) + (0.9 \pm 0.4)$, for Class I sources.

- $\log(\dfrac{M_{\mathrm{C_{II}}}}{M_{\mathrm{CO}}}) = (0.42 \pm 0.08)\log(L_{\mathrm{bol}}) + (0.7 \pm 0.3)$, for high-mass sources.

- $\log(\dfrac{M_{\mathrm{C_{II}}}}{M_{\mathrm{CO}}}) = (0.09 \pm 0.11)\log(L_{\mathrm{bol}}) + (2.4 \pm 1.3)$, for extragalactic sources.

Finally, alongside the high-mass protostellar sources, we also plot the estimate for G5.89-0.39, assuming that the masses scale with the column densities meaning that $\dfrac{M_{\mathrm{C_{II}}}}{M_{\mathrm{CO}}} = \dfrac{N_{\mathrm{C_{II}}}}{N_{\mathrm{CO}}}$ and using the L_{bol} measurement from Hunter et al. (2000).

Our results for Class I sources appear to be constant over L_{bol}. At the same time, they display a rather significant scatter, mostly ranging from 10^{-1} to 10^{2}. These results suggest, albeit with significant uncertainty, that the presence of an ionized outflow is not always necessary in order for Class I sources to follow the Class 0 correlation. In addition these results would be consistent with the dispersion of the envelope as the reason behind the appearance of the ionized component, as newly emerging class I protostars would have denser envelopes than more evolved class I protostars and therefore would have lower ionized-to-molecular mass ratios.

For the high-mass protostars, our results reveal a clear trend, with the ionized-to-molecular mass ratio increasing with L_{bol}. Such a correlation can be explained, as the more luminous stars emit more ionizing radiation, leading to a larger fraction of ionized gas in their surroundings. Notably, the measured ratio for G5.89-0.39 falls on the lower end of our measurements, but well within the observed scatter, therefore suggesting that, the ionized-to-molecular mass ratios needed, in order for high-mass protostars to follow the correlation set by low-mass Class 0 sources, are realistic. This then implies that, high-mass protostars are indeed following the same F_{CO} - L_{bol} correlation as the Class 0 and the extragalactic sources, firther strengthening the connection between the different types of outflows.

Finally, for the extragalactic sources, once more the ratio appears to be almost constant over the luminosities. although we find a significant ionized-to-molecular mass ratio of $\approx 10^{3}$. This result is in contrast to what we previously expected as the extragalactic outflow are shown to follow the same correlation as the low-mass Class 0 protostars. We attribute this discrepancy to the uncertainties that arise from extrapolating the best-fit of the low-mass Class 0 sample over more than 10 orders of magnitude.

Overall, our results for the ionized-to-molecular mass ratio, appear to offer a realistic explanation to the observed differences between the high-mass protostars and the Class 0 protostars. At the same time, results for Class I sources are more unclear, while results for extragalactic sources cannot be trusted due to the uncertainties of the extrapolated Class 0 best-fit.
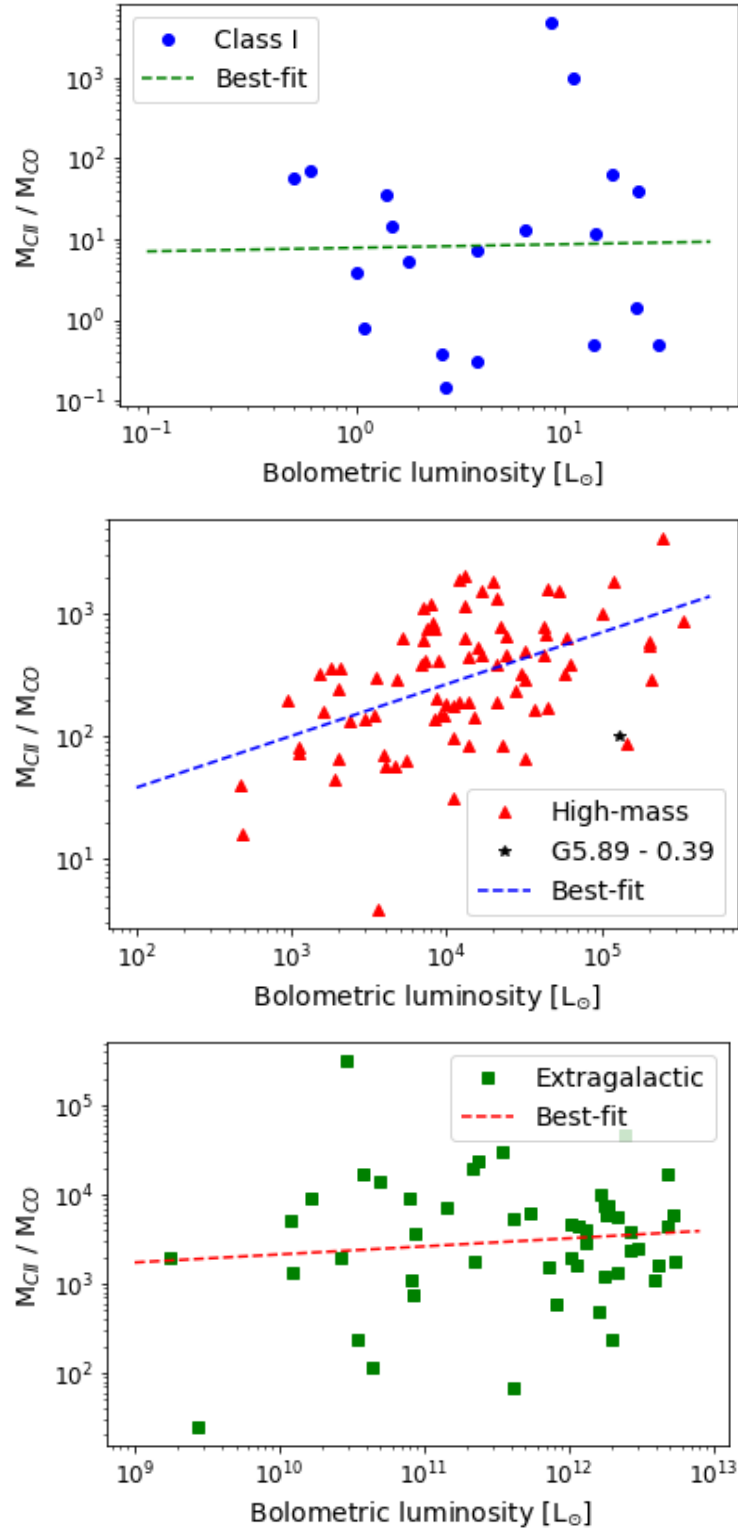
Figure 23: Ionized to molecular gas mass ratio plotted over the bolometric luminosities for Class I low-mass protostellar sources (top), High-mass protostellar sources (middle) and Extragalactic sources (bottom).Also plotted, in dashed lines, are the corresponding best fits in each case. Alongside the high-mass sample we plot the observed value for G5.89-0.39. (Gusdorf et al. 2015; Leurini et al. 2015).

7 Summary and Conclusions

In summary, for this work we looked at interferometric observations of CO [$J = 3$-2] and SiO [$J = 8$-7] emission lines of ten high-mass protostellar sources in the Cygnus-X molecular cloud. The observations form part of the PILS Cygnus survey and were carried out with the SubMillimeter Array. All data was initially cleaned using CASA v4.7 and then used to detect molecular outflows and measure the corresponding outflow forces. In addition, an extended sample of low-mass protostellar, high-mass protostellar and extragalactic outflows, with outflow force measurements, was gathered from the literature. Using this sample, we examined both, the effects of clustered star formation, by comparing our results, for the Cygnus-X sources, with similar results from the literature, as well as, the existence of common scaling relations between protostellar and extragalactic outflows. The main conclusions, arising from this work, are as follows:

- Using integrated intensity maps of the CO [$J = 3$-2] line emission, molecular outflows were detected originating from all ten sources of the PILS Cygnus survey, and their respective outflow forces were successfully measured.

- The close agreement found between the F_{CO}, measured for the ten Cygnus-X sources, with results from the literature, for sources with similar M_{env} and L_{bol}, indicate that, clustered star formation has no significant effect on the outflow behaviour of protostars. As the outflow activity is tied to the accretion process, this result suggests that, protostellar accretion is not significantly affected by the surrounding environment, but it is rather tied to local processes, determined by the protostar itself.

- Examination of the F_{CO} - M_{env} and F_{CO} - L_{bol} correlations, for the protostellar sources, revealed clear differences between the low- and high-mass protostellar sources both in the correlation itself as in the observed scatter. The observed scatter could potentially be explained as a result of episodic accretion, which would then suggest that, episodic accretion is more prominent in low-mass protostars than in their high-mass counterparts.

- The statistical comparison of the best-fits to the F_{CO} - L_{bol} correlation, for the different types of sources in the literature sample, revealed, with 95% confidence, that extragalactic and low-mass Class 0 protostellar outflows follow the same correlation, thus suggesting the presence of a common underlying launch mechanism.

- The presence of a significant ionized outflow in the case of high-mass protostellar sources offers a realistic explanation for the observed discrepancies between the F_{CO} - L_{bol} correlation of low-mass Class 0 and high-mass protostars.

Although our results allow for some interesting conclusions to be drawn, they also highlight the need for additional research and observations on the matter. More specifically, additional and more accurate observations are certainly required in order to constrain the observed F_{CO} - M_{env} correlation. This is even more apparent for the case of intermediate-mass sources, required to properly connect the low- and high-mass protostellar samples. This would, in turn, offer significant insight into the behaviour of episodic accretion, and more specifically to when, and why, it goes from having a significant effect in low-mass sources to having little to no effect in high-mass sources.

Similarly, more observations of ionized outflows, especially for high-mass protostars are required in order to examine the assumption that they indeed follow the same F_{CO} - L_{bol} correlation as the low-mass Class 0 sources. In addition, the connection between low-mass Class 0 protostars and extragalactic sources needs to be examined further and in more detail as well. Verifying that both high-mass protostars and extragalactic sources follow the same outflow correlation would strongly support the existence of a common launching mechanism, for both types of outflows, and would, in turn, open the way for the development of a universal outflow launch model.

Overall, we were able using statistical comparison of best-fits, to find, with 95% confidence, evidence that extragalactic outflows follow the same correlation with Class 0 protostars. In addition, we find that, a realistic ionized outflow is required in order for high-mass outflows to also follow the same correlation. We thus find that, it is likely, for protostellar and extragalactic outflows, to follow the same correlation, which then implies the existence of a common launching mechanism, behind both types of outflows, and

that extragalactic outflows are in truth a significantly scaled-up version of protostellar outflows. Of course though, more work is required to confirm this suggestion.

References

Aalto, S., Falstad, N., Muller, S., et al. 2020, Astronomy & Astrophysics, 640, A104

André, P. 1993, in 28th Rencontres de Moriond: Astrophysics: The Cold Universe

Andre, P., Ward-Thompson, D., & Barsony, M. 1993, The Astrophysical Journal, 406, 122

Audard, M., Abrahám, P., Dunham, M. M., et al. 2014, Protostars and Planets VI, 387

Bally, J. 2016, Annual Review of Astronomy and Astrophysics, 54, 491

Beuther, H., Schilke, P., Sridharan, T., et al. 2002, Astronomy & Astrophysics, 383, 892

Bontemps, S., André, P., Terebey, S., & Cabrit, S. 1996, in Disks and Outflows Around Young Stars (Springer), 270–275

Cabrit, S. & Bertout, C. 1990, The Astrophysical Journal, 348, 530

Cabrit, S. & Bertout, C. 1992, Astronomy and Astrophysics, 261, 274

Cicone, C., Maiolino, R., Sturm, E., et al. 2014, Astronomy & Astrophysics, 562, A21

Curtis, E. I., Richer, J. S., Swift, J. J., & Williams, J. P. 2010, Monthly Notices of the Royal Astronomical Society, 408, 1516

Cyganowski, C., Reid, M. J., Fish, V., & Ho, P. 2003, The Astrophysical Journal, 596, 344

Downes, T. P. & Cabrit, S. 2007, Astronomy & Astrophysics, 471, 873

Duarte-Cabral, A., Bontemps, S., Motte, F., et al. 2013, Astronomy & Astrophysics, 558, A125

Dunham, M. M., Arce, H. G., Mardones, D., et al. 2014, The Astrophysical Journal, 783, 29

Fiore, F., Feruglio, C., Shankar, F., et al. 2017, Astronomy & Astrophysics, 601, A143

Fluetsch, A., Maiolino, R., Carniani, S., et al. 2019, Monthly Notices of the Royal Astronomical Society, 483, 4586

Frerking, M., Langer, W., & Wilson, R. 1982, The Astrophysical Journal, 262, 590

Fukui, Y., Iwata, T., Mizuno, A., Bally, J., & Lane, A. P. 1993, in Protostars and Planets III, ed. E. H. Levy & J. I. Lunine, 603

González-Alfonso, E., Fischer, J., Spoon, H., et al. 2017, The Astrophysical Journal, 836, 11

Gusdorf, A., Marcowith, A., Gerin, M., & Güsten, R. 2015, arXiv preprint arXiv:1503.06580

Hunter, T., Churchwell, E., Watson, C., et al. 2000, The Astronomical Journal, 119, 2711

Kauffmann, J., Bertoldi, F., Bourke, T. L., Evans, N. J., & Lee, C. W. 2008, Astronomy & Astrophysics, 487, 993

Knodlseder, J. 2000, arXiv preprint astro-ph/0007442

Kristensen, L., Van Dishoeck, E., van Kempen, T., et al. 2010, Astronomy & Astrophysics, 516, A57

Lada, C. J. 1987, in Symposium-International astronomical union, Vol. 115, Cambridge University Press, 1–18

Lee, C.-F., Ho, P. T. P., Li, Z.-Y., et al. 2017, Nature Astronomy, 1, 0152

Leung, H. O. & Thaddeus, P. 1992, The Astrophysical Journal Supplement Series, 81, 267

Leurini, S., Wyrowski, F., Wiesemeyer, H., et al. 2015, Astronomy & Astrophysics, 584, A70

Lumsden, S., Hoare, M., Oudmaijer, R., & Richards, D. 2002, Monthly Notices of the Royal Astronomical Society, 336, 621

Lumsden, S., Hoare, M., Urquhart, J., et al. 2013, The Astrophysical Journal Supplement Series, 208, 11

Lutz, D., Sturm, E., Janssen, A., et al. 2020, Astronomy & Astrophysics, 633, A134

Maud, L., Lumsden, S., Moore, T., et al. 2015a, Monthly Notices of the Royal Astronomical Society, 452, 637

Maud, L. T., Moore, T., Lumsden, S., et al. 2015b, Monthly Notices of the Royal Astronomical Society, 453, 645

McMullin, J. P., Waters, B., Schiebel, D., Young, W., & Golap, K. 2007, in Astronomical Society of the Pacific Conference Series, Vol. 376, Astronomical Data Analysis Software and Systems XVI, ed. R. A. Shaw, F. Hill, & D. J. Bell, 127

Motte, F., Bontemps, S., Schilke, P., et al. 2007, Astronomy & Astrophysics, 476, 1243

Mottram, J., Van Dishoeck, E., Kristensen, L., et al. 2017, Astronomy & Astrophysics, 600, A99

Offner, S. S., Lee, E. J., Goodman, A. A., & Arce, H. 2011, The Astrophysical Journal, 743, 91

Panoglou, D., Cabrit, S., Des Forêts, G. P., et al. 2012, Astronomy & Astrophysics, 538, A2

Piddington, J. & Minnett, H. 1952, Australian Journal of Chemistry, 5, 17

Pudritz, R. E. & Norman, C. A. 1986, The Astrophysical Journal, 301, 571

Richard Thompson, A., Moran, J. M., & Swenson Jr, G. W. 2017, Interferometry and synthesis in radio astronomy (Springer Nature)

Rygl, K., Brunthaler, A., Sanna, A., et al. 2012, Astronomy & Astrophysics, 539, A79

Shu, F., Najita, J., Ostriker, E., et al. 1994, The Astrophysical Journal, 429, 781

Spilker, J. S., Aravena, M., Phadke, K. A., et al. 2020, The Astrophysical Journal, 905, 86

Stahler, S. W. & Palla, F. 2008, The formation of stars (John Wiley & Sons)

Strom, K. M., Strom, S. E., Edwards, S., Cabrit, S., & Skrutskie, M. F. 1989, The Astronomical Journal, 97, 1451

Sturm, E., González-Alfonso, E., Veilleux, S., et al. 2011, The Astrophysical Journal Letters, 733, L16

Tabone, B., Cabrit, S., Bianchi, E., et al. 2017, Astronomy & Astrophysics, 607, L6

Terebey, S., Shu, F. H., & Cassen, P. 1984, The Astrophysical Journal, 286, 529

van der Marel, N., Kristensen, L. E., Visser, R., et al. 2013, Astronomy & Astrophysics, 556, A76

van Kempen, T., van Dishoeck, E., Güsten, R., et al. 2009, Astronomy & Astrophysics, 507, 1425

Veilleux, S., Maiolino, R., Bolatto, A. D., & Aalto, S. 2020, The Astronomy and Astrophysics Review, 28, 1

Vorobyov, E. I. & Basu, S. 2015, The Astrophysical Journal, 805, 115

Wright, N. J., Drake, J. J., Drew, J. E., & Vink, J. S. 2010, The Astrophysical Journal, 713, 871

Wu, Y., Wei, Y., Zhao, M., et al. 2004, Astronomy & Astrophysics, 426, 503

Yıldız, U. A., Kristensen, L. E., Van Dishoeck, E. F., et al. 2012, Astronomy & Astrophysics, 542, A86

Yıldız, U. A., Kristensen, L. E., van Dishoeck, E. F., et al. 2015, Astronomy & Astrophysics, 576, A109

Yıldız, U. A., Kristensen, L. E., van Dishoeck, E. F., et al. 2013, Astronomy & Astrophysics, 556, A89

A   Spectra for determining integration velocity ranges.

A.1   N12
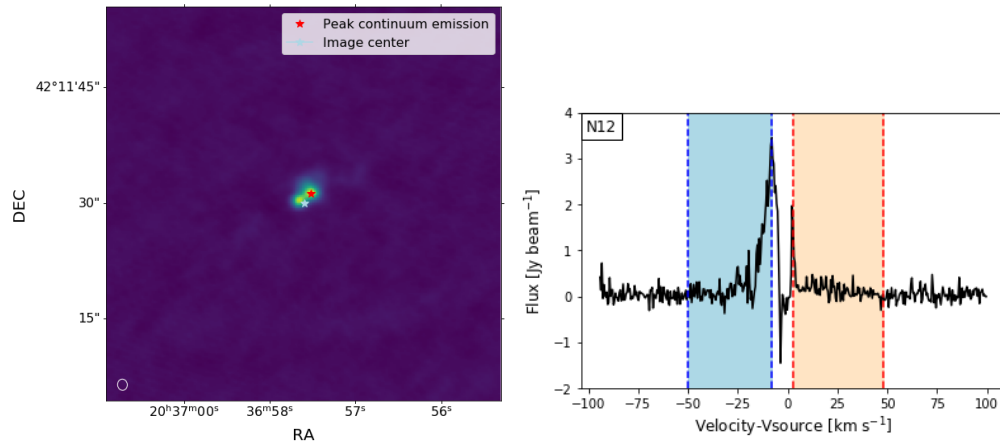
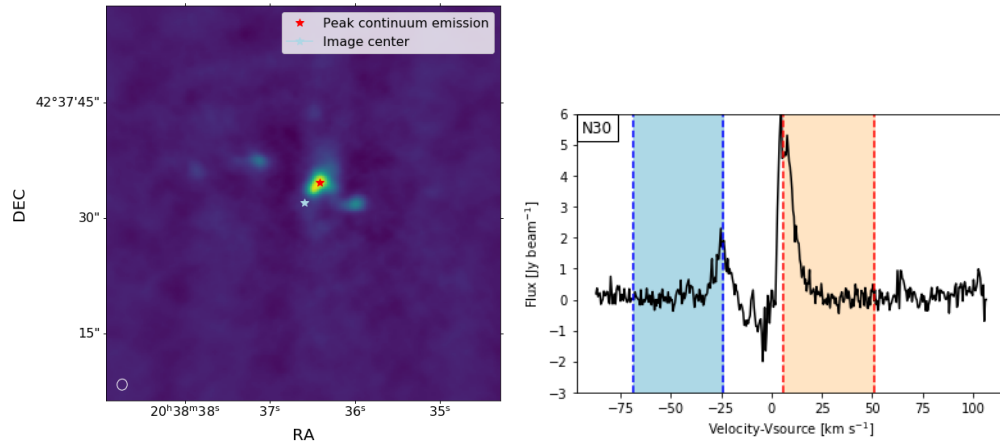**Figure 24:** [Left]: Continuum emission of N12, with the location of the peak marked with a red star and the center of the image with a light blue star.[Right]: Spectrum of N12 from the location of peak continuum emission.
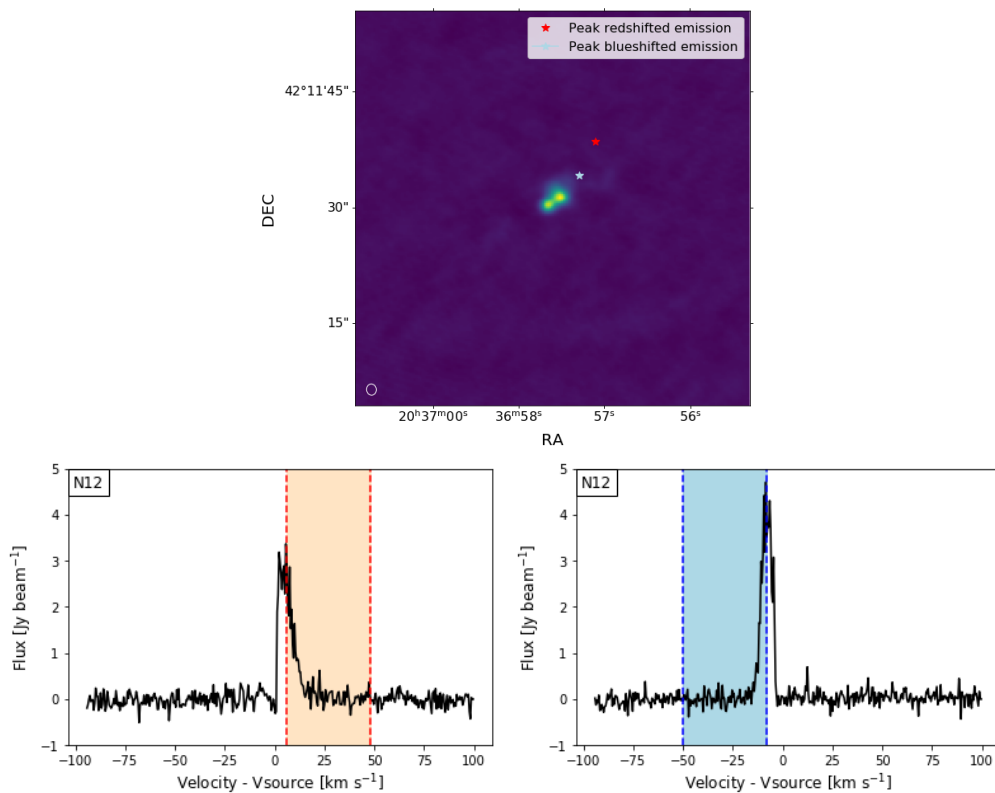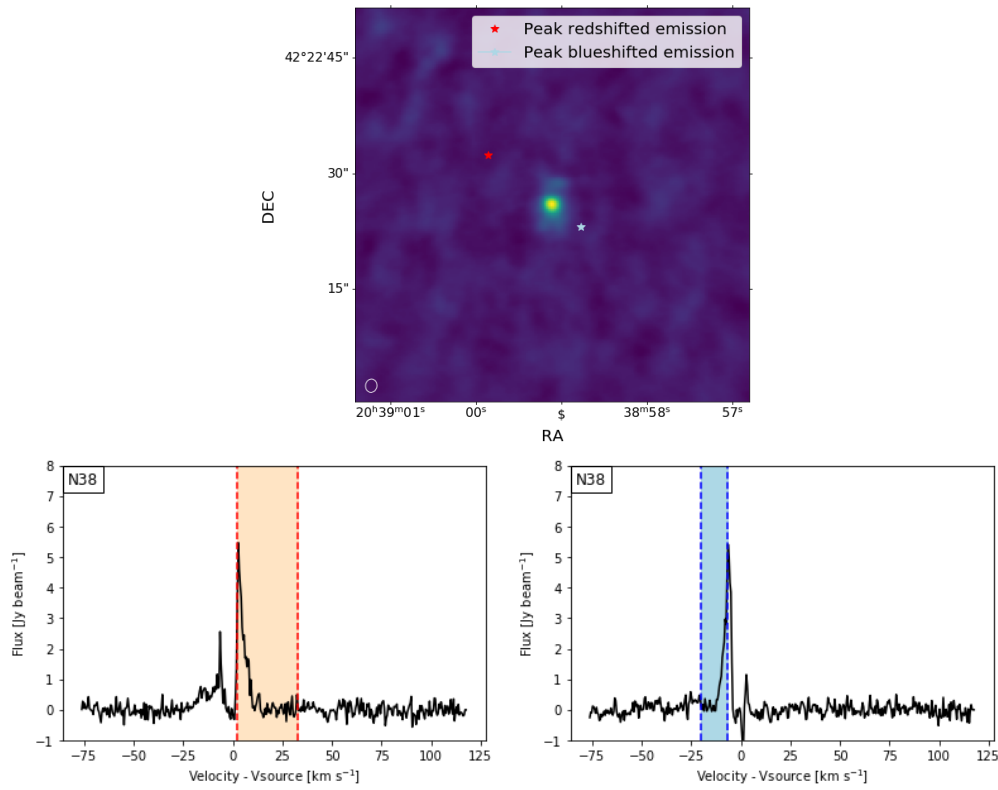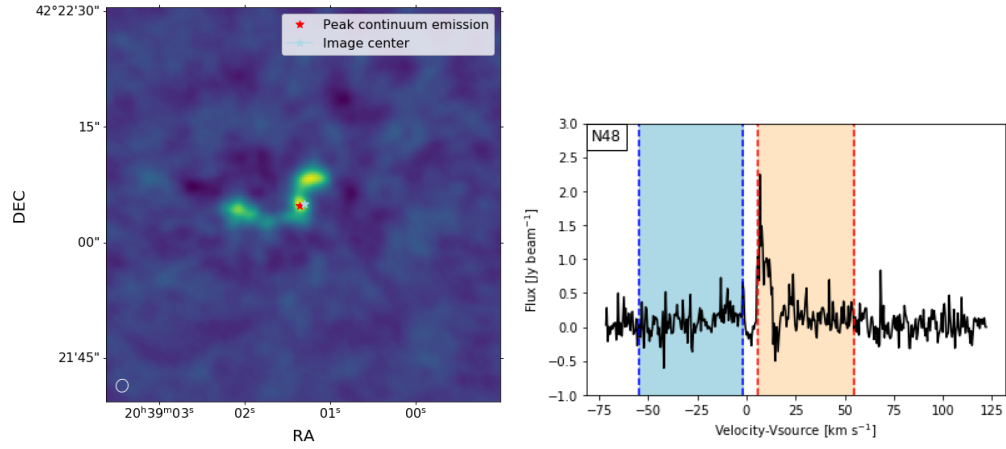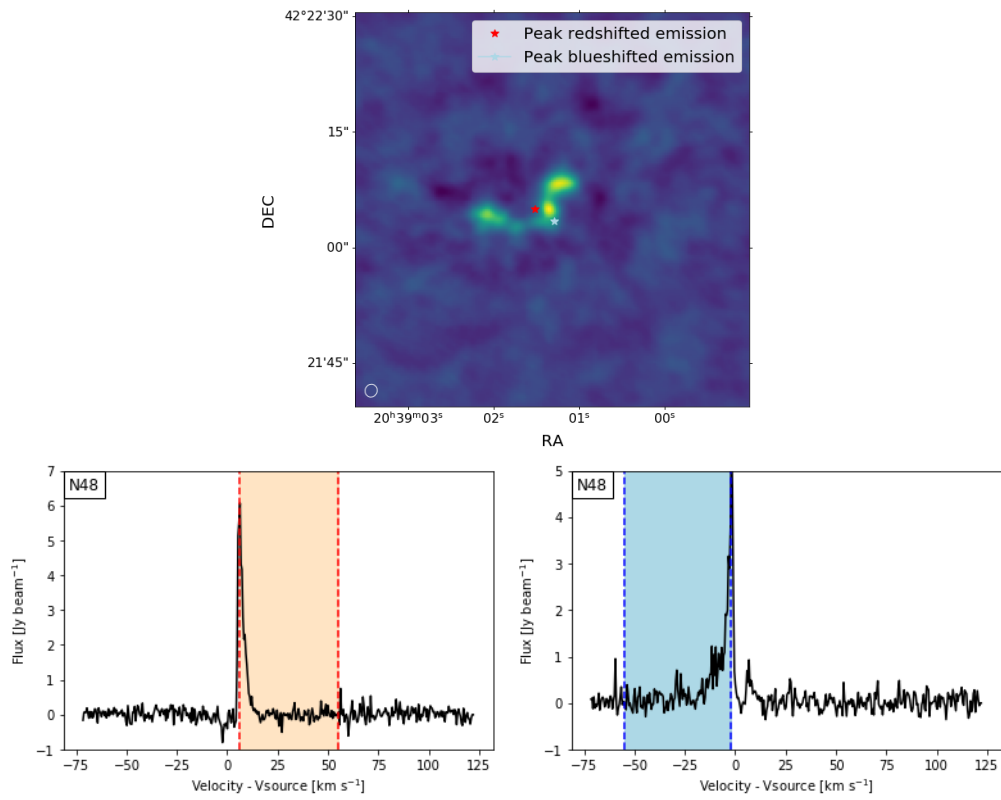

Figure 25: [Top]: Continuum emission of N12, with the location of the peak marked with a red star and the center of the image with a light blue star. [Left]: Spectrum of N12 from the location of peak red-shifted emission. [Right]: Spectrum of N12 from the location of peak blue-shifted emission.
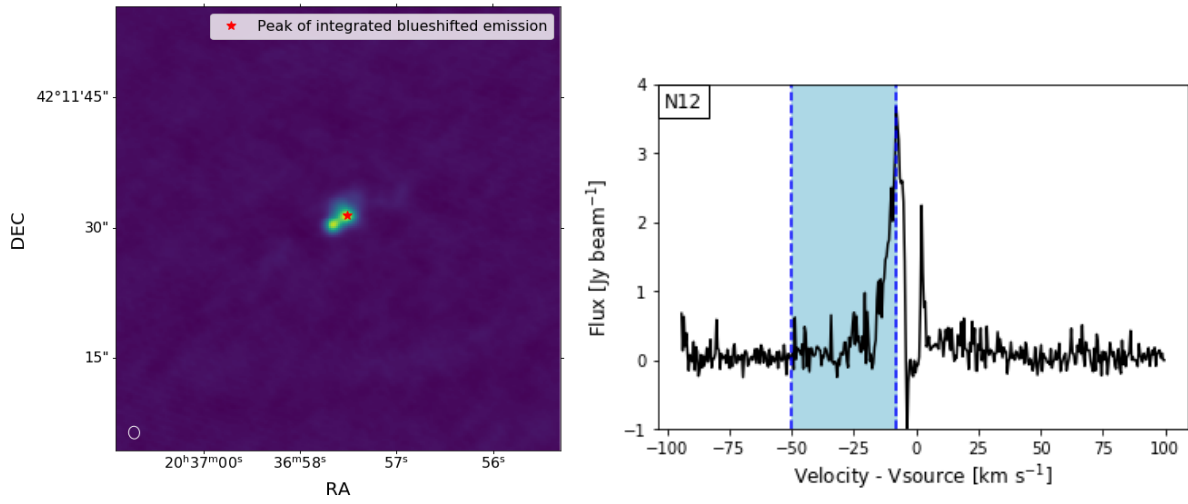
Figure 26: [Left]: Continuum emission of N12, with the location of the peak of the integrated blue-shifted CO emission marked with a red star.[Right]: Spectrum of N12 from the location of the peak of the integrated blue-shifted emission.
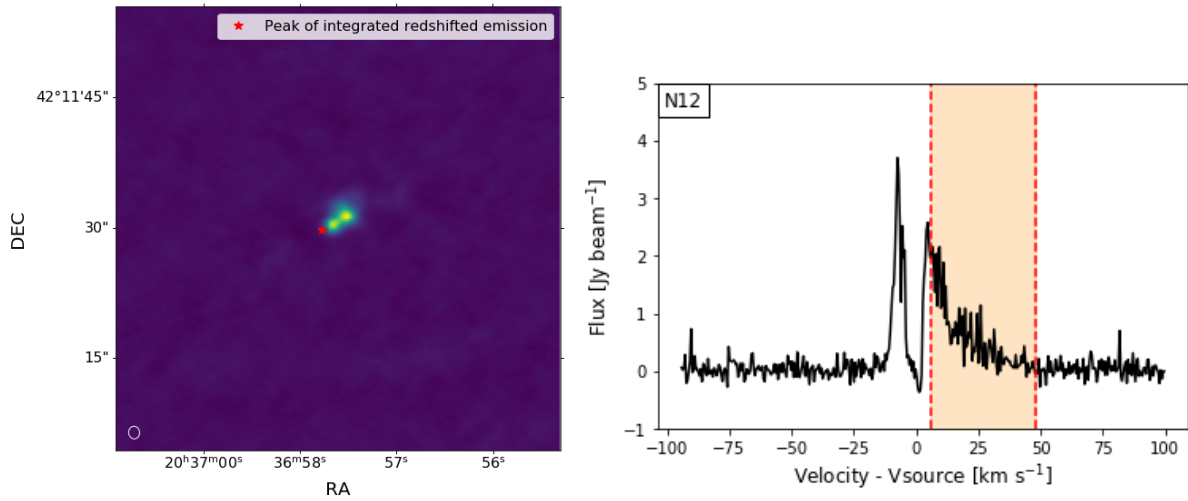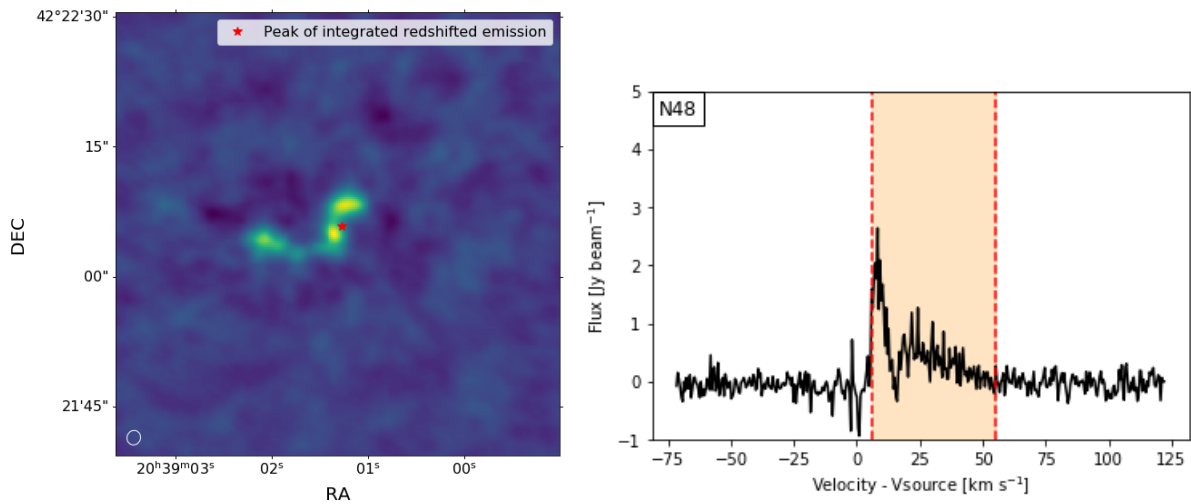

Figure 27: [Left]: Continuum emission of N12, with the location of the peak of the integrated red-shifted CO emission marked with a red star.[Right]: Spectrum of N12 from the location of the peak of the integrated red-shifted emission.
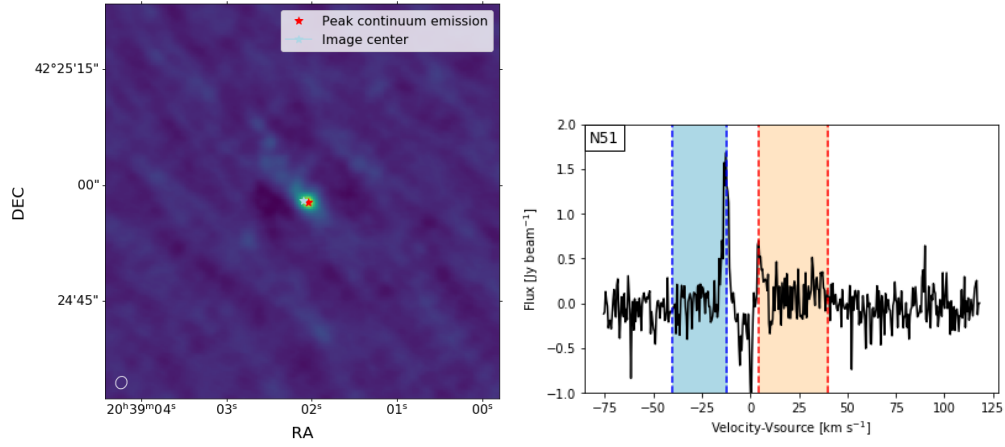
A.2 N30
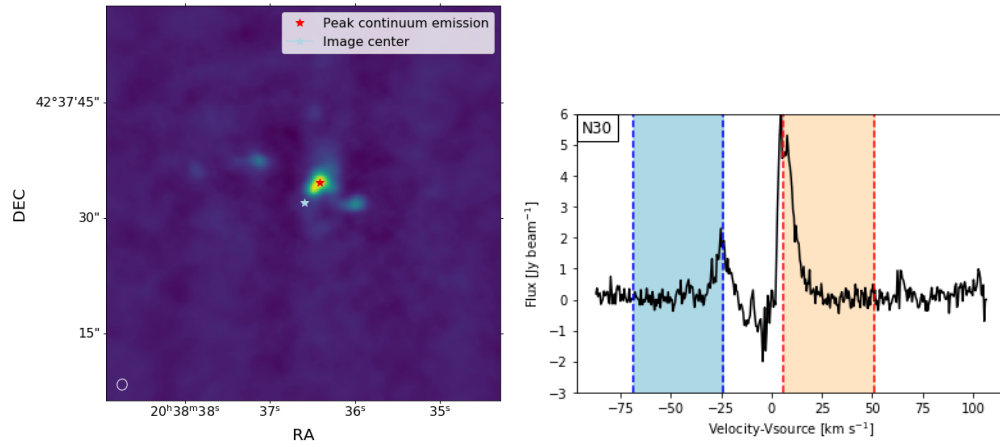
Figure 28: [Left]: Continuum emission of N30, with the location of the peak marked with a red star and the center of the image with a light blue star.[Right]: Spectrum of N30 from the location of peak continuum emission.
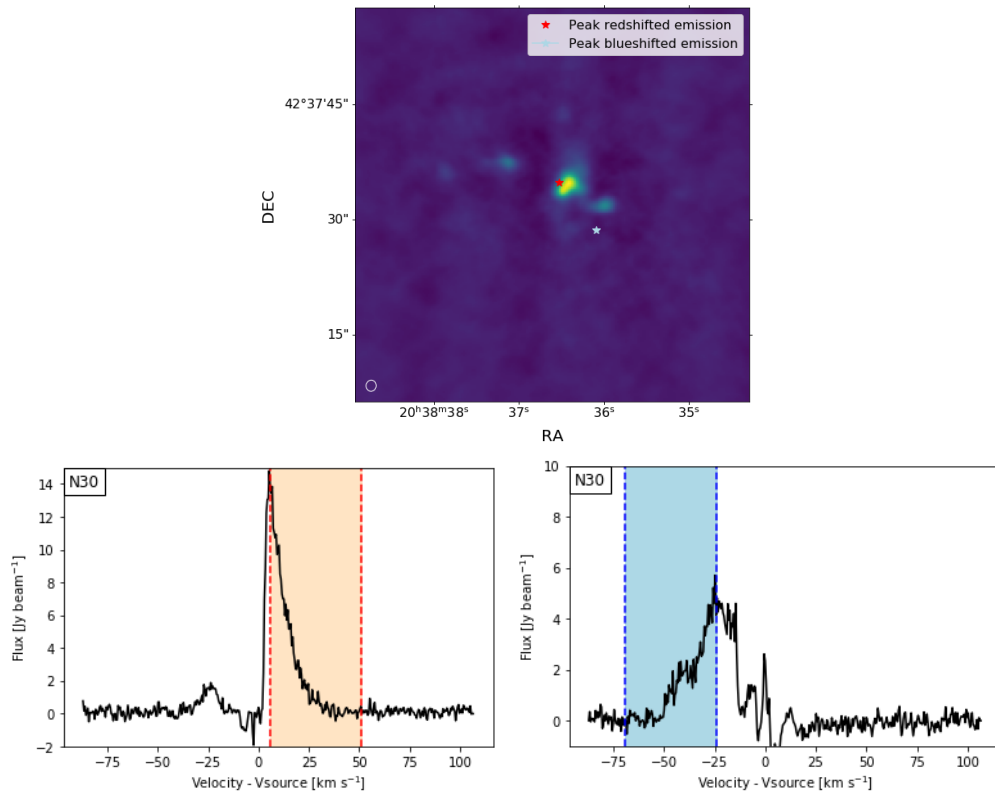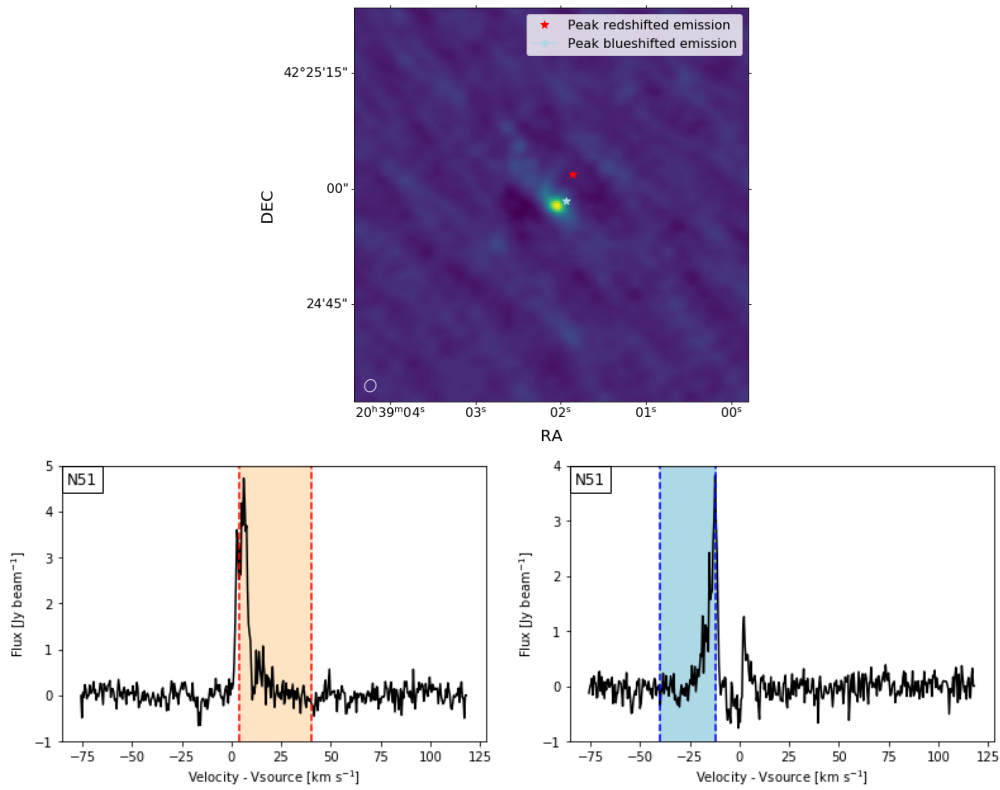

Figure 29: [Top]: Continuum emission of N30, with the location of the peak marked with a red star and the center of the image with a light blue star. [Left]: Spectrum of N30 from the location of peak red-shifted emission. [Right]: Spectrum of N30 from the location of peak blue-shifted emission.
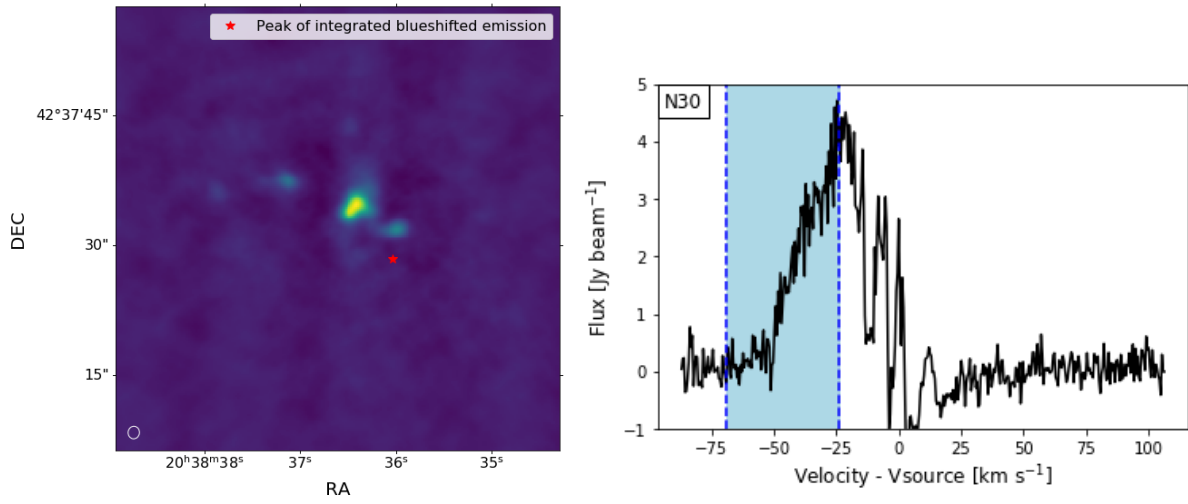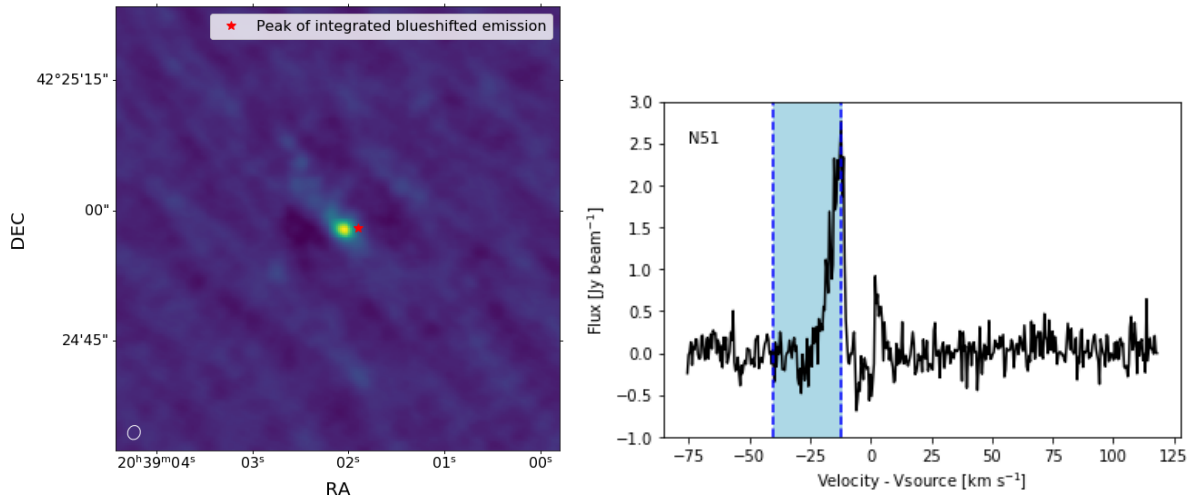
Figure 30: [Left]: Continuum emission of N30, with the location of the peak of the integrated blue-shifted CO emission marked with a red star.[Right]: Spectrum of N30 from the location of the peak of the integrated blue-shifted emission.
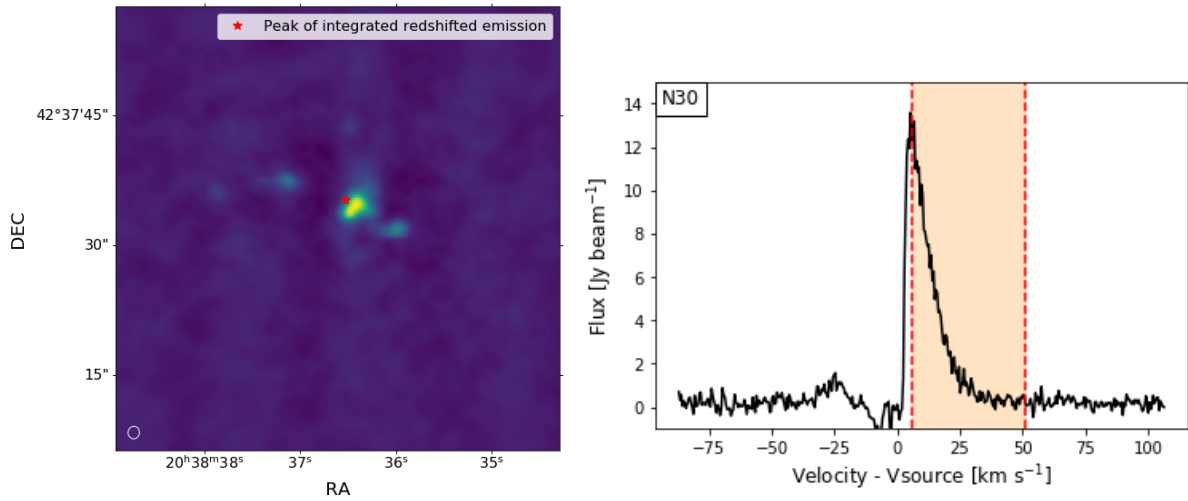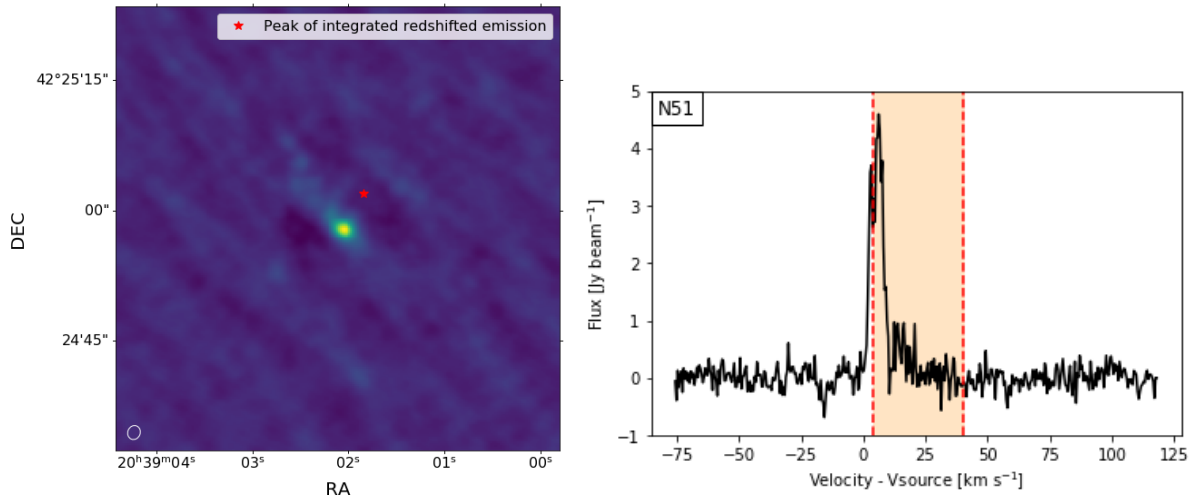

Figure 31: [Left]: Continuum emission of N30, with the location of the peak of the integrated red-shifted CO emission marked with a red star.[Right]: Spectrum of N30 from the location of the peak of the integrated red-shifted emission.
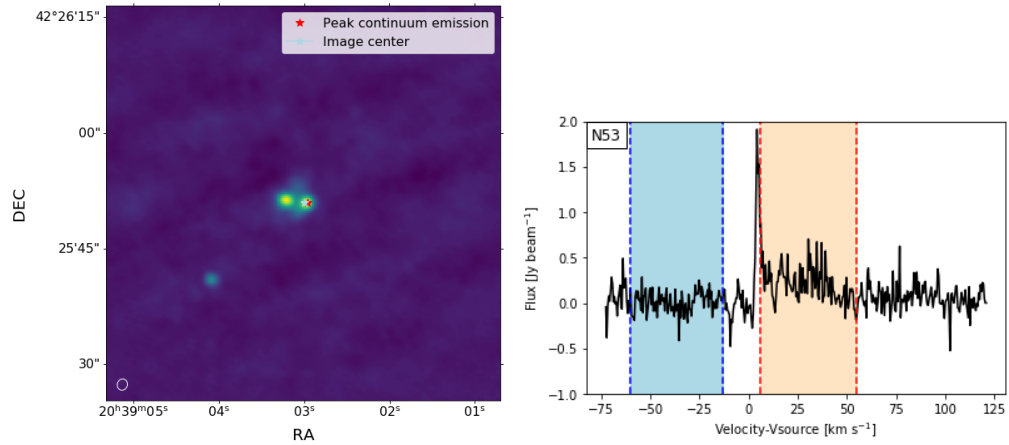
A.3 N38

Figure 32: [Left]: Continuum emission of N30, with the location of the peak marked with a red star and the center of the image with a light blue star.[Right]: Spectrum of N30 from the location of peak continuum emission.

Figure 33: [Top]: Continuum emission of N38, with the location of the peak marked with a red star and the center of the image with a light blue star. [Left]: Spectrum of N38 from the location of peak red-shifted emission. [Right]: Spectrum of N38 from the location of peak blue-shifted emission.
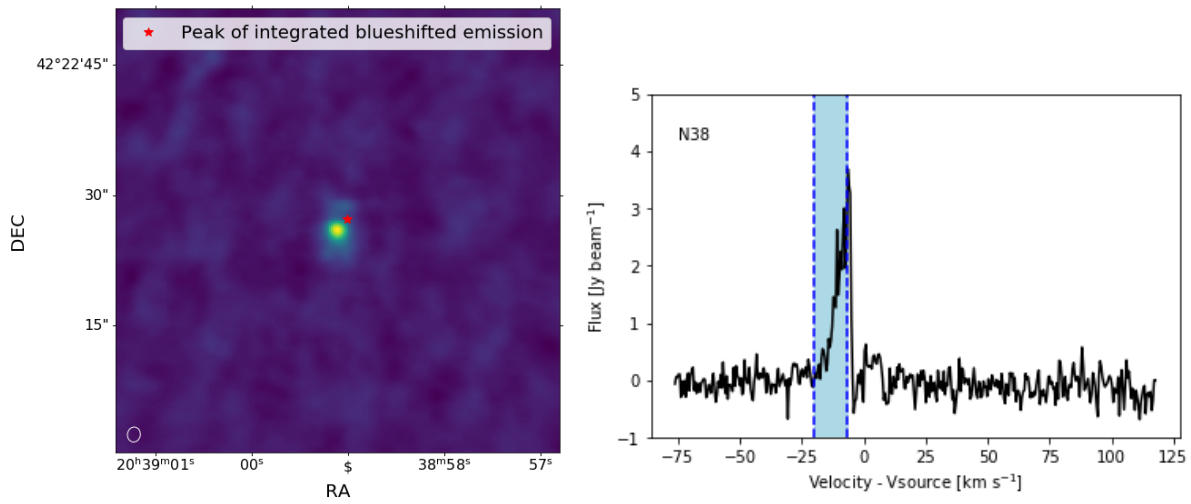
Figure 34: [Left]: Continuum emission of N38, with the location of the peak of the integrated blue-shifted CO emission marked with a red star.[Right]: Spectrum of N38 from the location of the peak of the integrated blue-shifted emission.
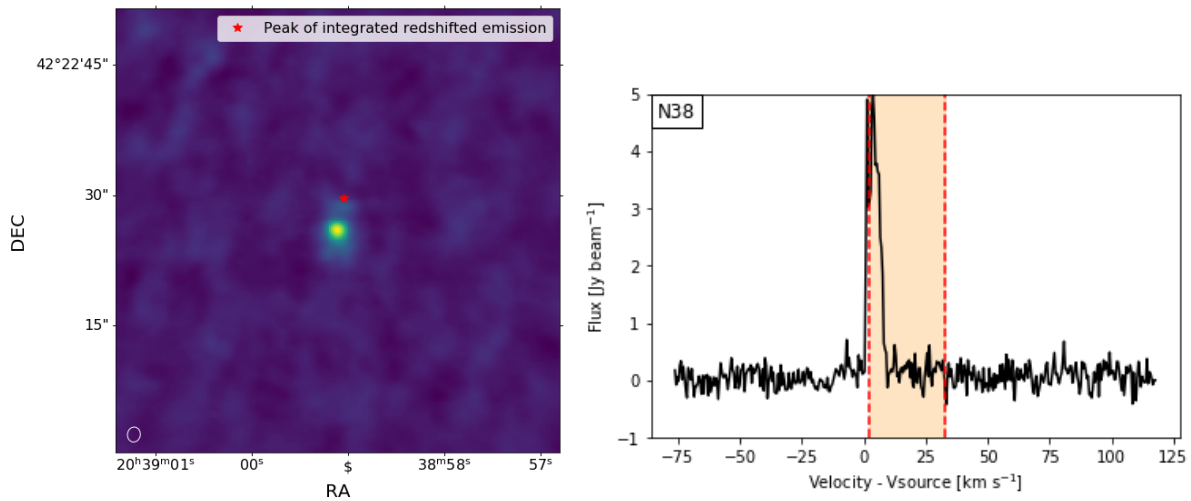
Figure 35: [Left]: Continuum emission of N38, with the location of the peak of the integrated red-shifted CO emission marked with a red star.[Right]: Spectrum of N38 from the location of the peak of the integrated red-shifted emission.

A.4   N48

Figure 36: [Left]: Continuum emission of N48, with the location of the peak marked with a red star and the center of the image with a light blue star.[Right]: Spectrum of N48 from the location of peak continuum emission.
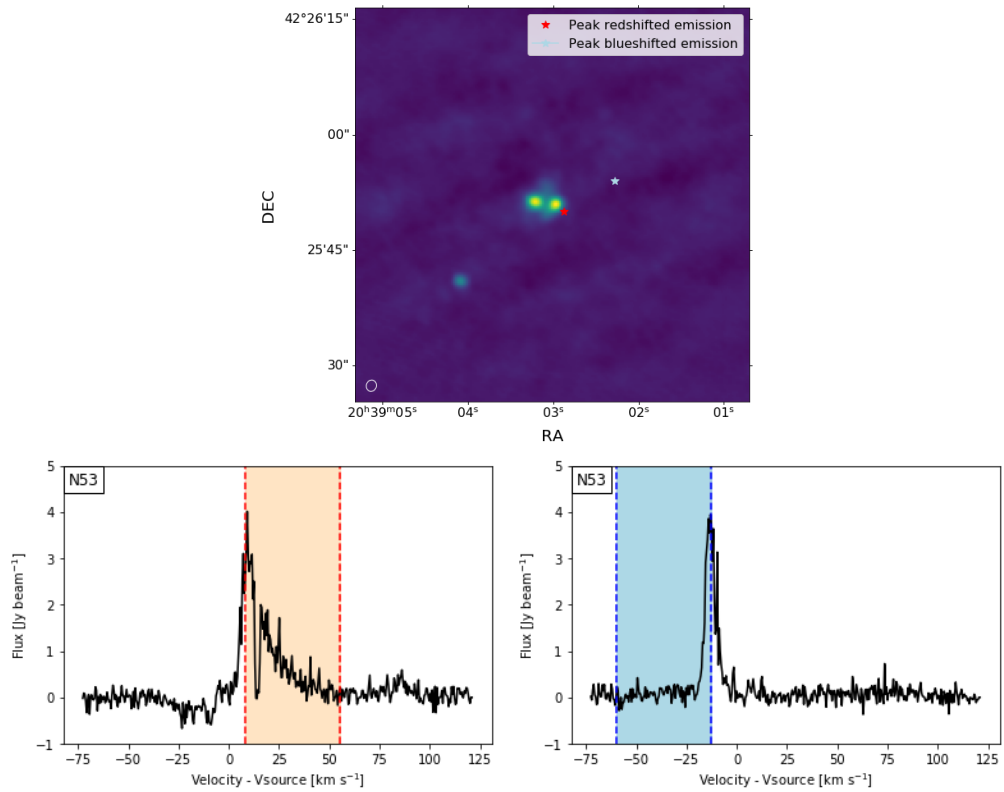

Figure 37: [Top]: Continuum emission of N48, with the location of the peak marked with a red star and the center of the image with a light blue star. [Left]: Spectrum of N48 from the location of peak red-shifted emission. [Right]: Spectrum of N48 from the location of peak blue-shifted emission.
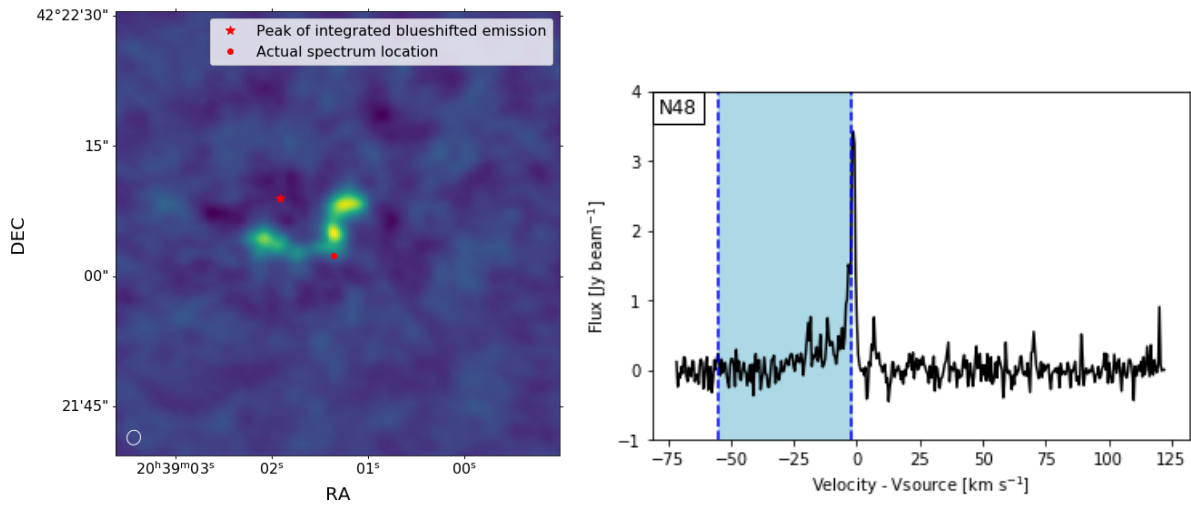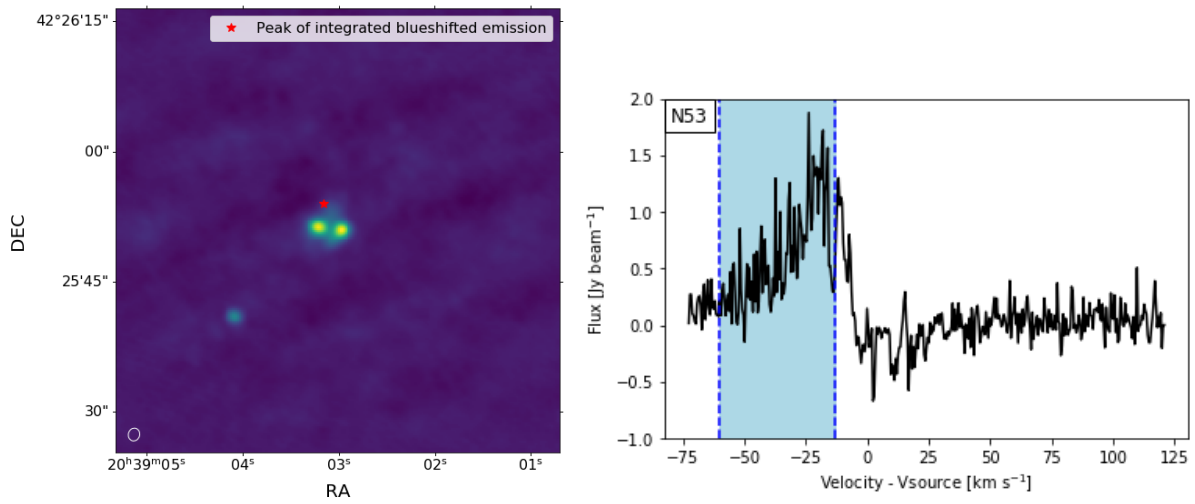
Figure 38: [Left]: Continuum emission of N48, with the location of the peak of the integrated blue-shifted CO emission marked with a red star.[Right]: Spectrum of N48 from the location of the peak of the integrated blue-shifted emission.
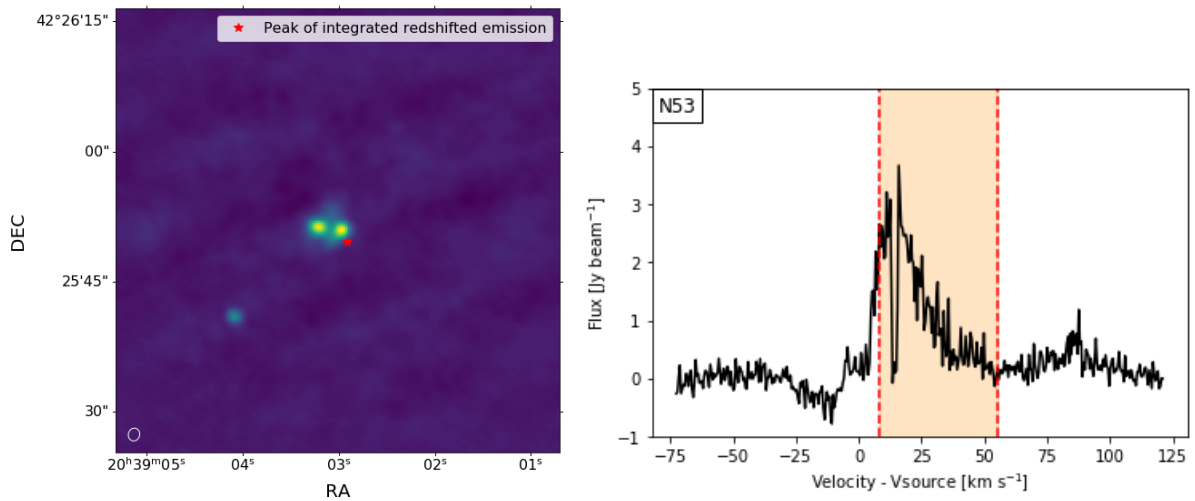

Figure 39: [Left]: Continuum emission of N48, with the location of the peak of the integrated red-shifted CO emission marked with a red star.[Right]: Spectrum of N48 from the location of the peak of the integrated red-shifted emission.
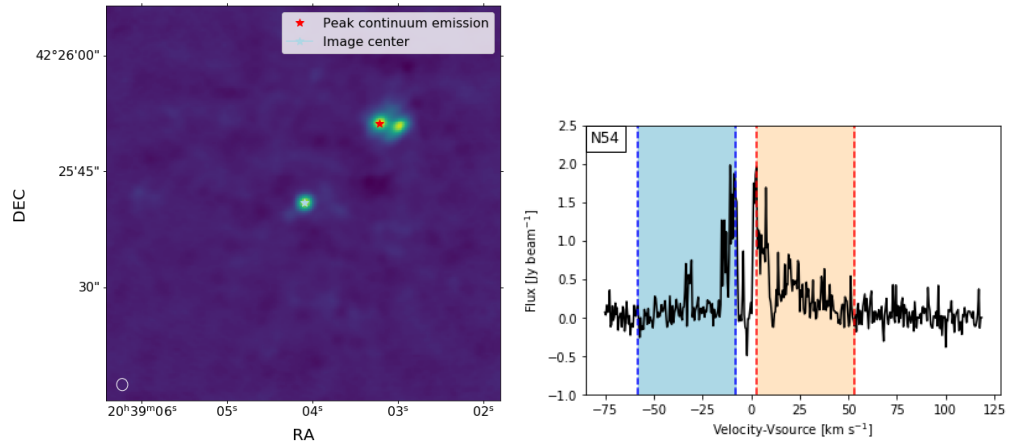
A.5 N51

Figure 40: [Left]: Continuum emission of N51, with the location of the peak marked with a red star and the center of the image with a light blue star.[Right]: Spectrum of N51 from the location of peak continuum emission.
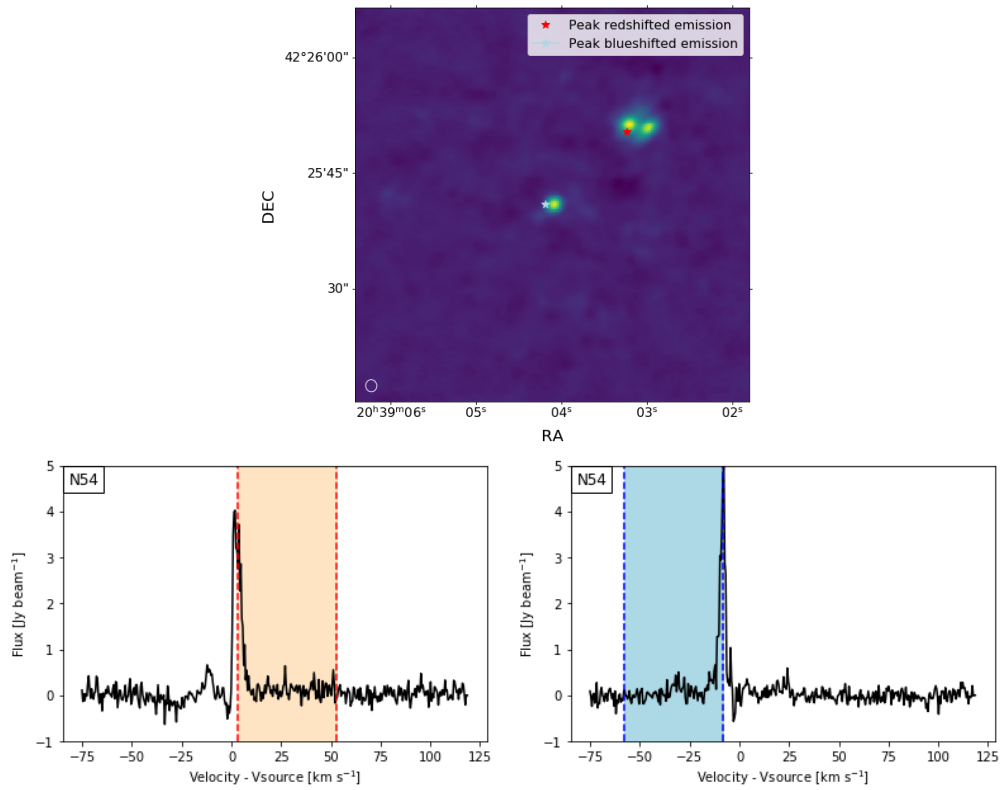

Figure 41: [Top]: Continuum emission of N51, with the location of the peak marked with a red star and the center of the image with a light blue star. [Left]: Spectrum of N51 from the location of peak red-shifted emission. [Right]: Spectrum of N51 from the location of peak blue-shifted emission.
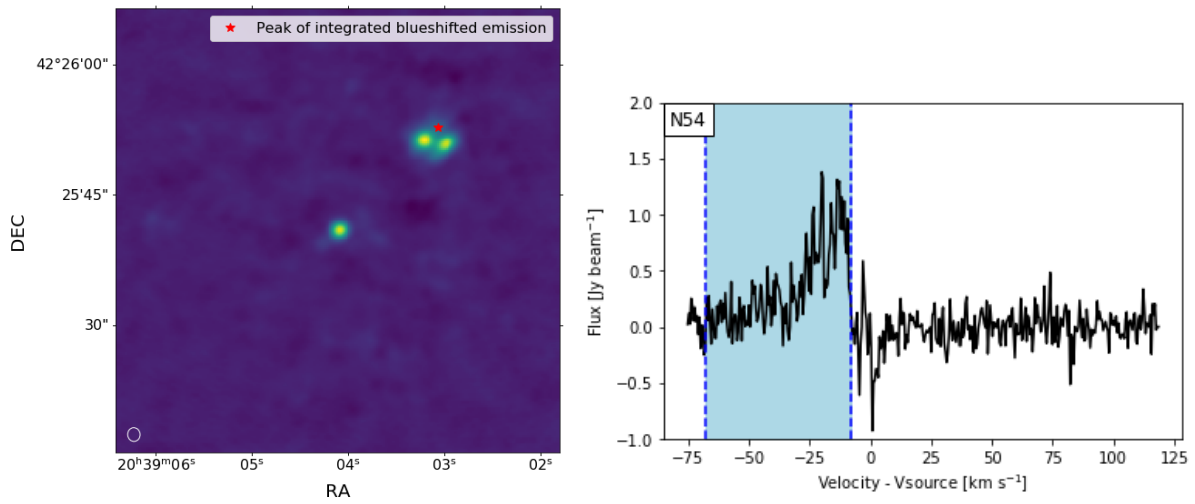
Figure 42: [Left]: Continuum emission of N51, with the location of the peak of the integrated blue-shifted CO emission marked with a red star.[Right]: Spectrum of N51 from the location of the peak of the integrated blue-shifted emission.
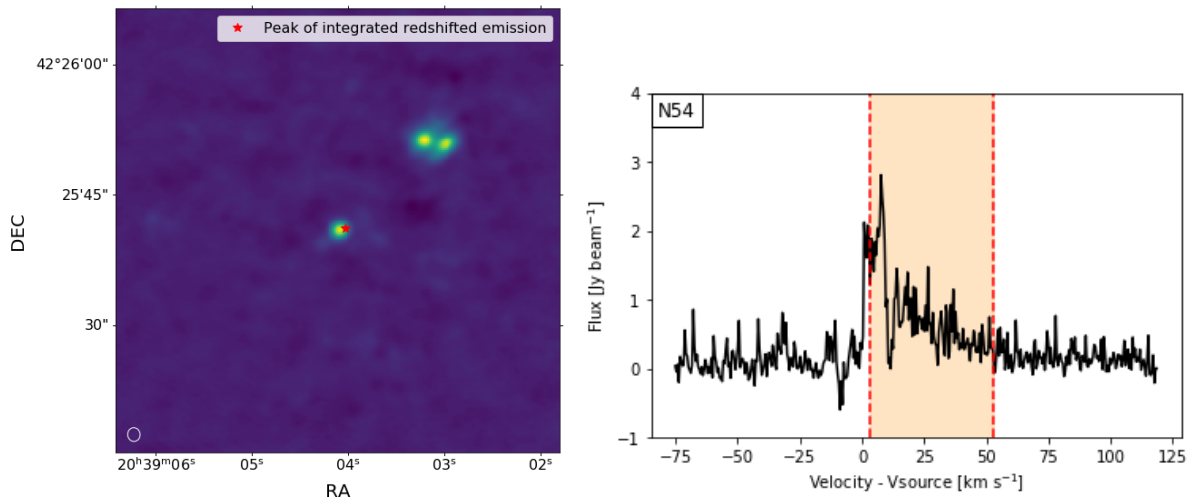

Figure 43: [Left]: Continuum emission of N51, with the location of the peak of the integrated red-shifted CO emission marked with a red star.[Right]: Spectrum of N51 from the location of the peak of the integrated red-shifted emission.
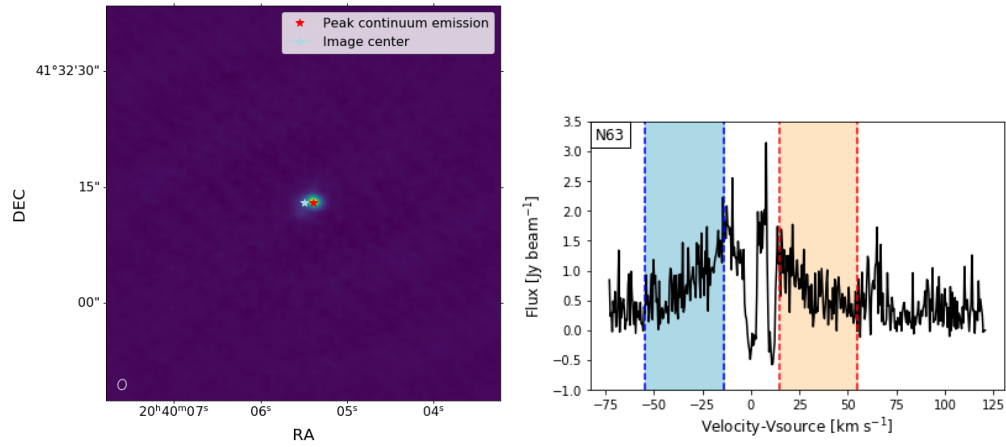
A.6 N53

Figure 44: [Left]: Continuum emission of N53, with the location of the peak marked with a red star and the center of the image with a light blue star.[Right]: Spectrum of N53 from the location of peak continuum emission.

Figure 45: [Top]: Continuum emission of N53, with the location of the peak marked with a red star and the center of the image with a light blue star. [Left]: Spectrum of N53 from the location of peak red-shifted emission. [Right]: Spectrum of N53 from the location of peak blue-shifted emission.

Figure 46: [Left]: Continuum emission of N53, with the location of the peak of the integrated blue-shifted CO emission marked with a red star.[Right]: Spectrum of N53 from the location of the peak of the integrated blue-shifted emission.

Figure 47: [Left]: Continuum emission of N53, with the location of the peak of the integrated red-shifted CO emission marked with a red star.[Right]: Spectrum of N53 from the location of the peak of the integrated red-shifted emission.

A.7   N54

Figure 48: [Left]: Continuum emission of N54, with the location of the peak marked with a red star and the center of the image with a light blue star.[Right]: Spectrum of N54 from the location of peak continuum emission.
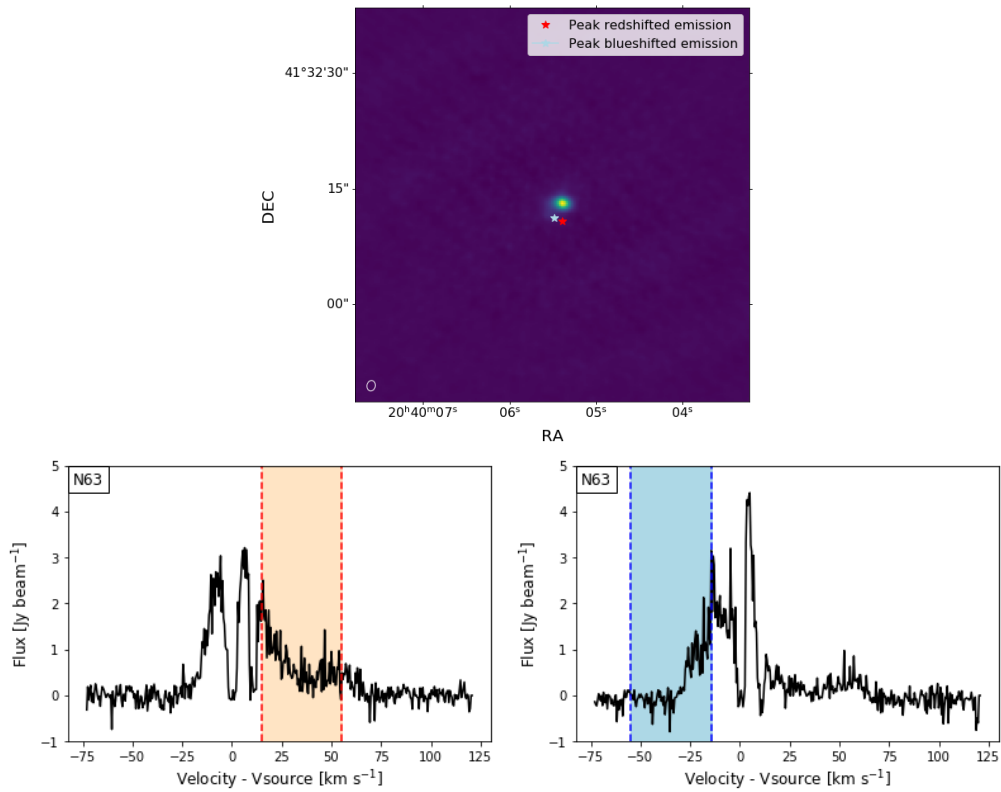

Figure 49: [Top]: Continuum emission of N54, with the location of the peak marked with a red star and the center of the image with a light blue star. [Left]: Spectrum of N54 from the location of peak red-shifted emission. [Right]: Spectrum of N54 from the location of peak blue-shifted emission.
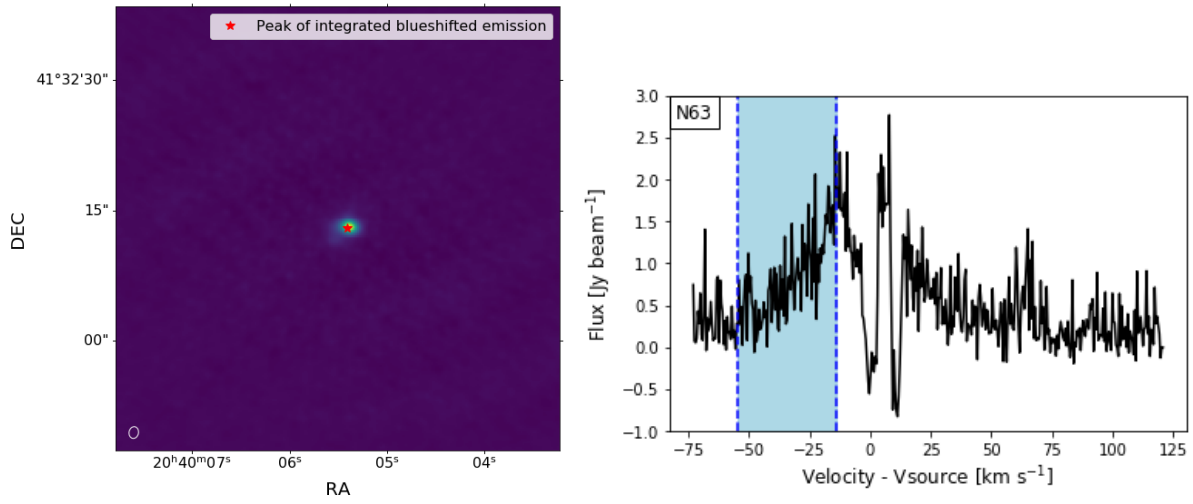
Figure 50: [Left]: Continuum emission of N54, with the location of the peak of the integrated blue-shifted CO emission marked with a red star.[Right]: Spectrum of N54 from the location of the peak of the integrated blue-shifted emission.
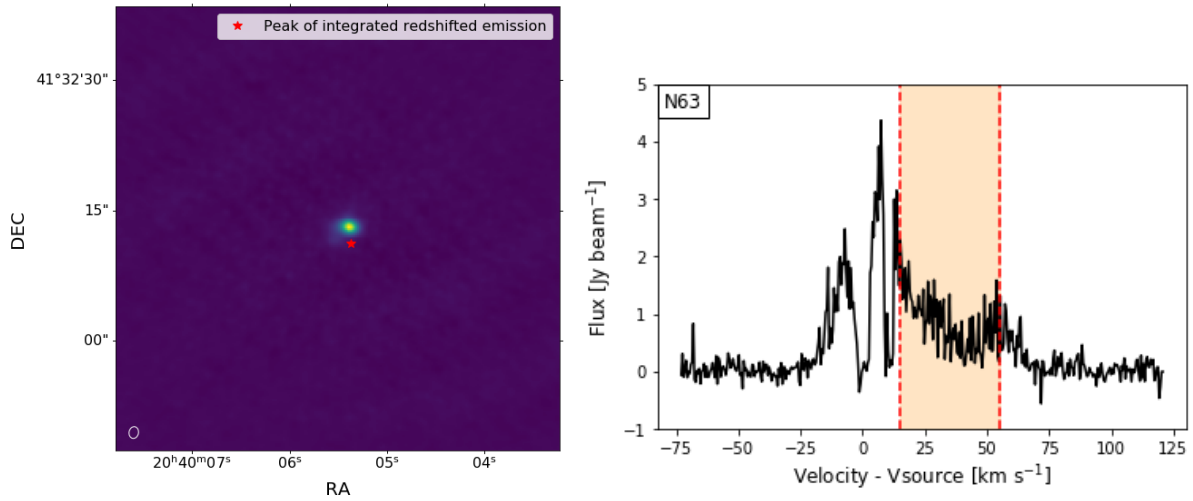

Figure 51: [Left]: Continuum emission of N54, with the location of the peak of the integrated red-shifted CO emission marked with a red star.[Right]: Spectrum of N54 from the location of the peak of the integrated red-shifted emission.
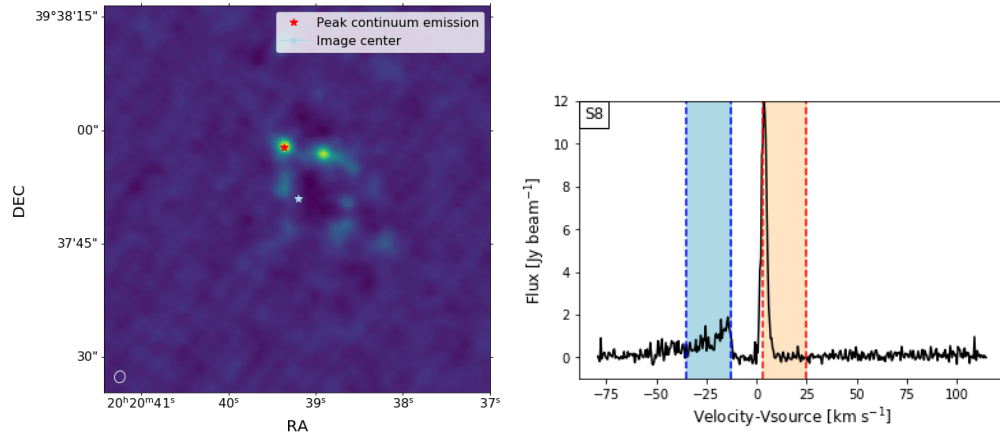
A.8 N63

Figure 52: [Left]: Continuum emission of N63, with the location of the peak marked with a red star and the center of the image with a light blue star.[Right]: Spectrum of N63 from the location of peak continuum emission.
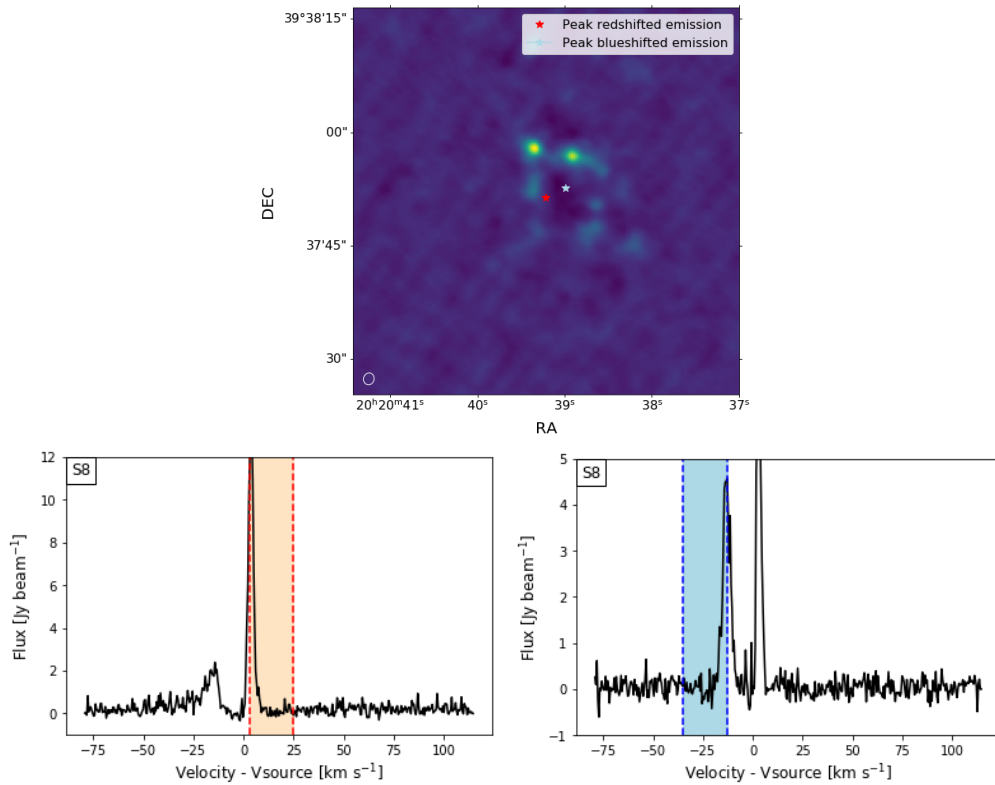

Figure 53: [Top]: Continuum emission of N63, with the location of the peak marked with a red star and the center of the image with a light blue star. [Left]: Spectrum of N63 from the location of peak red-shifted emission. [Right]: Spectrum of N63 from the location of peak blue-shifted emission.
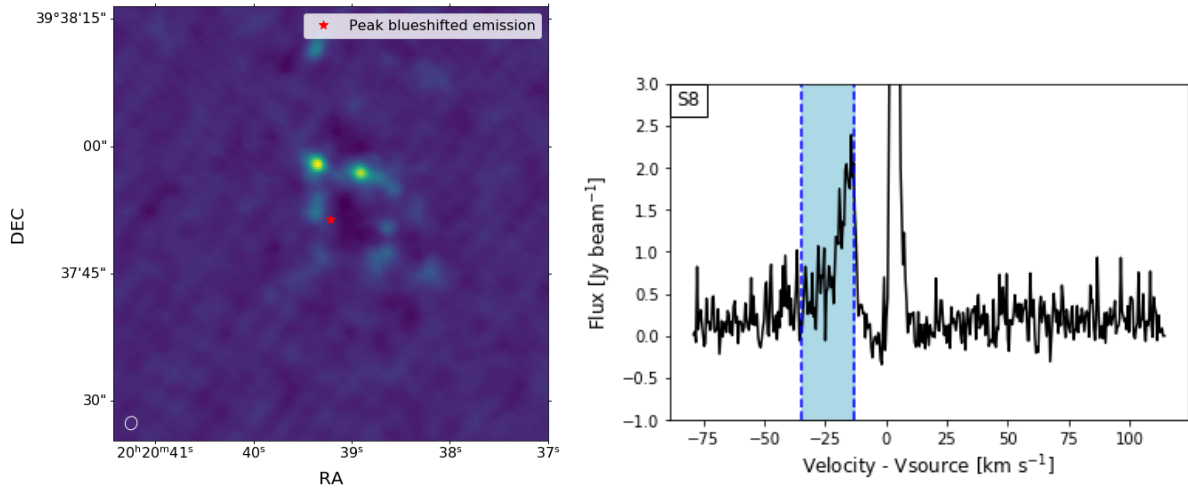
Figure 54: [Left]: Continuum emission of N63, with the location of the peak of the integrated blue-shifted CO emission marked with a red star.[Right]: Spectrum of N63 from the location of the peak of the integrated blue-shifted emission.
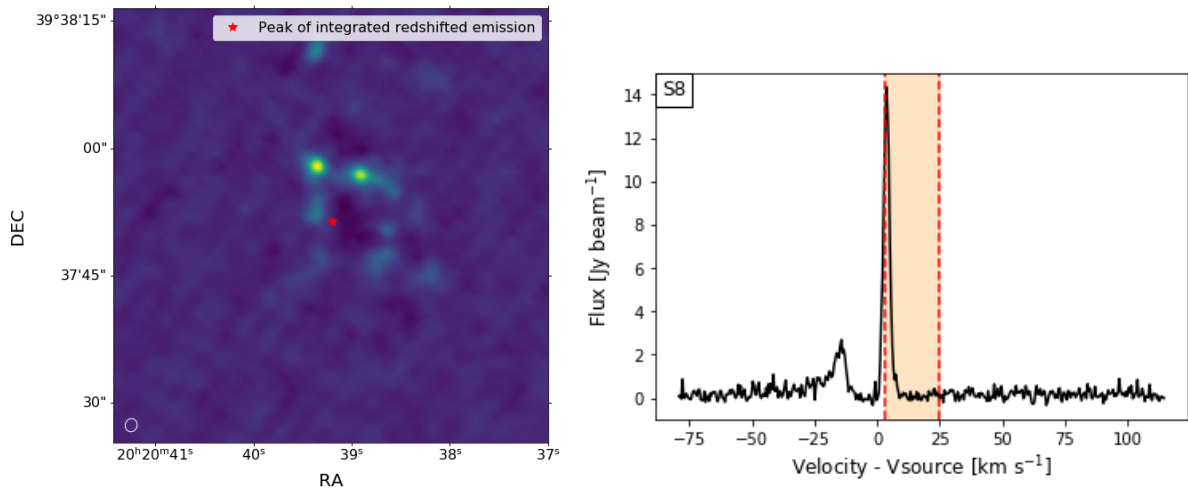

Figure 55: [Left]: Continuum emission of N63, with the location of the peak of the integrated red-shifted CO emission marked with a red star.[Right]: Spectrum of N63 from the location of the peak of the integrated red-shifted emission.

A.9 S8

Figure 56: [Left]: Continuum emission of S8, with the location of the peak marked with a red star and the center of the image with a light blue star.[Right]: Spectrum of S8 from the location of peak continuum emission.
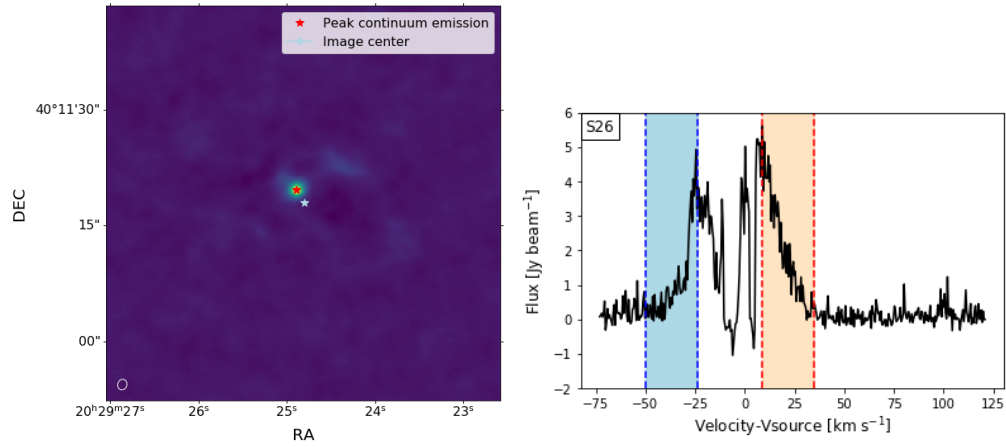

Figure 57: [Top]: Continuum emission of S8, with the location of the peak marked with a red star and the center of the image with a light blue star. [Left]: Spectrum of S8 from the location of peak red-shifted emission. [Right]: Spectrum of S8 from the location of peak blue-shifted emission.

Figure 58: [Left]: Continuum emission of S8, with the location of the peak of the integrated blue-shifted CO emission marked with a red star.[Right]: Spectrum of S8 from the location of the peak of the integrated blue-shifted emission.

Figure 59: [Left]: Continuum emission of S8, with the location of the peak of the integrated red-shifted CO emission marked with a red star.[Right]: Spectrum of S8 from the location of the peak of the integrated red-shifted emission.

A.10 S26

Figure 60: [Left]: Continuum emission of S26, with the location of the peak marked with a red star and the center of the image with a light blue star.[Right]: Spectrum of S26 from the location of peak continuum emission.
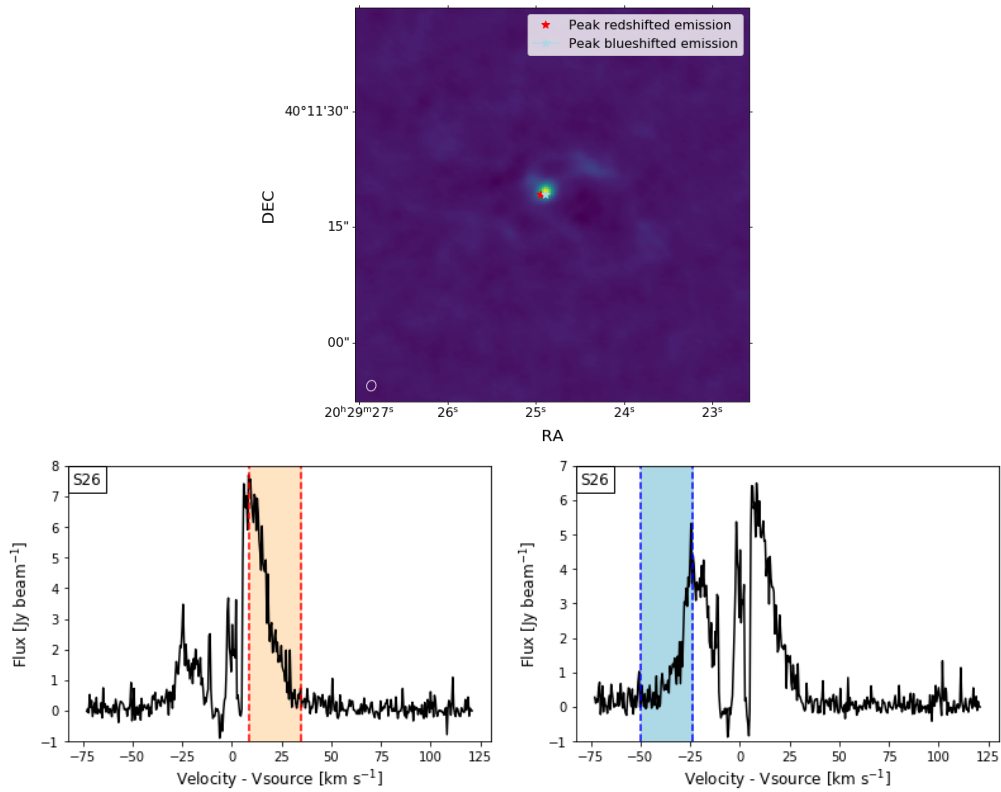

Figure 61: [Top]: Continuum emission of S26, with the location of the peak marked with a red star and the center of the image with a light blue star. [Left]: Spectrum of S26 from the location of peak red-shifted emission. [Right]: Spectrum of S26 from the location of peak blue-shifted emission.
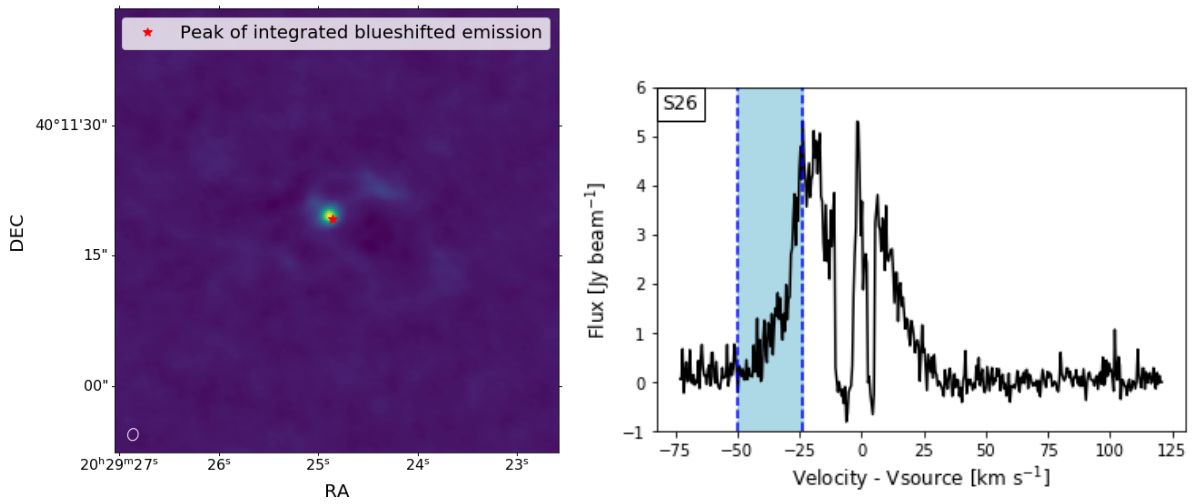
Figure 62: [Left]: Continuum emission of S26, with the location of the peak of the integrated blue-shifted CO emission marked with a red star.[Right]: Spectrum of S26 from the location of the peak of the integrated blue-shifted emission.
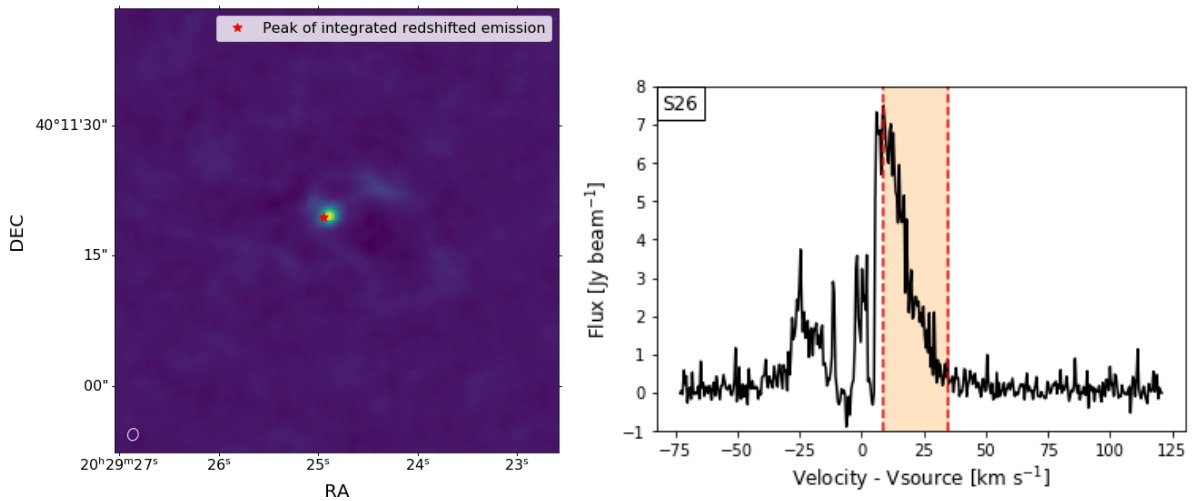

Figure 63: [Left]: Continuum emission of S26, with the location of the peak of the integrated red-shifted CO emission marked with a red star.[Right]: Spectrum of S26 from the location of the peak of the integrated red-shifted emission.